

Normal-Mode and Ray Theory Applied to Underwater Acoustic Conditions of Extreme Downward Refraction

MELVIN A. PEDERSEN AND DAVID F. GORDON

Naval Undersea Research and Development Center, San Diego, California 92132

This theoretical article investigates the acoustic field in the image-interference and shadow-zone regions for a model in which the sound velocity decreases with increasing depth from the surface. Near the surface the shadow-zone boundary is the surface-grazing ray, while in deeper regions this boundary is a caustic. The field near the caustic is investigated by modified ray theory based on Airy functions. A comparison of mode theory results with those of ray theory indicates that there is a $-\pi/2$ jump in the ray theory phase when the ray touches a caustic. There is, however, no such jump when the ray becomes horizontal. The normal-mode series is absolutely convergent for ranges greater than 1.732 times the sum of the source and receiver depths. When the shadow zone is bounded by a well-developed caustic, the series converges so slowly as to be impractical except at ranges well into the shadow-zone region.

LIST OF SYMBOLS

A_i	Airy integral	$H_{h/s}$	propagation loss, source and receiver exchanged
A_n	contribution of mode n	$H_{s/h}$	propagation loss, normal source and receiver
A_s	asymptotic approximation to A_i	H_0^2	second Hankel function of order zero
a	velocity profile parameter	h_1, h_2	modified Hankel functions of order one-third
a_n	n th root of the Airy integral	h'_1, h'_2	derivatives of modified Hankel functions
b	velocity profile parameter	g	$=pv$ = intensity
C	sound velocity	I	$= p^2 /\rho C$
C_h	sound velocity at receiver	Im	imaginary part of complex number
C_i	sound velocity at layer interface i	I/F	relative intensity of ray theory
C_m	ray parameter	$(I/F)_c$	relative intensity at caustic
C_s	sound velocity at source	$(I/F)_{cu}$	relative intensity for single arrival at caustic
$(C_m)_c$	ray parameter of caustic ray	$(I/F)_{\Delta R}$	relative intensity near caustic
C_0	surface sound velocity	K	coefficient in E_n
ϵ_i	phase shift of ray i	K	constant in Eq. 27
E_n	exponential factor in $ A_n $	k	$2\pi f/C_0$
F	average time rate of energy flow per unit solid angle	L	coefficient of proportionality, Eq. 30
F_n	coefficient in E_n	n	mode number
f	frequency	p	pressure
G	characteristic equation	p_0	pressure at unit distance from source
g	$-2k^2\gamma/C_0$	R	vector resultant, Fig. 5
H_e	$= -10 \log p^2/p_0^2 $ = propagation loss in sound-pressure level commonly used in experiments	R_c	range to caustic
H_i	propagation loss associated with the first i modes	R_0	unit distance
H_n	propagation loss associated with mode n	Re	real part of complex number
H_r	propagation loss in sound intensity level	r	$=R$ = range
		r_{pq}	range at which modes p and q are equal
		r_0	range of surface-grazing ray

S	a depth given by Eq. 64	γ	velocity gradient at surface
T	travel time	ΔR	range from caustic
l	argument of Airy integral, Eq. 28	ΔR_b	range of accuracy from caustic
U_n	depth function of mode n	ΔT	travel time difference
v	particle velocity	$\Delta \Psi$	$= 2\pi f \Delta T =$ phase difference
W_i	contribution of first i modes	ξ	argument of h_2 , Eq. 4
W_n	defined by Eq. 99	ξ_0	ξ evaluated at Z_0
X_n	defined by Eq. 94	$\eta(Z)$	index of refraction, Eq. B7
Y_n	defined by Eq. 97	θ_h	ray angle at receiver
Z	depth or receiver depth	θ_i	ray angle from horizontal at interface i
Z_h	receiver depth	θ_s	ray angle at source
Z_0	$= Z_s =$ source depth	ρ	density (assumed constant)
α	phase change, Fig. 5	λ_n	complex wavenumber
α	constant used in Appendix D	ϕ	velocity potential
α_m	coefficients in E_n	ϕ_0	velocity potential at unit distance
β	phase change, Fig. 5	Ψ	phase change in pressure occurring between source and receiver
β_m	coefficients in E_n		

INTRODUCTION

This article presents a comparison of normal-mode and ray theory under conditions of extreme downward refraction. This study was prompted by an earlier article¹ which examined a double family of modes in a surface duct. The first family of modes was recognized as containing those modes which propagate to long ranges. However the nature of the second family of modes was somewhat obscure. In a follow-up investigation the second family was found to be the only family present in the simple case of a negative-gradient velocity profile bounded above by the ocean surface and unbounded below. Although the original purpose was to determine the nature of this second family of modes under the simplest possible configuration, this study provides insights into a number of fundamental acoustic problems.

The earliest known mode solution for the model of this article was made by Pekeris.² The mode solution for a similar model (rigid rather than free surface) is presented by Morse and Ingard.³ The chief interest of these studies was to examine diffraction into the shadow zone. However they apparently overlooked the fact that the shadow-zone boundary is a caustic rather than the surface-grazing ray when the receiver depth is sufficiently far removed from the surface. Moreover these early studies were quite limited since digital computers were not developed to the point where numerical evaluation of the acoustic field was possible. Brekhovskikh⁴ uses a modified ray theory to investigate diffraction into a shadow zone using the composite model of a homogeneous half-space and an inhomogeneous half-space of the same mathematical form treated in the present article. However, in this case the entire shadow-zone boundary is a caustic, rather than only a portion as in the surface bounded case.

The present article makes numerical evaluation of the acoustic field using normal-mode theory, ray

theory, and a modified ray theory which includes the diffraction effects associated with a caustic. The ray theory solution is evaluated in the region ensonified by rays. The modified ray solution is evaluated in the neighborhood of the caustic. The mode theory solution is evaluated in the shadow zone. For receivers near the surface the mode theory is also readily evaluated into the region ensonified by rays. However, as the receiver depth is increased this evaluation becomes increasingly difficult because of roundoff error in the numerical computations. In some cases there is an overlapping of regions where the various solutions can be evaluated. In certain regions the numerical computations are often in almost perfect agreement, verifying the validity of the various theoretical approaches.

A topic of considerable interest has been the problem of whether a $-\pi/2$ jump in the phase of ray theory occurs at a ray vertex (turning point) or at a caustic. Tolstoy⁵ has reviewed this problem citing earlier work. Additional work has been published.⁶⁻⁸ The present consensus is that there is no phase jump associated with a ray vertex but there is one associated with a caustic. This is the position taken much earlier by Freehafer⁹ who prophetically stated, "there is frequently confusion regarding a possible change in phase when a ray passes through a turning point." Freehafer goes on to note that the source of confusion arises because the loci of turning points coincides with the caustic in the case of plane waves.

Two general approaches to the problem of phase jumps have been made in the work just cited. One approach is to investigate integral transforms using the approximations which lead to ray theory. The second approach is to investigate the effect of phase jumps in the transient solution for various impulsive sources. Deformations in the pulse shape can be associated with phase jumps which have occurred along the ray path. The present article uses a different approach for investigating phase jumps. An exact steady-state solution for

a harmonic source is calculated by normal-mode theory. For the steady-state situation one cannot examine phase along a single ray path as can be done with transients. However one can examine phase by the interference pattern between two arrivals traveling to the receiver by different ray paths. Phase jumps introduced in either of the two ray paths produces a marked range shift in the interference pattern. A comparison of the ray theory interference pattern with the exact normal-mode solution indicates the proper choice of phase jumps. These comparisons indicate that there is no phase jump associated with the ray vertex. However there appears to be a $-\pi/2$ change in phase associated with the caustic.

Another point of general acoustic interest is a comparison between ray and mode theory results which points up the importance of including the index of refraction in the conversion of velocity potential to intensity.

Section I of this article discusses the profile model and presents the various theoretical solutions. Section II compares numerical results of the theories for various source and receiver depths. Section III develops a correspondence between the mode theory solution and the presence or absence of caustics in the ray theory solution. In addition, the convergence properties of the normal-mode series are discussed. Section IV suggests areas for further investigation. Section V is a summary. There are four appendices that provide some of the mathematical details of the theory.

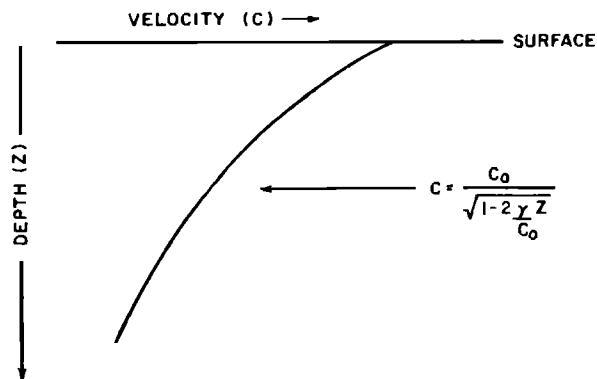
I. THEORETICAL SOLUTIONS

This section presents the model of the velocity depth profile and associated theories. The mode solution is presented first. This is followed by the ray solution, including ray diagrams. The final topic is the theoretical treatment of the field near a caustic, using a modified ray theory which accounts for diffraction.

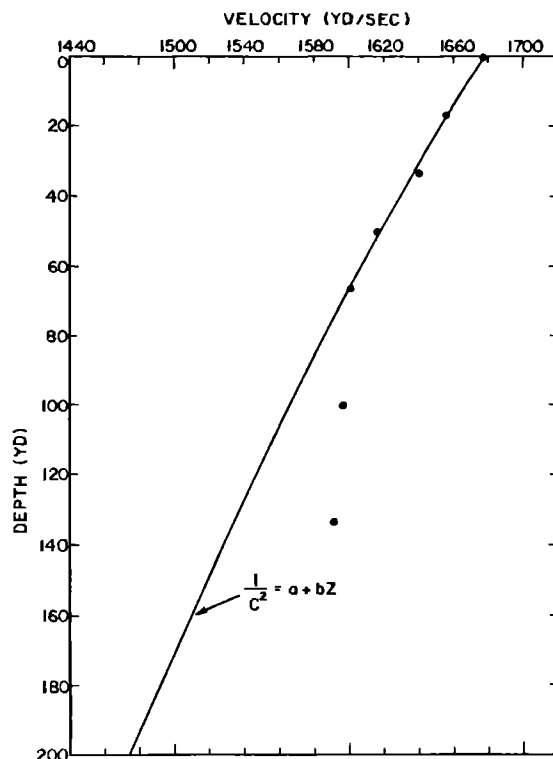
A. Velocity-Depth Profile Model

The ray and mode theories are both based on the profile model shown in Figs. 1(a) and 1(b). Figure 1(a) is a schematic model, depicting the parameters most convenient for the mode theory approach. The surface velocity is C_0 , while γ represents the slope (dC/dZ) evaluated at the surface.

Figure 1(b) presents a fit of the model to experimental velocity data, selected from the Pacific in an area of extreme velocity gradient. The reciprocal of the velocity squared was fit to a linear function of the depth by standard least-square methods. Only the five shallowest data points are included in the fit. The maximum departure of these five data points from the fit is 2.7 yd/sec. This is a fair fit considering that the velocity change from the surface to 67-yd depth is 75 yd/sec and that this simple model is of necessity stylized with



(a)



(b)

FIG. 1. (a) Schematic model depicting the profile parameters of the normal-mode approach. (b) Fit of the model to experimental velocity data. Two deepest data points are not included in the fit.

little flexibility. The two deepest data points are not included in the fit but are shown to indicate that the model is not physically realistic at depths greater than 67 yd. We are not really concerned in this paper with experimental data as our approach is to compare the results of two theoretical methods. However even in purely theoretical studies, it is desirable to make the models as realistic as possible. In order to test critical portions of the theory, we shall have to consider even greater depths than shown in Fig. 1(b). Although the theoretical velocities at these greater depths are not

only unrealistically low but also physically impossible, this lack of reality is irrelevant to the comparison of different theoretical approaches for an identical model.

The parameters, a and b in Fig. 1(b), are those most convenient for the ray theory approach. The parameter a is related to the velocity at $Z=0$, while b is a measure of the slope. The parameters of Fig. 1(a) are related to those of Fig. 1(b) as follows:

$$C_0 = a^{-1} \quad \text{and} \quad \gamma = -ba^{-1}/2 = -bC_0^3/2. \quad (1)$$

Numerical values for the fit of Fig. 1(b) are $a = 3.5543646 \times 10^{-7}$ (sec/yard)² and $b = 5.2072740 \times 10^{-10}$ sec²/yd³. Corresponding values for the parameters of Fig. 1(a) are $C_0 = 1677.3319$ yd/sec and $\gamma = -1.2286762$ sec⁻¹. All theoretical calculations in this paper are based on these parameters.

This paper only treats the case of γ negative, i.e., b positive. In this case the velocity decreases with increasing depth and approaches zero asymptotically at infinite depth. In the examination of the ray theory it will be convenient at times to ignore the presence of the ocean surface and to consider Z as assuming negative values. If the velocity curve is extended into the region of negative Z we find that C asymptotically approaches infinity as $Z \rightarrow -a/b$. In the example of Fig. 1(b) this horizontal asymptote is $Z = -682.6$ yd.

There are three additional basic parameters that are determined by the experimental setup. These include the frequency f and the source and receiver depths, designated by Z_0 and Z , respectively.

B. Normal-Mode Solution

This abbreviated presentation parallels that of Ref. 10, which should be consulted for additional detail and considerations. Certain useful combinations of the basic parameters are

$$k = 2\pi f/C_0 \quad \text{and} \quad g = -2k^2\gamma/C_0. \quad (2)$$

The product of the depth functions is

$$U_n(Z)U_n(Z_0) = -g^{1/2}[h_2'(Mx_n)]^{-2}h_2(\xi)h_2(\xi_0), \quad (3)$$

where

$$\xi = Mx_n + g^{1/2}Z. \quad (4)$$

The quantity ξ_0 is obtained by replacing Z by Z_0 in Eq. 4.

The h_2 function in Eq. 3 is a modified Hankel function of order one-third, while h_2' is the first derivative of this function. The quantity Mx_n in Eqs. 3 and 4 is a complex eigenvalue and is a root of the characteristic equation

$$h_2(Mx_n) = 0. \quad (5)$$

The propagation loss is given as a function of range r by

$$H_e = -10 \log \left| \sum_1^N H_0^2(\lambda_n r) U_n(Z) U_n(Z_0) \right|^2 - 20 \log \pi, \quad (6)$$

where H_0^2 is the second Hankel function of order zero. As discussed in Appendix C, Eq. 6 is equivalent to the relationship,

$$H_e = -10 \log |p^2/p_0^2|, \quad (6a)$$

where p is the pressure at the point (Z, r) and p_0 is the pressure at unit distance (1 yd) from the source located at the point $(Z_0, 0)$. The wavenumber λ_n is complex and is given by

$$\lambda_n = (k^2 - Mx_n g^{1/2})^{1/2}. \quad (7)$$

The expressions presented here may be obtained using the methods of Marsh¹¹ and Furry.¹² The derivation is outlined in Appendix A, which also indicates how the solution may be obtained as a degenerate case of the surface channel solution of Ref. 10. Appendix A also demonstrates that the modes correspond to the second family of modes for the two-layer case of Ref. 1. The solution as given by Eqs. 2-7 and the solution of Pekeris² can be shown to be equivalent.

The eigenvalue Mx_n is the n th zero of h_2 . Values for the first three zeros are given on p. xxxvi of Ref. 13. The first 50 values may be obtained from Ref. 14 and the relationship

$$Mx_n = -a_n \exp(2\pi i/3), \quad (8)$$

where a_n is the n th root of the Airy integral Ai . These roots are given to only nine or ten significant decimal digits. Because of certain roundoff errors to be discussed later, it was necessary to obtain the eigenvalues to more significant digits. This was done using Eq. 2 of Ref. 1 with $G = h_2(Mx_n)$ and $G' = h_2'(Mx_n)$. Initial values in Newton's iteration were obtained from Eq. 8, with a_n determined from Ref. 14 for $n \leq 50$ and from Eq. 11 for larger n .

All of the normal-mode calculations were done in double precision floating point on the CDC 1604 computer. The double precision word length is about 25 decimal digits. By comparing roots obtained by power series method to those obtained by asymptotic series it was found that the Mx_n were determined with accuracy of at least 19 decimal digits.

Note that the eigenvalues Mx_n are independent of the profile parameters and f . This means that once the set of Mx_n is determined with sufficient accuracy it applies to every mode calculation, based on the general model of Fig. 1(a). There is no necessity for determining eigenvalues whenever the profile parameters or frequency is changed as is the case for the bilinear model of Ref. 10. The computer program for the model of Fig. 1(a) uses the set of Mx_n and $h_2'(Mx_n)$ as inputs. The only special functions then which must be computed in the program, are h_2 and H_0^2 . Thus this program is much simpler than that of the bilinear profile which in addition requires the functions h_1 , h_1' , and h_2' and also requires eigenvalue iteration for each computer run. This simplicity of the present model allows double precision calculation, whereas the computation time would be prohibitive for the two-layer model.

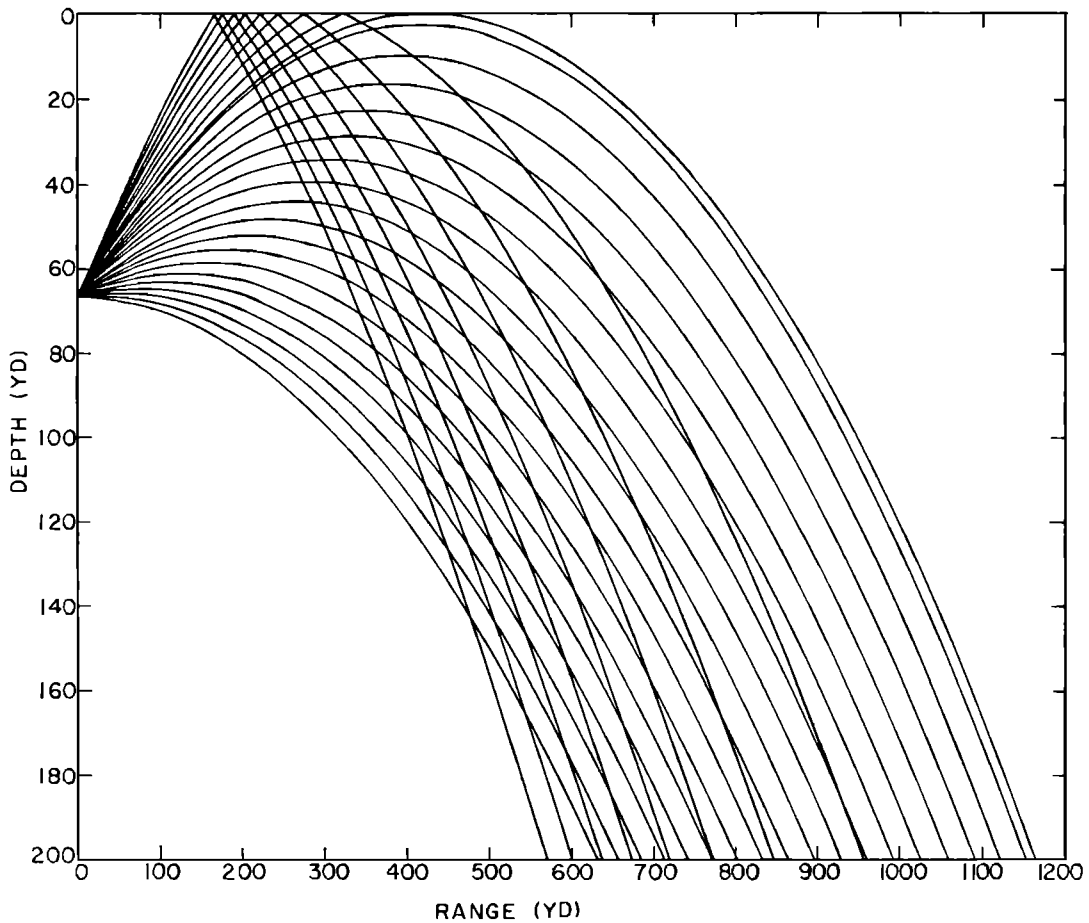


FIG. 2. Ray diagram for the profile of Fig. 1(b) and a source depth of 66.7 yd.

C. Ray Theory Solution

In this treatment the ray to be calculated is designated by the parameter C_m , the velocity at which the ray becomes horizontal. In this case, Snell's law becomes

$$\cos\theta_i = C_i/C_m, \quad (9)$$

where θ_i is the angle formed by the ray with the horizontal and C_i is the velocity at interface i . Then

$$\tan\theta_i = \pm(C_m^2 - C_i^2)^{1/2}/C_i \quad (10)$$

and $\cot\theta_i$ is the reciprocal. In Eq. 10 we choose the plus sign for downward headed rays, corresponding to positive θ_i and the minus sign for upward headed rays, corresponding to negative θ_i . By considering θ_i to take on negative values we can succinctly write expressions for all possible rays with a given C_m .

Since Fig. 1 represents a single layer situation, the value i can only take on three values: h associated with the receiver, s associated with the source, and 0 associated with the surface. Since rays cannot form nadirs or reflect from a bottom and since i can take on only three possible values, the ray theory expressions given

in Ref. 10 can be simplified to the forms presented in this section.

The presentation and discussion of the detailed ray theory forms is facilitated by a ray plot. Figure 2 presents a ray plot for the profile of Fig. 1(b) and a source depth of 66.7 yd. Rays for negative values of θ_s are plotted at 1° intervals starting at zero and ending at -25° . In addition the ray which grazes the ocean surface is also plotted. The θ_s of this ray is about -17.36° . Ray plots such as Fig. 2 are produced by a special computer run using the C_m 's corresponding to the desired source angles. For runs of propagation-loss calculation more than 125 ray parameters were used with C_m 's chosen to approximate a uniform distribution in range intervals of interest rather than to produce equal increments in source angle.

The horizontal range between source and receiver may be expressed as

$$R = 2b^{-1}C_m^{-2}(\tan\theta_h - \tan\theta_s - 2|\tan\theta_0|). \quad (11)$$

In Eq. 11 and other expressions to follow any function of θ_0 is deleted unless the ray reflects from the surface between source and receiver. Note from Fig. 2 that

θ_h is positive and θ_s is negative for a ray which reflects from the surface.

In the case of rays which do not reflect from the surface θ_h and θ_s may be positive or negative. When θ_h is positive and θ_s is negative the ray forms an apex between source and receiver. Rays with θ_h positive and θ_s positive can only occur when the receiver is deeper than the source. These rays are not plotted in Fig. 2 because they cover the region below the source at short ranges of little interest. Rays with θ_h negative and θ_s negative can only occur when the receiver is shallower than the source. Rays with θ_h negative and θ_s positive cannot occur since the rays do not form a nadir or reflect from a bottom. The angular restrictions just noted for rays which do not reflect from the surface as well as the angular restriction noted for the surface-reflected rays follow from Fig. 2 and our sign convention on θ , which depends on direction the ray is headed. It can also be verified that R of Eq. 11 is positive under these angular restrictions. One can show that if these restrictions are ignored then R of Eq. 11 turns negative and cannot be interpreted from a physical standpoint.

The travel time corresponding to Eq. 11 becomes

$$T = 2(3b)^{-1}C_m^{-3}(\tan^3\theta_h - \tan^3\theta_s - 2|\tan^3\theta_0|) + R/C_m. \quad (12)$$

The derivative term, necessary in the intensity formulation, is

$$dR/dC_m = 2b^{-1}C_m^{-3}(\cot\theta_h - \cot\theta_s - 2|\cot\theta_0|) - R/C_m. \quad (13)$$

We wish now to examine the sign of Eq. 13. For surface-reflected rays, $|\theta_0| < \theta_h$ or $|\theta_s|$. Hence $|\cot\theta_0| > |\cot\theta_h|$ or $|\cot\theta_s|$. It follows then that the first term in Eq. 13 is negative. Hence dR/dC_m is always negative for surface-reflected rays. The maximum range of the surface-reflected rays occurs for the ray which grazes the surface, $C_m = C_0$. As C_m is increased beyond C_0 , the range of the surface reflected rays decreases monotonically to zero corresponding to $C_m = \infty$.

In the case of rays which do not reflect from the surface, Eq. 13 may be written as

$$dR/dC_m = -RC_m^{-1}(1 + \cot\theta_h \cot\theta_s). \quad (14)$$

When θ_h and θ_s have the same sign Eq. 14 is negative. Thus the maximum range of a ray for θ_h and θ_s positive occurs for $C_m = C_s$. As C_m is increased to infinity the range for θ_h and θ_s positive decreases monotonically to zero. The maximum range for a ray for θ_h and θ_s negative occurs for $C_m = C_h$. As C_m is increased to infinity the range for θ_h and θ_s negative decreases monotonically to zero.

The only other possibility is when θ_h is positive and θ_s is negative, corresponding to rays which start upward at the source, form an apex, and then head downward at the receiver. In this case dR/dC_m may be positive,

negative, or zero. The caustic or envelope occurs when

$$dR/dC_m = 0. \quad (15)$$

From Eq. 14 it follows that at the caustic

$$\cot\theta_h = -\tan\theta_s, \quad (16)$$

or

$$\theta_h = 90^\circ + \theta_s = 90^\circ - |\theta_s|, \quad (17)$$

i.e., the angle the caustic forms at the receiver is the complement of the absolute value of the angle at the source. The ray parameter for the caustic ray $(C_m)_c$ may be expressed in terms of the velocity at the source and receiver.

$$(C_m)_c = (C_h^2 + C_s^2)^{1/2}. \quad (18)$$

When $C_m < (C_m)_c$, Eq. 14 is positive and the range is increasing. When $C_m > (C_m)_c$, Eq. 14 is negative and the range is decreasing. There is a further consideration. Equation 14 applies only when the rays do not reflect from the surface, i.e., when $C_m < C_0$. Thus in order for the caustic to occur,

$$(C_h^2 + C_s^2) = (C_m)_c^2 \leq C_0^2. \quad (19)$$

The largest receiver velocity for which a caustic can occur is

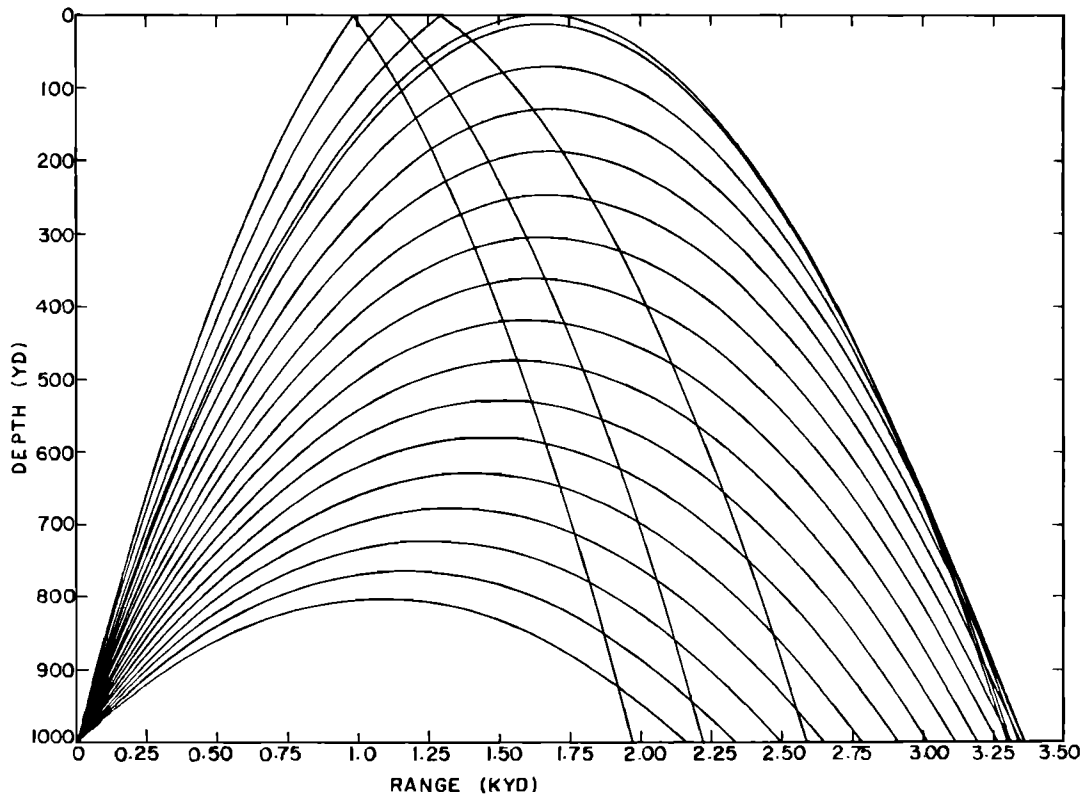
$$C_h = (C_0^2 - C_s^2)^{1/2}. \quad (20)$$

For the source and surface velocity corresponding to Fig. 2, Eq. 20 yields $C_h = 500.35$ yd/sec. This is for a receiver depth of 6988 yd, which is far deeper than shown in Fig. 2. For the receiver depths depicted in Fig. 2 there are no caustics. The rays which form an apex between source and receiver start out at minimum range for $C_m = C_s$. This range increases monotonically to a maximum value for the surface-limited ray, i.e., $C_m = C_0$.

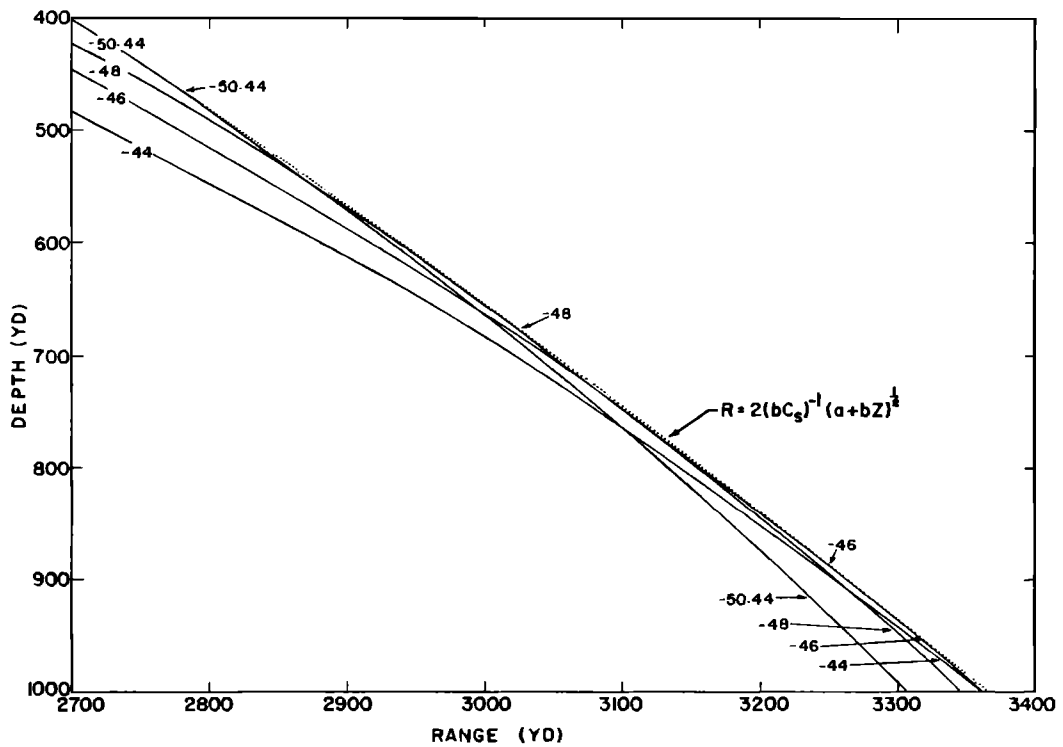
The caustic is best illustrated by treatment of a deeper source depth. Figure 3(a) presents a ray plot for a source depth of 1000 yd. Rays for negative values of θ_s are plotted at 2° intervals starting at -20° and ending at -56° . The ray which grazes the ocean surface is also plotted. The θ_s of this ray is about -50.44° . In the lower right-hand region of the ray plot, the maximum range is not determined by the ray which grazes the surface, but rather by the envelope of the family of rays.

Let us consider the relationship of the rays to the envelope in more detail. From Eq. 16, it follows that the ray with $\theta_s = -45^\circ$ touches the envelope at the source depth. Moreover rays with $|\theta_s| < 45^\circ$ or $|\theta_s| > 45^\circ$ touch the envelope at depths, deeper or shallower, respectively, than the source depth. This statement is illustrated by Fig. 3(b) which depicts four rays in the critical region of Fig. 3(a). The envelope is shown as the dotted line. The ray, $\theta_s = -44^\circ$, does not touch the envelope in the depth interval shown in Fig. 3(b), i.e., at depths shallower than 1000 yd. However, the rays with $\theta_s = -46^\circ$, -48° , and -50.44° (ray which

NORMAL-MODE AND RAY THEORY



(a)



(b)

FIG. 3. (a) Ray diagram for a source depth of 1000 yd. (b) Expanded section of Fig. 3(a), showing the relationship of four rays to the envelope. The envelope is the dotted line.

grazes surface) do touch the envelope at depths shallower than 1000 yd, which is the source depth. The points at which these three rays touch the envelope are labeled by the arrows pointing to the left.

One may obtain an explicit expression for the envelope for the evaluation of Eq. 11 for the ray parameter given in Eq. 18. Equation 11 reduces to

$$R_c = 2b^{-1}/C_s C_h. \quad (21)$$

Finally if C_h is expressed in terms of receiver depth Z , we obtain

$$R_c = 2(bC_s)^{-1}(a+bZ)^{1/2}. \quad (22)$$

The dotted line in Fig. 3(b) is a plot of Eq. 22 for the profile parameters of Fig. 1(b) and for the source velocity at a depth of 1000 yd. The dotted line in Fig. 3(b) is terminated at a depth of about -466 yd, the depth at which the ray, grazing the surface, touches the envelope. At smaller depths than this, Eq. 22 represents the envelope of the family of rays for which the ocean surface has been removed. In Eq. 22, $R_c \rightarrow 0$ as $Z \rightarrow -b/a$, which is the horizontal asymptote of the velocity profile. This is the point on the envelope corresponding to $\theta_s = -90^\circ$ and $\theta_h = 0^\circ$. In Eq. 22 $R_c \rightarrow \infty$ as $Z \rightarrow \infty$. This is the point on the envelope corresponding to $\theta_s = 0^\circ$ and $\theta_h = 90^\circ$.

Although the presence of the envelope complicates the ray diagram somewhat, one simple observation appears. For the general profile model of Fig. 1(b), there are either no rays or two rays which leave any given source depth and pass through any given point in the range-receiver depth plane. The no-ray or shadow-zone region lies at ranges beyond the envelope for deep receivers or beyond the surface-grazing ray for shallow receivers. Exactly two rays pass through each point in the region ensonified by rays. There is never just one ray and never more than two rays. The acoustic field of ray theory then is the result of the interference between two ray paths.

The relative intensity of ray theory is computed by

$$I/F = C_s |\cot \theta_s| |\cot \theta_h| / C_h C_m R |dR/C_m|. \quad (23)$$

Equation 23 is usually derived in the literature from geometric considerations. As discussed in Appendix C, Eq. 23 is equivalent to the following definition:

$$I/F = |p^2/C_h| / |p_0^2/C_s| R_0^2. \quad (23a)$$

Here R_0 is the unit distance (1 yd in our case). Definitions for I and F are discussed in Appendix C. The propagation losses of ray theory were based on

$$H_r = -10 \log(R_0^2 \sum |I/F|), \quad (23b)$$

where the summation is taken over the various ray paths. The propagation loss of Eq. 23b is in terms of sound intensity level. The quantity R_0 in Eq. 23b is often suppressed since it is of unit value and has no effect on the numerical result. We include it here and

in Eq. 23a to give proper dimensions. For example, the argument of the logarithm in Eq. 23b is now a dimensionless quantity.

For our case in Eq. 23b we use a vector sum which takes into account the phase angles of the arrivals as well as their pressure amplitudes. The ray theory propagation loss for the combination of two ray paths, 1 and 2, may be written as

$$H_r = -10 \log[(I/F)_1 + (I/F)_2 + 2(I/F)_1^{1/2}(I/F)_2^{1/2} \cos(\Psi_1 - \Psi_2)]. \quad (24)$$

The unit term R_0^2 in Eq. 23b has been suppressed in Eq. 24. Here Ψ represents the change in phase (of the pressure) which occurs between source and receiver.

The phase angles are given by

$$\Psi_1 = 2\pi f T_1 + \epsilon_1 \quad (25)$$

and

$$\Psi_2 = 2\pi f T_2 + \epsilon_2, \quad (26)$$

where T is the travel time and ϵ represents a phase shift which depends on the type of ray. For the model of Fig. 1b, the phase shift ϵ is zero for the ray types which neither reflect from the surface nor form an apex between source and receiver. These types are not treated in this article, because they cover short ranges where the mode theory is too difficult to apply.

One of the ray types, which is of interest, is the ray which forms an apex between source and receiver but does not touch the envelope between source and receiver. For this type $C_s \leq C_m \leq (C_m)_c \leq C_0$. The quantity, dR/dC_m , is positive in this interval and the range is increasing with increasing C_m . In the use of Eq. 24 we shall designate a ray of this type as path 1. For this path we consider ϵ_1 as assuming two possible values, $\epsilon_1 = 0$ and $\epsilon_1 = -\pi/2$. A comparison of the ray theory result for each of these values with the result of mode theory demonstrates that $\epsilon_1 = 0$ is the proper value.

The second of our two paths in Eq. 24 can be of two distinct classes. Class I are the rays which reflect from the surface. For this path $C_m \geq C_0$. The range is decreasing in this interval with increasing C_m . The phase shift for Class I is $\epsilon_2 = -\pi$, corresponding to perfect reflection from the free surface. The Class II rays for the second path are those rays which form an apex between source and receiver and which touch the envelope between source and receiver. For this path $C_0 \geq C_m \geq (C_m)_c$. Here again the range is decreasing with increasing C_m . For Class II rays we shall consider ϵ_2 as assuming two possible values, $\epsilon_2 = 0$ and $\epsilon_2 = -\pi/2$. A comparison of the ray theory result for each of these values with the result of mode theory will demonstrate that $\epsilon_2 = -\pi/2$ is the proper value.

We have now defined a first ray path and a second path consisting of two classes. These two paths combine to form the acoustic field of ray theory at the longer ranges. For receivers below the source, these are the ranges beyond the zero-degree ray at the source. For

receivers above the source, these are the ranges beyond the locus of ray apices. Our primary interest will be range intervals which include the shadow-zone boundary. This interval has the most significant acoustic features. Moreover, there are numerical problems in the evaluation of the mode theory at shorter ranges.

D. Field near a Caustic

At a caustic, dR/dC_m is zero and the relative intensity of Eq. 23 becomes infinite. In previous work on this problem we have followed Marsh¹⁵ who developed a diffraction correction which results in a finite relative intensity at the caustic. However, here we shall follow Brehkovskikh's treatment,⁴ which not only covers the near-caustic region ensounded by rays but also determines the field in the ray theory shadow zone bounded by the caustic. Here we only present those forms necessary for computation. Details on how to obtain these forms from Ref. 4 are presented in Appendix B.

The corrected relative intensity at the caustic is given by

$$(I/F)_c = K(C_s/C_h C_m) |\cot \theta_s| |\cot \theta_h| f^{1/2} / R |C_m d^2 R / dC_m^2|^{1/2}, \quad (27)$$

where K , a dimensionless constant, is equal to 2.32. Equation 27 is evaluated for the C_m , which is the root of $dR/dC_m = 0$. The corrected relative intensity near the caustic is given by

$$(I/F)_{\Delta R} = (I/F)_c [Ai(t)/Ai(0)]^2, \quad (28)$$

where $Ai(t)$ is the Airy integral. Equation 28 represents the corrected relative intensity at a horizontal distance ΔR from the caustic. The physical parameter ΔR is related to the dimensionless mathematical argument of the Airy integral by the relation

$$\Delta R = -Lt, \quad (29)$$

where

$$L = 0.2331 C_m (C_m d^2 R / dC_m^2)^{1/2} f^{-1/2}. \quad (30)$$

Equation 28 can be interpreted as the phased addition of the two ray paths which merge to form the caustic. For the profile of Fig. 1, there are only two paths. Hence we need not be concerned with the phase associated with the relative intensity of Eq. 28, as it represents the total field. The propagation loss at a distance ΔR from the caustic may be written as

$$H_r = -10 \log(I/F)_c - 20 \log[Ai(t)/Ai(0)]. \quad (31)$$

Equation 31 is the corrected form of Eq. 24, applying in the caustic region.

Equation 31 is easy to apply in practice. Consider Fig. 4 which is the second term of Eq. 31, plotted over $-7 \leq t \leq 3$. Figure 4 represents the propagation loss relative to the loss at the caustic. All one needs to obtain a propagation loss plot in the region of the caustic

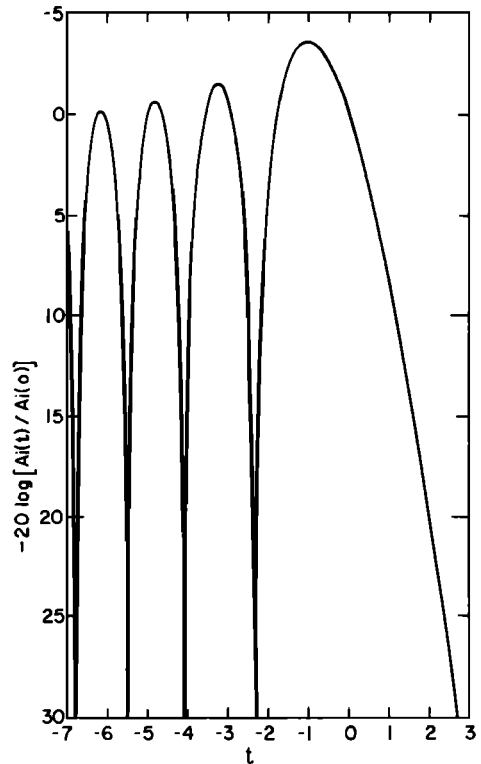


FIG. 4. Propagation loss relative to that at the caustic, represented by $t=0$.

is Fig. 4 and the numerical result of Eqs. 27 and 30. One translates Fig. 4 vertically so that 0 dB corresponds to $-10 \log(I/F)_c$, which is the propagation loss at the caustic. Equation 30 then gives the scale factor which relates t to ΔR .

The caustic is represented in Fig. 4 by $t=0$. The behavior for positive t is monotonic increasing, resulting from an exponential decrease in $Ai(t)$. For a caustic at a relative maximum in range, L of Eq. 30 is negative and positive t corresponds to a positive ΔR , which represents the shadow zone region. For a caustic at a relative minimum in range, L of Eq. 30 is positive and positive t corresponds to a negative ΔR , which represents the shadow-zone region. Thus positive t represents the shadow-zone region for both types of caustics.

The region of negative t represents the region ensounded by the two ray paths which merge to form the caustic. The beats in this region represent the interference between these two paths. Note that the minimum loss does not occur at the caustic, but occurs at a value of $t = -1.02$. An explanation for this result is provided by the $-\pi/2$ phase shift which occurs when a ray touches the envelope. Consider the schematic of Fig. 5. Vector 1 represents the contribution of the ray which has not touched the envelope, vector 2 represents the contribution of the ray which has touched the envelope, and vector R represents the resultant of 1 and

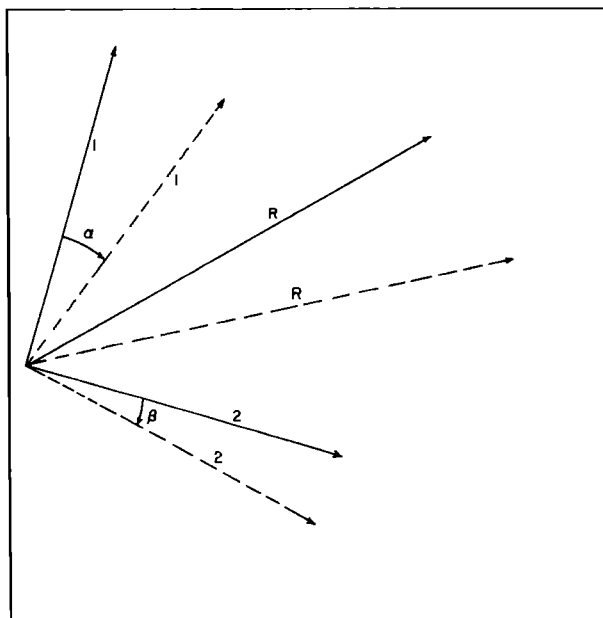


FIG. 5. Schematic representing ray contributions at the caustic (solid lines) and before the caustic (dashed lines).

2. The solid vectors represent the situation at a caustic at a relative maximum in range. Vectors 1 and 2 have equal magnitude but the phase of vector 2 is 90° less than that of vector 1. The resultant R lags vector 1 by 45° . The dashed vectors represent the situation at a range somewhat less than that of the caustic. At this shorter range the phase of both vectors 1 and 2 will be smaller than that at the caustic. However, the phase change α will not equal β .

In order to determine the relative sizes of α and β we make use of a fundamental property of the calculus of variations. From this standpoint a ray represents an extremal curve which minimizes the travel time. Jacobi¹⁶ proved that when two extremals (rays) pass through two given points (source and receiver) then the extremal which has touched the envelope between the two points cannot minimize the integral (travel time). The consequences of this theorem is that the arrival which has touched the envelope (vector 2) will always have a travel time that is greater than that of the arrival which has not touched the envelope (vector 1). The greater travel time for vector 2 represents a larger phase angle. Hence dashed 2 will be closer to solid 2 than dashed 1 is to solid 1. It follows then that $\alpha > \beta$. We note in Fig. 5 that the two arrivals are more nearly in phase and the resultant has increased for a range somewhat short of the caustic.

The minimum loss in Fig. 4 may be interpreted as occurring at (or near) a range where $\alpha - \beta = 90^\circ$, i.e., dashed vectors 1 and 2 are exactly in phase. Because of the complete cancellations in Fig. 4 it is logical that vectors 1 and 2 of Fig. 5 have equal magnitude. However, Fig. 4 also indicates that the magnitude of vectors 1 and 2 must change together as the range is decreased,

for if the magnitudes remained constant, positions of equivalent phase would be uniformly spaced in t . This is not the case in Fig. 4. Indeed we can demonstrate that the amplitude of vectors 1 and 2 is larger at the in-phase position than at the caustic. If the magnitude of the vectors remained the same then the resultant when the two vectors are in phase would be $10 \log 2 = 3.0$ dB greater than the resultant when the two vectors are 90° out of phase. This compares with a minimum value of -3.6 dB at the in phase position of Fig. 4. Thus vectors 1 and 2 must be somewhat larger at this in-phase condition than they are at the 90° out of phase position at the caustic.

In the case of the caustic at a relative minimum in range a schematic similar to Fig. 5 applies. However, the in-phase position occurs at a range greater than that of the caustic. Here the phase of dashed vectors 1 and 2 must be increased to bring them into the in-phase position.

Note that Eqs. 23 and 27 have a number of factors in common and can be related. However, Eq. 23 represents a single arrival while Eq. 27 represents the combination of two arrivals. The appropriate expression to compare with Eq. 23 is

$$(I/F)_{cu} = 2^{-1/2} (I/F)_c, \quad (32)$$

where $(I/F)_{cu}$ indicates the relative caustic intensity in an uncombined state. Equation 32 represents the contribution of one of the two equal amplitude components which are out of phase by 90° . From Eqs. 23, 27, and 32 we find that the uncombined relative intensity for each arrival at the caustic may be expressed in terms of the relative intensity of basic ray theory as follows:

$$(I/F)_{cu} = [1.64 f^3 |dR/dC_m| / |C_m(d^2R/dC_m^2)|^3] (I/F). \quad (33)$$

The expression in the brackets can be regarded as a correction factor at the caustic. Although greatly oversimplified, this is the basic idea behind the diffraction correction factor of Marsh,¹⁵ who presents a complicated correction factor which applies in the ensonified region near the caustic and which in essence reduces to the expression in the brackets of Eq. 33.

The relationship between Eqs. 23 and 27 has also been investigated by Silbiger.¹⁷ He has demonstrated that the regions, where Eq. 28 and the bracketed term of Eq. 24 apply, overlap to some extent with the solutions becoming identical at a zone near the caustic. He demonstrates that the ray theory solution of Eq. 23, with the appropriate phasing of the two arrivals, is valid up to the point at which the expression,

$$A_s(t) = \pi^{-1/2} (-t)^{-1/2} \sin[\frac{2}{3}(-t)^{3/2} + \pi/4], \quad (34)$$

becomes an inaccurate representation for $Ai(t)$. Equation 34 is an asymptotic development of $Ai(t)$, valid for large negative t .

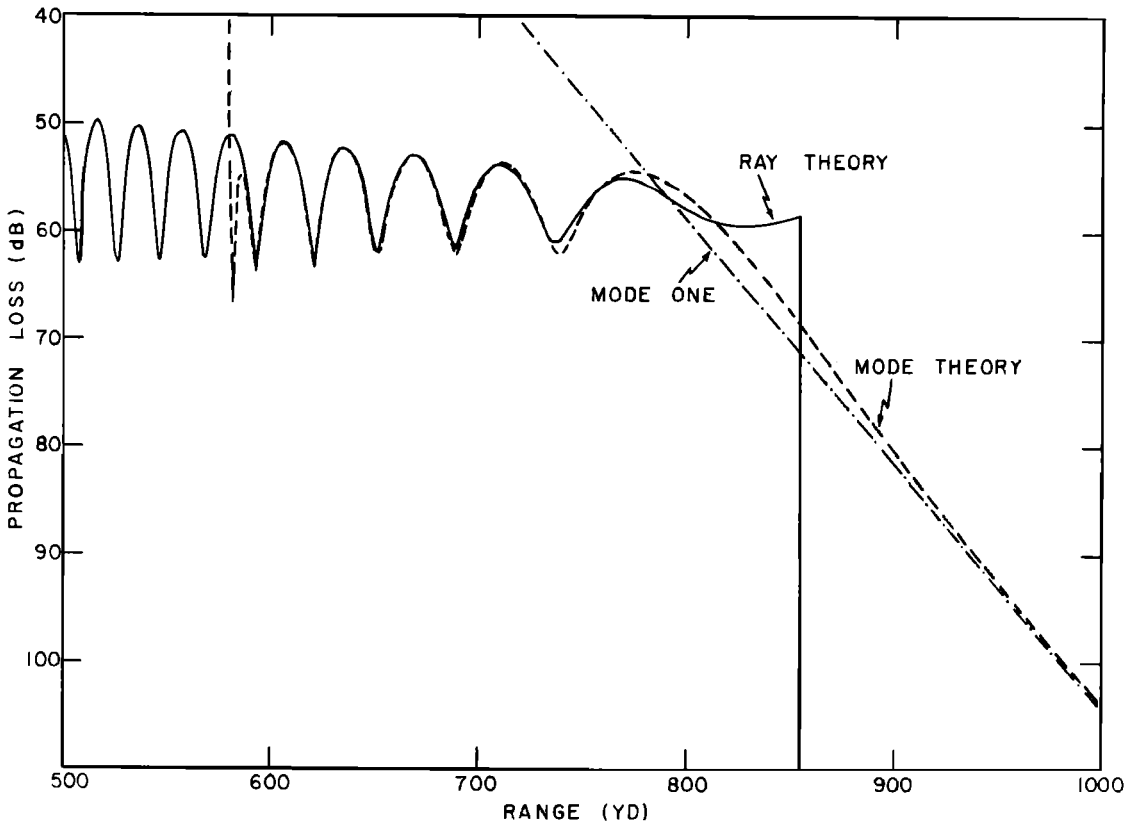


FIG. 6. Comparison of the propagation losses of ray and mode theory for a 66.7-yd source and a 66.7-yd receiver.

Expressed in terms of propagation loss, Eq. 24 will be valid with an error of less than 0.1 dB for $t < t_0$ where t_0 is the solution of

$$20 \log[A_s(t_0)/Ai(t_0)] = 0.1. \quad (35)$$

The solution of Eq. 35 as determined numerically is $t_0 = -1.29$. Thus Eq. 24 for practical purposes is valid at all ranges further removed from the caustic than ΔR_b where

$$\Delta R_b = 1.29L. \quad (36)$$

In order to evaluate Eqs. 27 and 30 for the profile model of Fig. 1, we need an expression for d^2R/dC_m^2 , which is to be evaluated at the caustic. For this model, caustics can only occur for rays, which do not reflect from the surface. Hence we may take the derivatives of Eq. 14, which may be expressed as

$$\begin{aligned} d^2R/dC_m^2 = & (dR/dC_m)^2 R^{-1} - (dR/dC_m) C_m^{-1} \\ & + R \cot \theta_s \cot \theta_h [(C_m^2 - C_s^2)^{-1} + (C_m^2 - C_h^2)^{-1}]. \end{aligned} \quad (37)$$

At the caustic Eqs. 15, 16, and 18 apply. Substitution of these into Eq. 37 leads to

$$(d^2R/dC_m^2)_c = -R_c(C_h^2 + C_s^2)/C_h^2 C_s^2. \quad (38)$$

Substitution into Eq. 27 leads to $(I/F)_c$

$$(I/F)_c = K C_s^4 C_h^2 f^4 (b/2)^{5/3} (C_h^2 + C_s^2)^{1/3}, \quad (39)$$

which may also be written as

$$(I/F)_c = K C_s^2 (2f/b)^{1/3} / (C_h^2 + C_s^2)^{1/3} R_c^2. \quad (40)$$

Substitution into Eq. 30 leads to

$$L = -0.2331 (C_h^2 + C_s^2) (R_c/C_h^2 C_s^2)^{1/3} f^{-1/3}, \quad (41)$$

which may also be written as

$$L = -0.2331 (C_h^2 + C_s^2) (2/bf^2)^{1/3} / C_h C_s. \quad (42)$$

For the profile model of Fig. 1, Eqs. 21, 40, and 41 together with Fig. 4 are sufficient to evaluate the field near the caustic.

For a given source depth we wish to determine the behavior of Eqs. 39 and 42 as a function of receiver depth. If we differentiate Eq. 39 with respect to C_h and equate to zero we find that an extremum, equal to

$$(I/F)_c = K (2f/b)^{1/3} / 3^{1/3} C_s R_c^2, \quad (43)$$

occurs at

$$C_h = 2^{1/2} C_s. \quad (44)$$

This is a maximum value. Equation 39 shows that for finite nonzero C_s , $(I/F)_c \rightarrow 0$ as $C_h \rightarrow 0$ and as $C_h \rightarrow \infty$.

If we differentiate Eq. 42 with respect to C_h and equate to zero we find that an extremum, equal to

$$L = -0.4662 (2/bf^2)^{1/3}, \quad (45)$$

occurs at

$$C_h = C_s. \quad (46)$$

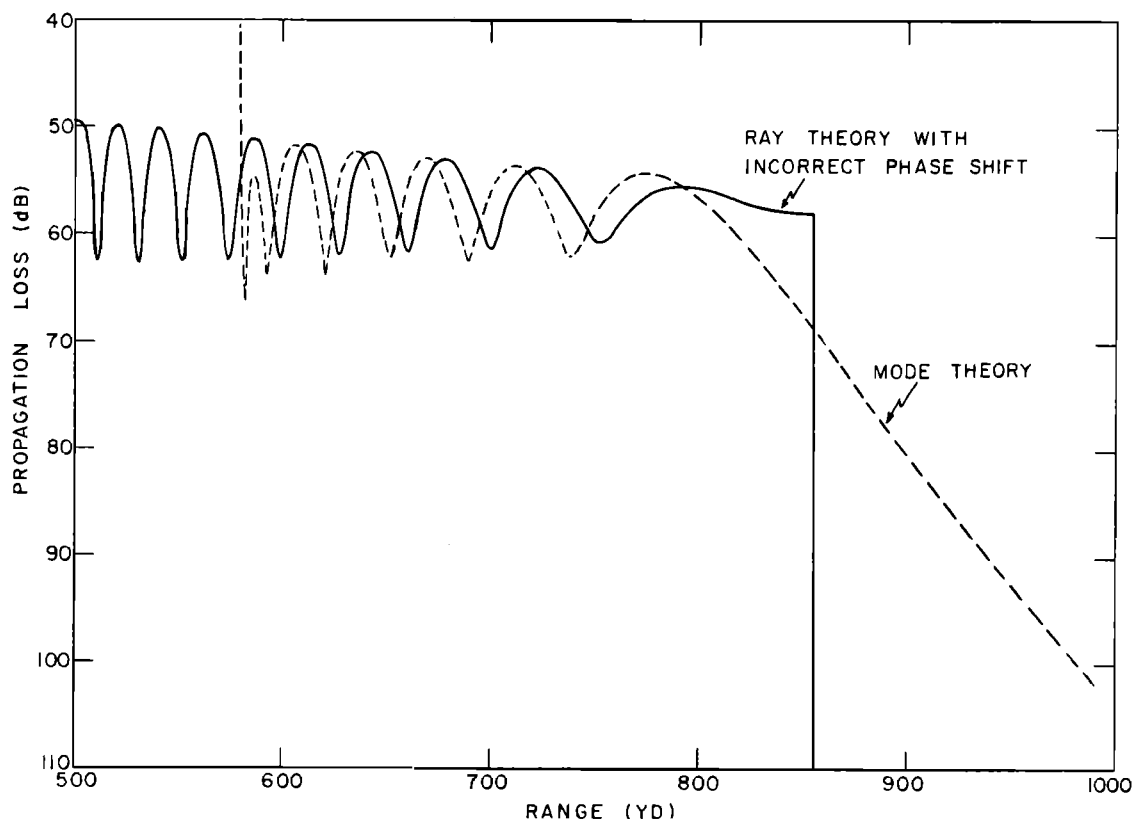


FIG. 7. Comparison similar to that of Fig. 6. The ray theory differs in that a $-\pi/2$ phase jump is introduced at the ray vertex.

This is a maximum value (minimum in absolute value). Equation 42 shows that for finite nonzero C_s , $L \rightarrow -\infty$ as $C_h \rightarrow 0$ and as $C_h \rightarrow \infty$.

II. NUMERICAL COMPARISON OF THEORIES

This section presents a numerical investigation of the various theories. All calculations are made for a frequency of 2 kHz. Shallow sources and receivers are treated first, where the mode theory readily converges. Deep sources and receivers are treated next, where convergence problems with the mode theory preclude satisfactory comparison with ray theory. Intermediate source and receiver depths are then examined and a correspondence between the rapidity of convergence of the mode theory and the presence of ray theory caustics is indicated.

A. Shallow Transducers

Figure 6 presents propagation loss for source and receiver both at a depth of 66.7 yd. The sound velocity profile is realistic at depths shallower than this, so Fig. 6 represents conditions that could be encountered in the ocean. The dashed curve is the mode theory result using the first 70 modes. The solid curve is the ray theory result with ϵ_1 of Eq. 25 equal to zero, i.e., no phase shift is associated with the ray vertex. A ray theory shadow zone exists beyond a range of 855 yd.

As shown by Fig. 2, the shadow-zone boundary for this configuration is the ray which grazes the ocean surface.

There is essentially perfect agreement between ray and mode theory in the range interval 590–680 yd. At shorter ranges the discrepancy between ray and mode theory results from the use of only 70 modes. Higher order modes could be included for this configuration with mode theory accuracy extending into shorter ranges. However, our interest here is not to extend the mode theory to shorter ranges, but to demonstrate that it agrees with ray theory over a sufficiently large interval to convince one of the accuracy of both theories. At ranges greater than 680 yd the ray theory begins to depart from the mode theory with the departure generally increasing with increasing range as the shadow zone is approached. This departure represents an inadequacy in the ray theory for the normal mode result is an exact solution because there is no branch-line integral for this model.¹⁰

Because mode 1 has the smallest mode attenuation, it will become the dominant mode at long range. The propagation loss of mode 1 is plotted in Fig. 6. It merges with the mode theory at a range of 1039 yd (just beyond the limits of Fig. 6). Beyond this range the mode solution is mode 1 as the contribution of higher-order modes has been attenuated to the point where they contribute nothing as compared to mode 1.

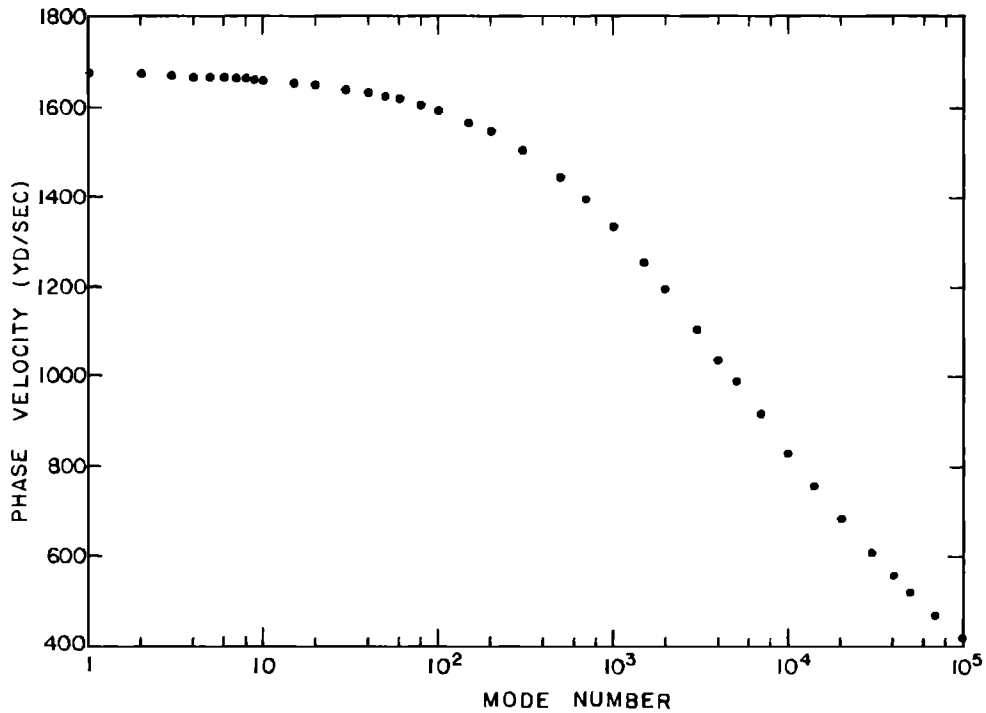


FIG. 8. Phase velocity versus mode number for 2 kHz.

Figure 7 compares mode theory with an incorrect ray theory. The mode theory is identical to that of Fig. 6. However, in the ray theory ϵ_1 of Eq. 25 was taken as $-\pi/2$ corresponding to a phase jump associated with

the ray vertex. A comparison of the good agreement between mode and ray theory in Fig. 6 to the poor agreement in Fig. 7 clearly demonstrates that the introduction of a $-\pi/2$ phase jump at the ray vertex is

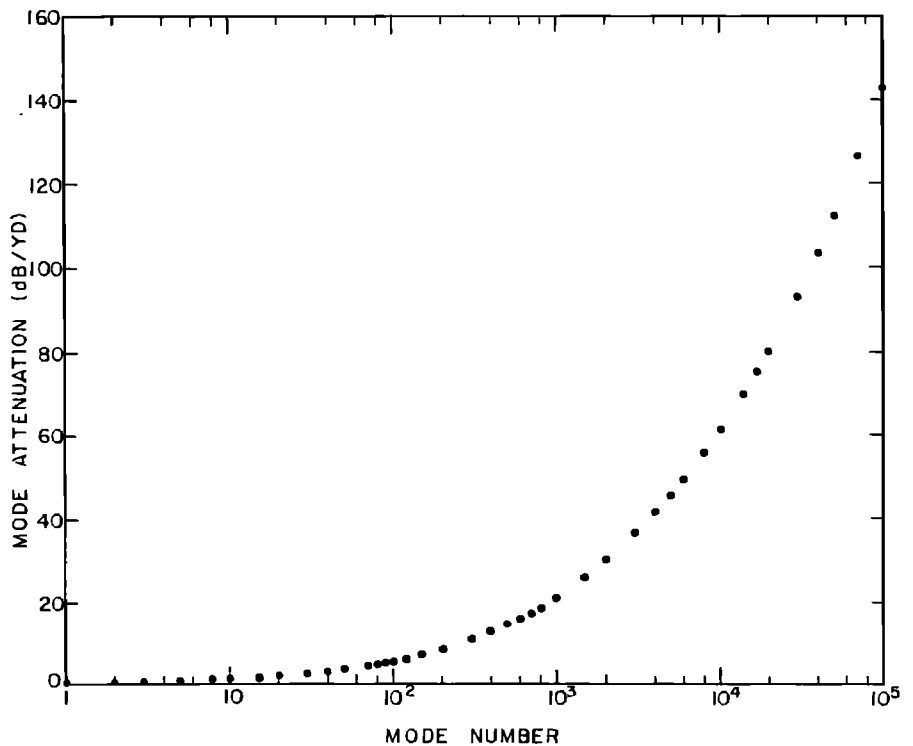


FIG. 9. Mode attenuation coefficient versus mode number for 2 kHz.

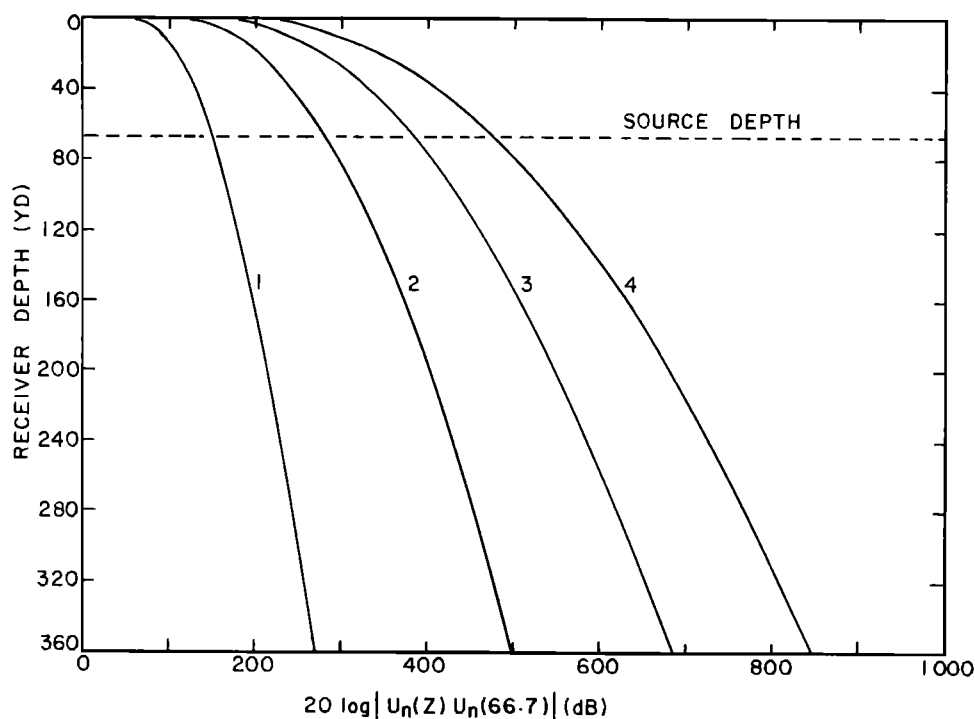


FIG. 10. Depth-function amplitudes for modes 1 to 4 for 2 kHz.

incorrect. It is true that this demonstration applies to only a particular model of the velocity profile. In this sense it is a verification of no phase jump rather than a proof. However, it is a direct demonstration, using exact solutions and avoids assumptions, approximations, and heuristic arguments.

Before the investigation of deeper transducers, it is convenient to present intermediate mode theory results on phase velocity, attenuation and mode depth functions.

The phase velocity of a normal mode is given by Eq. 21 of Ref. 1. Figure 8 presents the phase velocity at 2 kHz for the profile of Fig. 1(b) as a function of mode number. The phase velocity is smaller than the surface velocity and decreases with increasing mode number. This behavior is typical for the second family of modes illustrated in Fig. 10 of Ref. 1. In Ref. 1 by means of the phase velocity, the first and second families of modes were associated with ray groups that, respectively, do or do not reflect from the ocean surface. However, we can now demonstrate that the association between rays and modes through phase velocity can be fallacious. All modes for the profile of Fig. 1(a) have phase velocities which are less than the surface velocity. All of the modes would then correspond to rays which do not reflect from the surface. However, one of the two ray paths which form the interference pattern of Fig. 6, reflects from the surface. Which modes correspond to this path if all modes correspond to rays which do not reflect from the surface? The root of this problem lies in the difficulty of the physical interpretation of modes when the imaginary part of the eigenvalues (i.e., the attenuation) is large. We shall see further examples of this difficulty presently.

Figure 9 presents the mode attenuation coefficient as given by $-8.686 \text{ Im} \lambda_n \text{ dB/yd}$. The attenuation increases monotonically with mode number. These

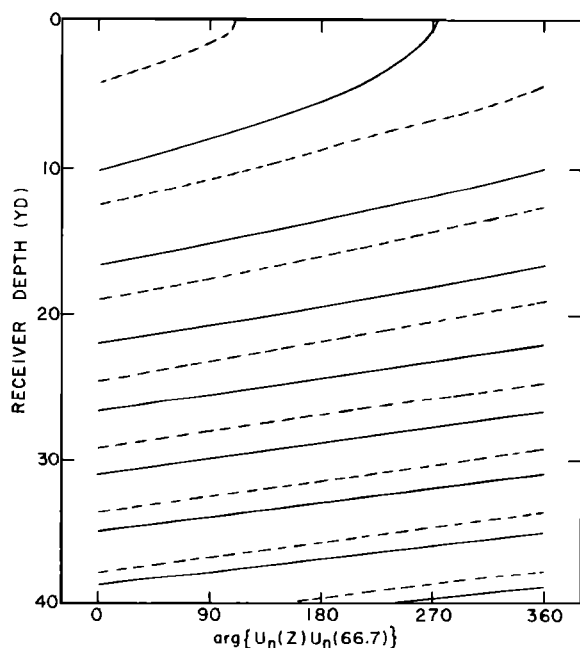


FIG. 11. Depth-function phase for 2 kHz. The solid and broken curves are for modes 1 and 4, respectively.

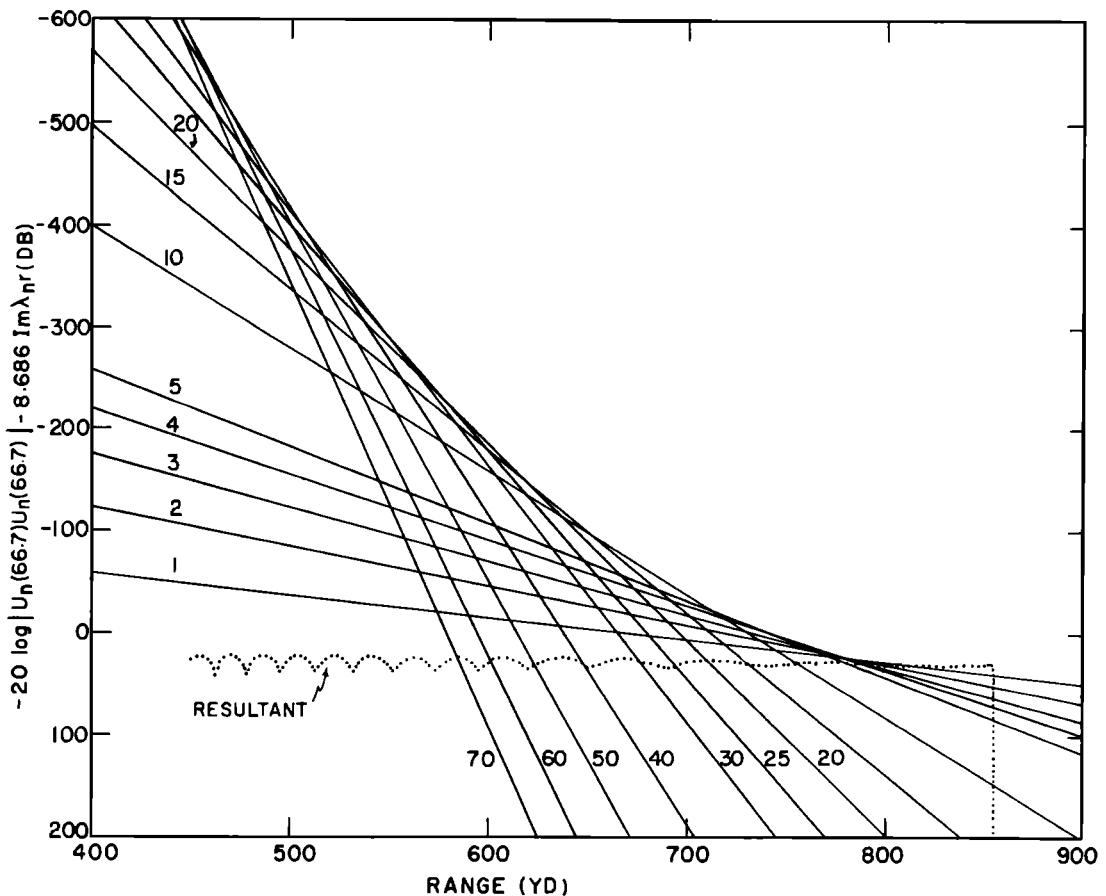


FIG. 12. Relative contribution of individual modes designated by numbers next to lines, as a function of range for a 66.7-yd source and a 66.7-yd receiver. The resultant is determined by ray theory.

attenuations are extremely large. The attenuation for mode 1 is 2.22×10^{-1} dB/yd. Contrast this figure with the mode 1 value of 7.44×10^{-6} dB/yd at 1.03 kHz for the S.S. profile of Ref. 10 or of 1.04×10^{-3} dB/yd at 1.5 kHz for the profile of Ref. 1.

Figure 10 presents the depth-function amplitudes for the first four modes and a source depth of 66.7 yd. The functions are zero at the surface and increase monotonically with depth. This general behavior is illustrated for a similar problem in Fig. 188 of Ref. 4. These amplitudes are huge compared to those of our previous investigations, illustrated by Figs. 8–10 of Ref. 10 and Fig. 13 of Ref. 1.

Figure 11 presents the phase of the depth functions for modes 1 and 4 and a source depth of 66.7 yd. The behavior is typical for downgoing waves (i.e., in the region below the channel of a two-layer profile) illustrated by Figs. 11 and 12 of Ref. 10 and Fig. 14 of Ref. 1.

The large depth-function amplitudes of Fig. 10 can be related to the large attenuation coefficients of Fig. 9. Whenever the attenuation coefficients are large the depth-function amplitudes must also be large—otherwise the modes will make no contribution at ranges of importance. This feature is illustrated by Fig. 12 which

presents the relative contribution of individual modes, corresponding to the source and receiver configuration of Fig. 6. This type of plot and its utility are discussed in detail in Secs. II-D, II-E, and II-G of Ref. 1. In brief, the solid curves of Fig. 12 are straight lines with slopes equal to the negative of the attenuation coefficients of Fig. 9. The intercept of the lines at zero range represents the negative of the depth-function amplitudes of Fig. 10 at a receiver depth equal to 66.7 yd. The resultant, as determined by ray theory, is given by the dotted line.

The pattern of Fig. 12 is very similar to that of the second family of modes in Fig. 15 of Ref. 1. However, the ordinate of corresponding modes in Fig. 12 is considerably larger than in Fig. 15 of Ref. 1. The contribution of individual modes is large compared to the resultant at ranges of interest. For example, at a range of 590 yd the maximum contribution of an individual mode is about 235 dB greater than the resultant. The analysis of Sec. II-G of Ref. 1 indicates that in order to obtain an accuracy of 0.1 dB in the resultant the error in the contribution of the largest mode must be less than $2.1 \times 10^{-12}\%$. This degree of accuracy can be obtained on the CDC 1604 computer only by the

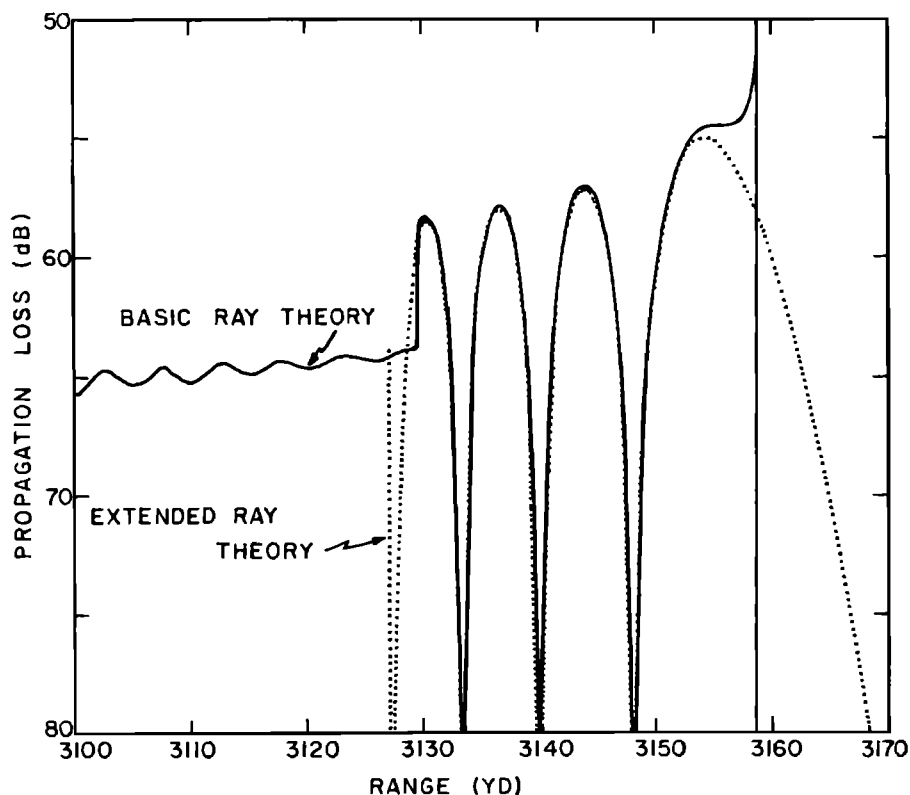


Fig. 13. Comparison of basic ray theory and an extended ray theory modified by diffraction for a 1000-yd source and an 800-yd receiver.

use of a double-precision arithmetic as previously discussed.

Note in Fig. 12 that at a range of 590 yd the contribution of mode 70 is about 20 dB less than the resultant. The analysis, presented in Sec. II-E of Ref. 1, indicates that this 20-dB difference is compatible with the fact that the mode solution in Fig. 6 begins to lose accuracy at shorter range because of the omission of modes of higher order than 70.

B. Deep Transducers

After our initial success with the propagation losses for shallow transducers, we proceeded to investigate a deep transducer configuration of 1000-yd source and 800-yd receiver. Our interest was to verify, by comparison with the mode theory solution, that there was a $-\pi/2$ phase jump at the ray theory caustic. From Figs. 3(a) and (b) we see that an 800-yd receiver is well into the region where the shadow zone boundary is a caustic.

Let us now compare the basic ray theory (Sec. I-C) with the extended ray theory (Sec. I-D) that applies near a caustic. (The normal-mode solution poses a problem that is best treated later.) The solid curve of Fig. 13 is the result of basic ray theory with ϵ_1 of Eq. 25 equal to zero, as established by the comparison of Figs. 6 and 7, and with ϵ_2 of Eq. 26 equal to $-\pi/2$ for $C_0 \geq C_m$ and equal to $-\pi$ for $C_m \geq C_0$. This choice for ϵ_2 corresponds to a -90° phase jump when the ray touches the caustic and a -180° phase jump when the

ray reflects from the surface. The dotted line is an application of the theory of Sec. I-D.

Consider first the basic ray theory result. In Fig. 13 the ray theory caustic and shadow-zone boundary occurs at a range of about 3159 yd. The ray which grazes the surface encounters the receiver at a range of about 3130 yd. The interval between 3130 and 3159 yd is characterized by the strong interference between two nonsurface-reflected arrivals of near equal amplitude. There is an abrupt increase in loss at 3130 yd, corresponding to the replacement of one of these nonsurface-reflected arrivals by a surface-reflected arrival of zero amplitude. Here this change is 5.6 dB, and corresponds to the removal of one of two equal-amplitude arrivals occurring at 3130 yd, where the difference in phase angle is 36° . A result of the basic ray theory is that the ray which barely reflects from the surface has zero relative intensity. The relative intensity of the surface-reflected arrival gradually increases as the range is decreased from that of the ray which just grazes the surface. This explains why the interference pattern between arrivals in Fig. 13 has such a small beat amplitude at ranges just less than 3130 yd and also why the interference builds up as the range decreases. This buildup in the amplitude of the beat pattern with decreasing range is characteristic of the region before the range of the surface-grazing ray. It will also appear in other examples to be presented later.

Consider now the dotted curve of Fig. 13. This curve is identical to that of Fig. 4, but with appropriate

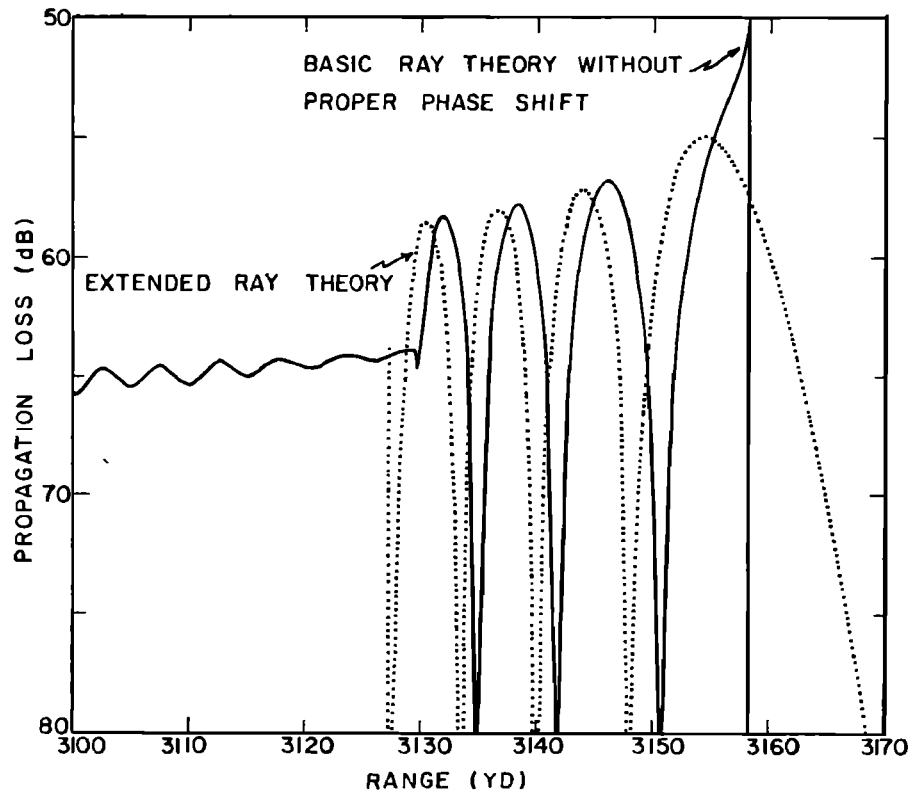


FIG. 14. Comparison similar to that of Fig. 13. The basic ray theory differs in that no phase shift is introduced when the ray touches the envelope.

translations and scaling. The range of the caustic, 3158.8 yd, corresponds to $t=0$ in Fig. 4. The propagation loss at the caustic, 58.6 dB, corresponds to 0 dB in Fig. 4. The scale factor, L , of Eqs. 30 and 41 is -4.608 . The ΔR_b of Eq. 36 becomes -5.9 yd. Thus the solid curve of Fig. 13 should start to depart from the dotted curve at $R_c + \Delta R_b = 3152.9$ yd. This is indeed the case. Thus Fig. 13 provides a numerical verification of analysis presented in Eqs. 34–36. An analysis of the exact region of validity of Eq. 31 is beyond the scope of this article. In Fig. 13 the two solutions are for practical purposes identical between the range of the surface-grazing ray and $R_c + \Delta R_b$. Obviously, Eq. 31 cannot apply in the region where one of the arrivals is surface reflected. It is gratifying, and to some extent surprising, to find in Fig. 13 agreement over several beats of the interference pattern.

Figure 14 compares the extended ray theory with an incorrect basic ray theory. The extended ray theory is identical to that of Fig. 13. However, in the basic ray theory, ϵ_2 of Eq. 26 was taken as zero for $C_0 \geq C_m \geq (C_m)_c$. This choice for ϵ_2 corresponds to no phase jump when the ray touches the caustic. It should be pointed out that Figs. 13 and 14 do not constitute an independent verification of -90° phase jump at a caustic. We have only demonstrated that the choice of $\epsilon_2 = -\pi/2$ is compatible with the extended ray theory of Sec. I-D. It remains to be demonstrated that the result of normal mode theory agrees with this choice. At ranges less than that of the surface-grazing ray the solid curves of

Figs. 13 and 14 are identical. Note in Fig. 12 that there is a small decrease in loss of 0.8 dB at 3130 yd, corresponding to the replacement of one of the nonsurface-reflected arrivals by a surface-reflected arrival of zero amplitude. This corresponds to the removal of one of two equal-amplitude arrivals occurring at 3130 yd, where the difference in phase angle is 126° .

Although the ray theory of Fig. 13 posed no additional computational problems as compared to the ray theory of Fig. 6, investigation revealed that the normal-mode solution posed an insurmountable computational problem. This problem is illustrated by Fig. 15, which is the deep transducer counterpart of Fig. 12. The dotted curve of Fig. 15 is the equivalent of the solid curve of Fig. 13. A comparison of Fig. 15 with Fig. 12 shows two important differences. In Fig. 15 over ranges of interest, individual mode contributions are much greater than the resultant as compared to Fig. 12. A second difference is the monotonic nature of the pattern of Fig. 12 as compared to the folded-over nature of the pattern in Fig. 15. In Fig. 12 the pattern moves in to shorter ranges with increasing mode number. In Fig. 15 the pattern starts to move out in range, reverses at about mode 2000 and then moves back in to shorter ranges with increasing mode number. The nature of the folded-over pattern will become clearer when we investigate intermediate depth transducers. In Sec. III we relate this pattern to the presence of the ray theory caustic.

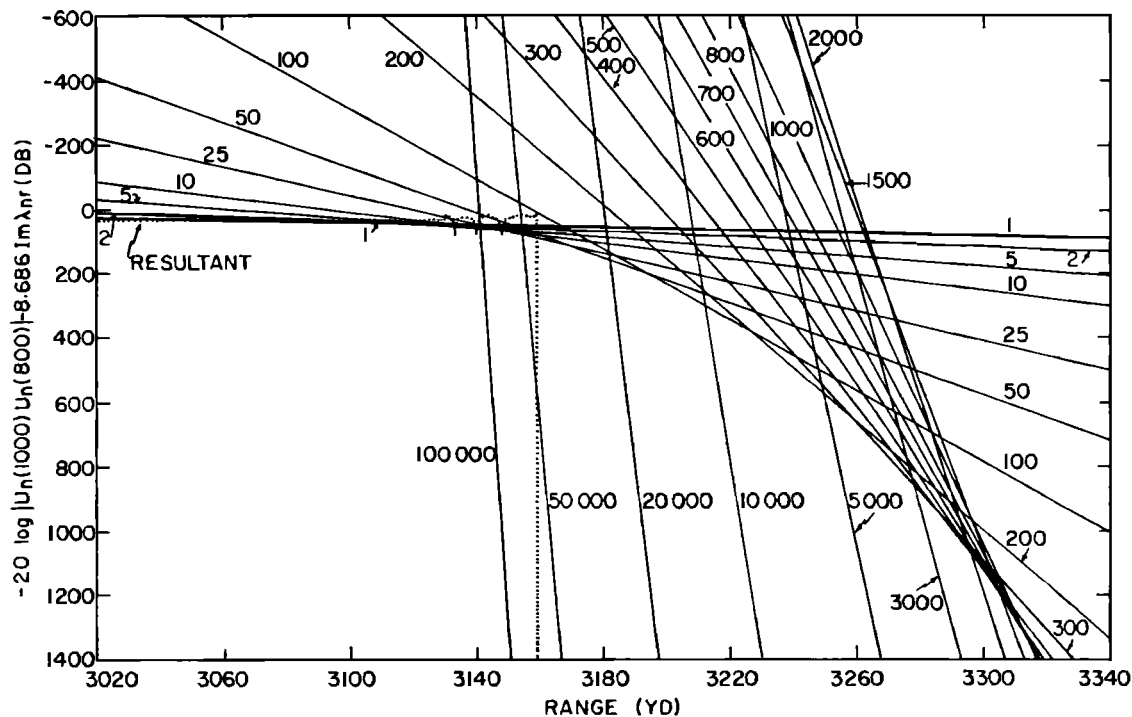


FIG. 15. Relative contribution of individual modes as a function of range for a 1000-yd source and an 800-yd receiver. The resultant is determined by ray theory.

The full extent of the computational problem is not apparent from Fig. 15. Figure 16 presents the relative contribution of the individual modes as a function of mode number for one fixed range. The particular range

chosen is at the ray theory caustic. Mode number is plotted on a logarithmic scale to accommodate both small and large numbers. Although mode number is a discrete variable and only a sparse sampling of mode

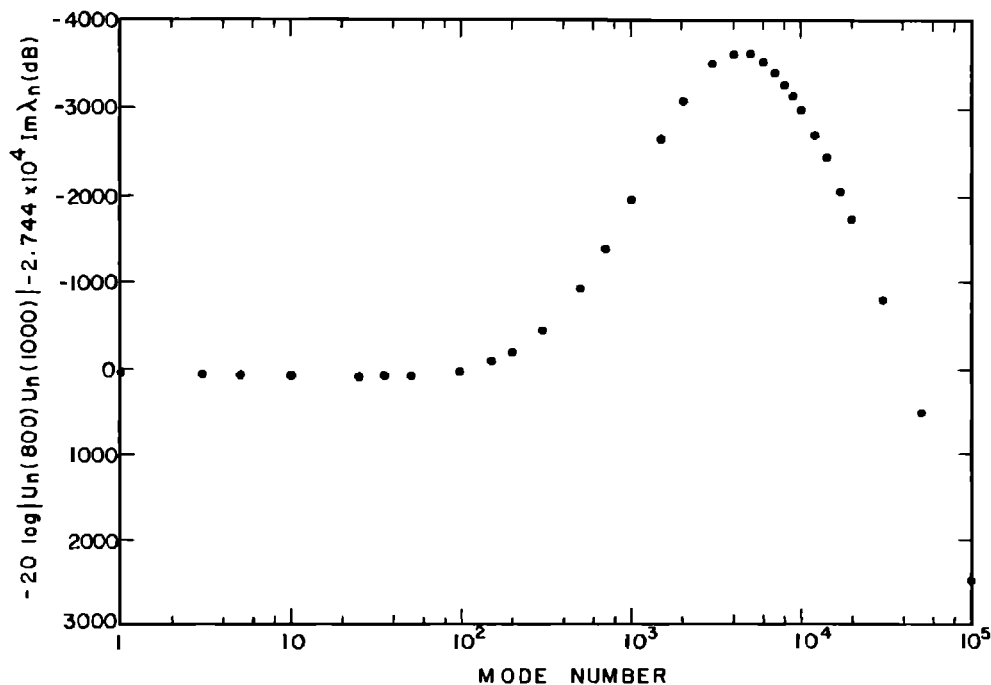


FIG. 16. Relative contribution of individual modes at the range of the caustic as a function of mode number for a 1000-yd source and an 800-yd receiver. The range is 3159 yd and the resultant, as determined by extended ray theory, is 25 dB.

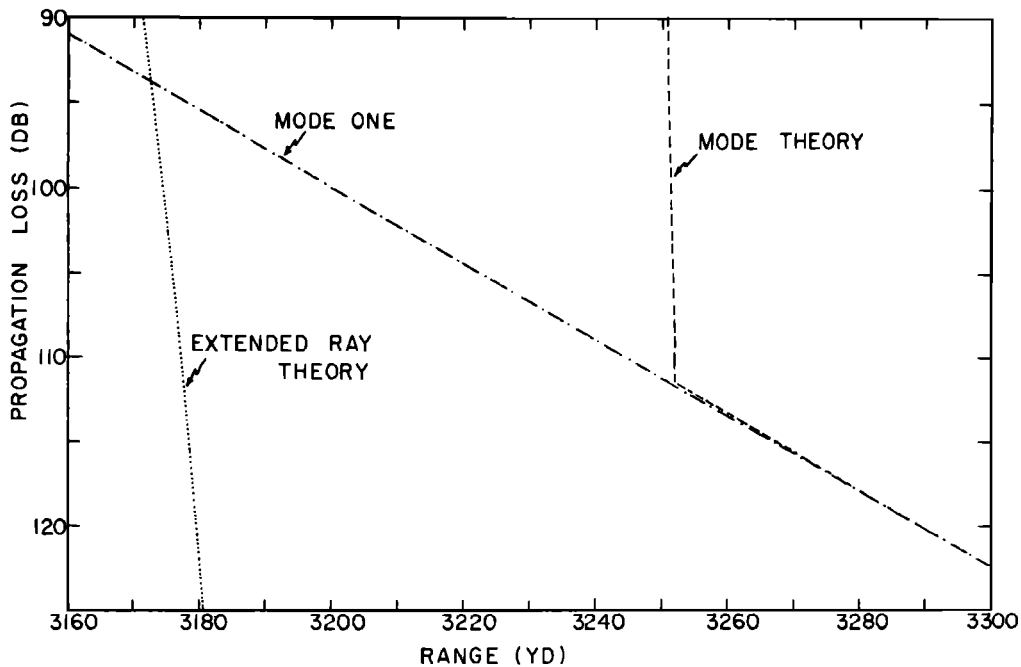


Fig. 17. An attempt at the comparison of mode theory and extended ray theory for a 1000-yd source and an 800-yd receiver. The regions of solution accuracy or validity do not overlap.

numbers is plotted, it is apparent that the points lie on a smooth curve. As the mode number is increased from 1 the contribution of a mode initially decreases. A relative minimum of 88 dB occurs for mode 25. As the mode number is increased further the contribution increases and a relative maximum of about -3630 dB occurs between modes 4000 and 5000. As the mode number is increased further, the contribution decreases monotonically.

The propagation loss at the caustic was determined from $-10 \log(I/F)_c$ and Eq. 40. This loss was 58.6 dB and corresponds to a Fig. 16 resultant of 24.9 dB as determined by Eq. 40 of Ref. 1. Applying the theory of Ref. 1, we determine that only the modes in Fig. 16 with values less than 63.7 dB can make an effective contribution to the resultant. Figure 16 indicates then that some 43 000 modes would be required to make an accurate computation at the caustic range. The maximum mode contribution is about 3660 dB larger than the resultant. Accurate computations for this situation then would require a computer word length in excess of 183 decimal digits. It is evident that here the normal mode computation lies beyond the present state of computer capabilities.

Although normal-mode computations at the caustic are impossible, Fig. 15 indicates that computations beyond 3260 yd were well within the capability of the computer. This range region was examined and the results of Fig. 17 obtained. The dashed curve of Fig. 17 presents the mode theory result using modes 1-3700. The rapid decrease in the propagation loss of this result at ranges less than about 3252 yd is an artifact

resulting from roundoff error in the mode calculation. The propagation loss for mode 1 in Fig. 17 merges with the dashed curve at a range of 3280 yd. The dotted line in Fig. 17 is a continuation of the dotted line of Fig. 13 into the region of 90- to 125-dB loss. Unfortunately the mode theory result cannot be calculated into the caustic region where comparison with extended ray theory is possible. However, such a comparison is possible for shallower source depths and will be considered in Sec. II-C.

Before completing this section the nature of the mode solution at a range of 3254 yd, the smallest range for which accurate computations were made, is of interest. Figure 18 presents various propagation losses for this range as a function of mode number. The dots represent the propagation loss associated with individual modes. The open circles represent the propagation loss associated with the partial sums of the modes, i.e., the sums from one to the indicated mode number.

Consider the dots of Fig. 18. The behavior in essence is the same as depicted in Fig. 16. The contribution of individual modes initially decreases as the mode number is increased from one. A relative minimum in mode contribution is formed and then the contribution begins to increase. (This minimum was not established nor is it shown in Fig. 18 because the loss for modes between mode 6 and mode 850 exceeded 200 dB and could not affect the resultant.) The contribution of individual modes then forms a relative maximum near mode 2000. The contribution then decreases monotonically with

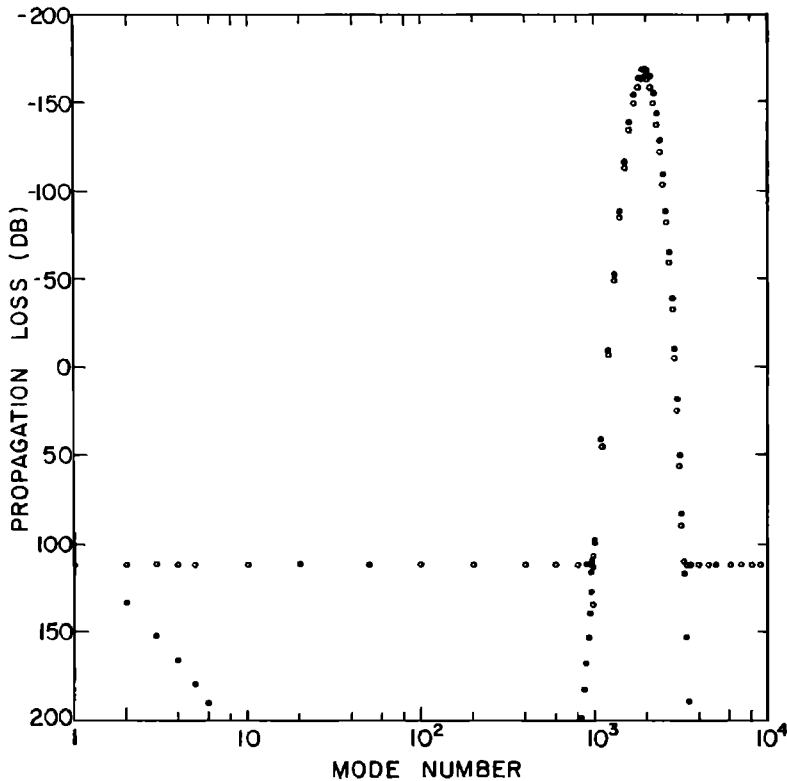


FIG. 18. Propagation loss for a 1000-yd source and an 800-yd receiver at a range of 3254 yd as a function of mode number. Dots are for individual modes while open circles are for partial sums.

increasing mode number. The loss exceeds 200 dB for mode numbers greater than about 3500.

Consider now the propagation loss of the partial sums, i.e., the open circles of Fig. 18. The value for mode 1 as determined from computer printout is 111.92 dB. The value for mode 4 is 111.88 dB. The value of the partial sum then remains essentially constant at this value until about mode 900. Here the contribution of individual modes again becomes important and the partial sum changes with considerable detail which cannot be shown in Fig. 18. As the relative maximum in individual mode contributions is formed, the partial sum exhibits the same behavior but with somewhat greater loss. After this maximum contribution, the propagation loss for the partial sums increases until the individual contributions make no difference in the resultant. The resultant remains constant at 111.90 dB for all modes beyond mode 3480.

The interesting feature of this investigation is that the summation of all the modes beyond mode 4 made a difference of only 0.02 dB in the resultant. Thus modes 900–3480, which form the prominent peak in the contribution of individual modes, almost completely annihilate each other by appropriate phasing. This is surprising when one considers that the mode of maximum contribution (mode 1947) has an amplitude which is 280 dB above the resultant.

Additional details on the individual mode contributions and partial sums, which can be only grossly presented in Fig. 18, are of interest. This detail is facili-

tated by the vector representations of Fig. 19, which are given in linear units. In this plot the vectors (the lines in Fig. 19), which represent individual mode contributions, are placed end to end with the vector from the origin to the point representing the partial sum. The quantities of Fig. 19 are related to those of Fig. 18 by

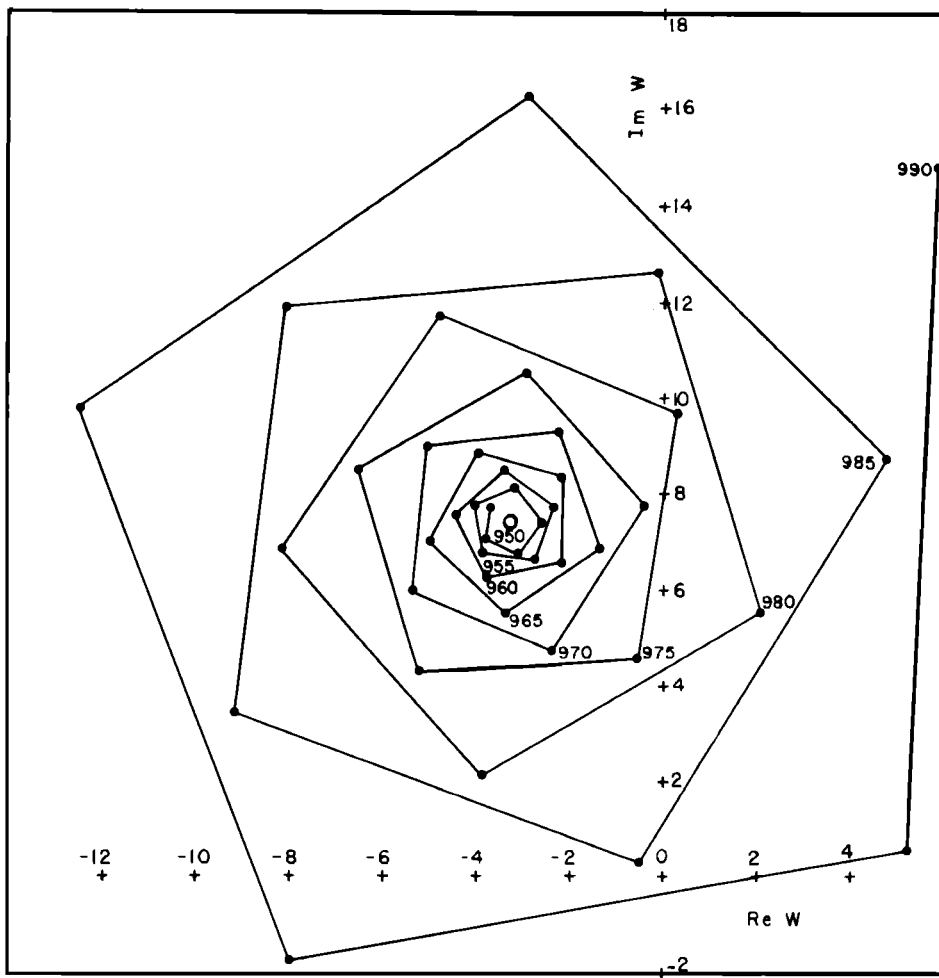
$$H_n = -20 \log |A_n| - 20 \log r \quad (47)$$

and

$$H_i = -20 \log |W_i| - 20 \log r. \quad (48)$$

Here H_n is the propagation loss associated with mode n , i.e., the dots of Fig. 18; $|A_n|$ is the amplitude of mode n , i.e., the length of the lines in Fig. 19; H_i is the propagation loss associated with partial sums, i.e., the open circles of Fig. 18; and $|W_i|$ is the amplitude of the partial sums, i.e., the distance from the points in Fig. 19 to the origin.

Figure 19(a) presents a section of the initial buildup of mode contributions as the peak of Fig. 18 is approached from the left. The open circle represents the partial sum for mode 900 which is essentially the same as that for mode 4 as indicated in the discussion of Fig. 18. As the mode number is increased beyond 900 the points of Fig. 19(a) spiral counterclockwise and outward from the open circle. As one can see the behavior of the partial sums in this section is quite complicated since the distance of the points from the origin jumps about. This explains why the open circles in Fig. 18 appear somewhat erratic in this region.



(a)

FIG. 19. Contributions of modes at a range of 3654 yd. The lines are a vector representation of the mode contribution in linear units. The vectors from the origin to the points represent the partial sum,

$$W_i = \sum_{n=1}^i H_0^2(\lambda_n r) U_n(Z) U_n(Z_0).$$

(a) Modes 950-990. (Scale: 1 unit = 10^{-7} .)

Figure 19(b) presents a section of vector diagram which includes the peak of Fig. 18. A comparison of scales shows that the vectors of Fig. 19(b) are some 14 orders of magnitude larger than those of Fig. 19(a). In Fig. 19(b) the vectors move about the origin since the resultants (open circles) of Figs. 19(a) and (b) are indistinguishable from the origin on the scale of Fig. 19(b). The points of Fig. 19(b) are moving in a counter-clockwise direction as in Fig. 19(a). The mode with maximum amplitude of partial sum is mode 1943. Thus the points spiral outward from the origin for mode numbers less than 1943 and spiral inward toward the origin for mode numbers greater than 1943. The mode of maximum contribution is mode 1947. Thus the length of the lines in Fig. 19(b) increases for mode numbers less than 1947 and decreases for mode numbers greater than 1947. We note in Fig. 19(b) that the length of the

lines is longer than the distance of the points from the origin. This indicates why, in this region, the dots of Fig. 18 lie above the open circles.

Figure 19(c) presents a section of the mode contributions as the peak of Fig. 18 is departed to the right. To simplify the figure, the lines are not drawn for mode numbers beyond 3260. The open circle represents the partial sum for mode 3480, which is in essence, the resultant for all modes. The scale of Figs. 19(c) and (a) are the same. The lengths of the lines joining the points of Fig. 19(c) decrease monotonically with the points converging to the open circle.

Figures 19(a)-(c) indicate the manner in which modes 900-3480 almost completely annihilate each other. However, they shed no light on the seemingly purposeless presence of modes which, in a practical sense, annihilate each other. In order to investigate this

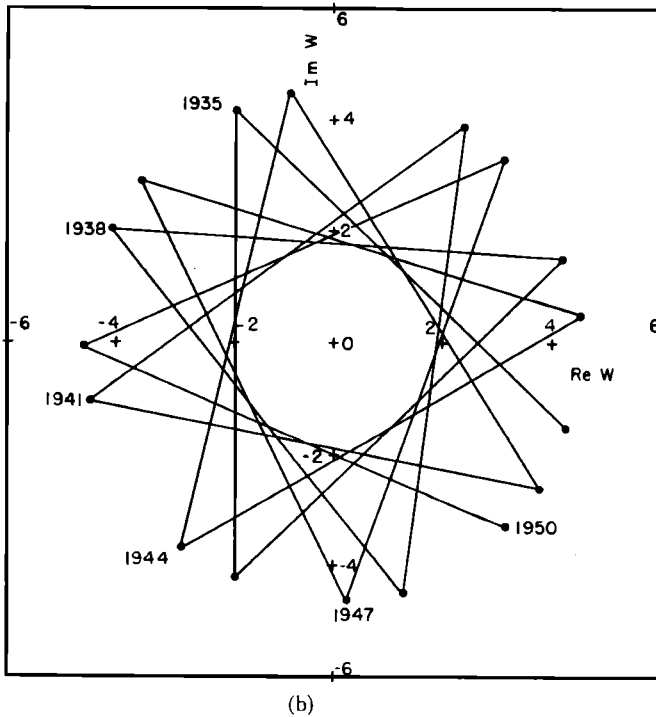


FIG. 19 (Continued). (b) Modes 1935-1950. (Scale: 1 unit = 10^7 .)

problem and others related to the caustics we must investigate intermediate depth transducers where hopefully the region of validity or accuracy of the extended ray theory and normal-mode theory overlaps.

C. Intermediate Depth Transducers

Since the mode theory computational problems become unmanageable for deep transducers, we decided to investigate transducer depths between the conditions of Secs. II-A and -B. The basic idea was to keep the transducers as shallow as possible, but deep enough so that a caustic was formed. This occurs when the caustic ray is the surface-grazing ray or from Eq. 18 when

$$C_0 = (C_h^2 + C_s^2)^{1/2}. \quad (49)$$

The shallowest configuration for the combination of source and receiver occurs when they are at the same depth, i.e., when

$$C_s = C_h = C_0/2^{1/2}. \quad (50)$$

For the profile of Fig. 1, the velocity of Eq. 50 corresponds to a depth of 682.5768 yd.

However we did not want to confine the investigation to the conditions of Eq. 50 because this represents an atypical case where only one ray path which arrives at the receiver has the high relative intensities associated with the caustic region. This is a transitional case and we should not anticipate the strong beat pattern of Fig. 4, associated with a typical well-developed caustic.

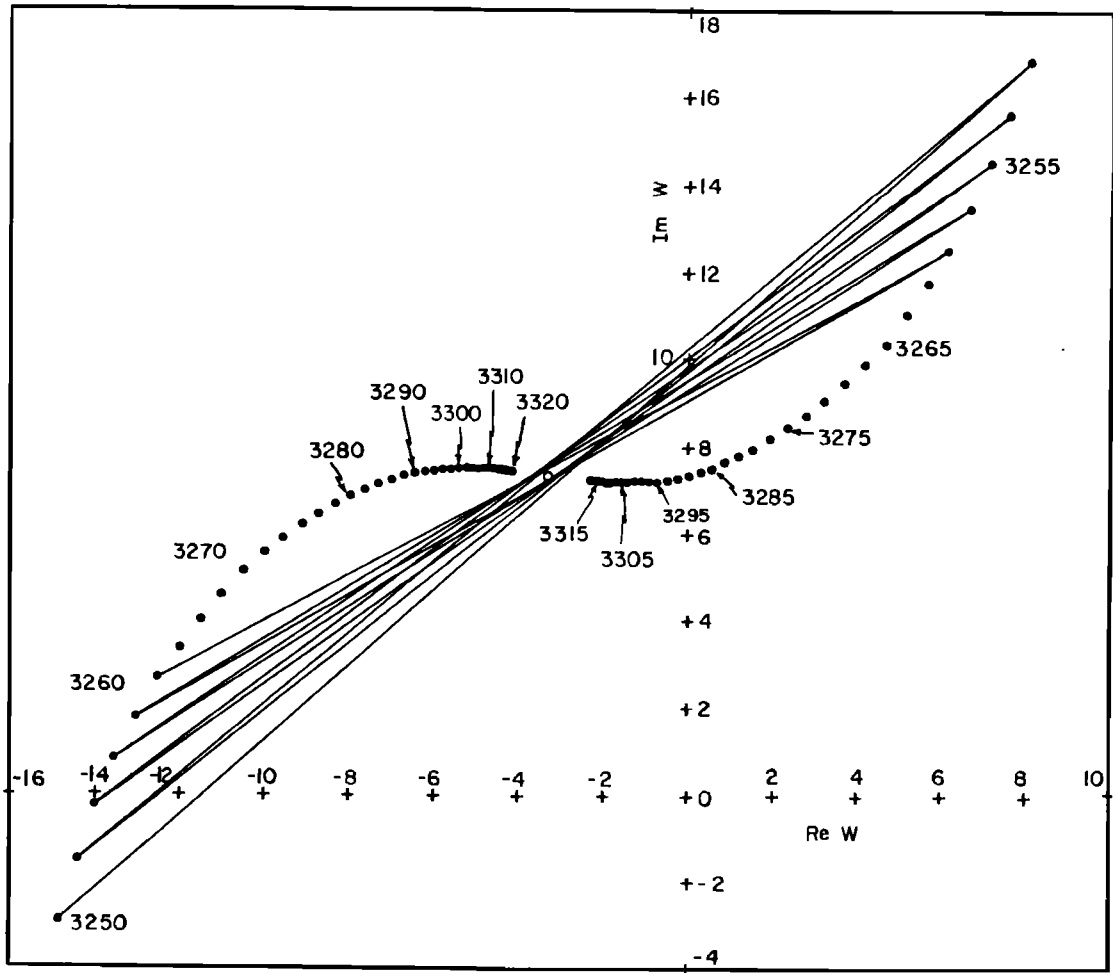
Our plan of procedure then was to fix the source depth at 682.5768 yd and to examine a variety of receiver depths, starting with a shallow depth where

there was no caustic and where we anticipated a manageable mode-theory computation problem. If this computation proved feasible, we would then proceed to successive deeper receivers until we encountered prohibitive computational problems. Hopefully this would not occur until the receiver depth was well into the region where a well-developed caustic is formed.

The acoustic field of mode theory is a continuous function of range and receiver depth. Thus as the receiver depth is increased from a shallow value the acoustic field should change in a gradual and continuous fashion from a condition comparable to that of Sec. II-A to a condition comparable to that of Sec. II-B. By observing the progressive changes with receiver depth, we would gain insight into the transition from one condition to the other. In particular we were interested in how a folded mode contribution pattern, such as that of Fig. 15, arises from a simple mode contribution pattern such as that of Fig. 12. We also wished to determine if this folded pattern is associated in some way with the ray theory caustic.

With this background we now proceed to Fig. 20 which compares ray and mode theory for the 682.5768-yd source and a 200-yd receiver. We note immediately that there appears to be a vertical displacement between results with the ray theory losses about 1 dB greater than the mode theory losses.

The answer to this discrepancy lies in a subtle difference in the conversion from velocity potential to intensity. The comparison should not be made between H_r (the ray theory loss of Eq. 24) and H_s (the mode theory loss of Eq. 6). The appropriate comparison be-



(c)

 FIG. 19 (Continued). (c) Modes 3250-3320. (Scale: 1 unit = 10^{-7} .)

tween H_r and H_e is

$$H_r = H_e + 10 \log(C_h/C_e), \quad (51)$$

where the ratio of velocities represents the index of refraction at the receiver. A derivation and discussion of Eq. 51 is presented in Appendix C.

In the case of Fig. 6, the source and receiver were at the same depth and H_r and H_e could be compared directly. However in the case of Fig. 20 the second term on the right side of Eq. 51 is 0.95 dB.

Figure 21 compares results where the mode theory losses have been corrected according to Eq. 51. With this correction there is essentially perfect agreement between ray and mode theory in the range interval from about 1942 to 1952 yd. At ranges greater than 1952 yd the ray theory begins to depart from the mode theory with the departure increasing as the ray-theory shadow zone is approached at a range of 2102 yd. The propagation loss of mode 1 merges with the mode theory at

TABLE I. Acoustic features for a source depth of 682.6 yd.

(1) Receiver depth (yd)	(2) Range of surface grazing ray (yd)	(3) Caustic range (yd)	(4) Range of mode 1 dominance (yd)	(5) $10 \log C_h/C_e$ (dB)	(6) Maximum mode number used	(7) Minimum range of accuracy (yd)
200	2104.11	None	2315	0.95	323	1940
400	2410.20	None	2627	0.50	471	2302
682.6	2730.30	2730.30	2951	0.00	990	2686
775	2819.35	2821.22	3041	-0.14	1321	2798
850	2888.11	2892.89	3111	-0.25	1677	2890

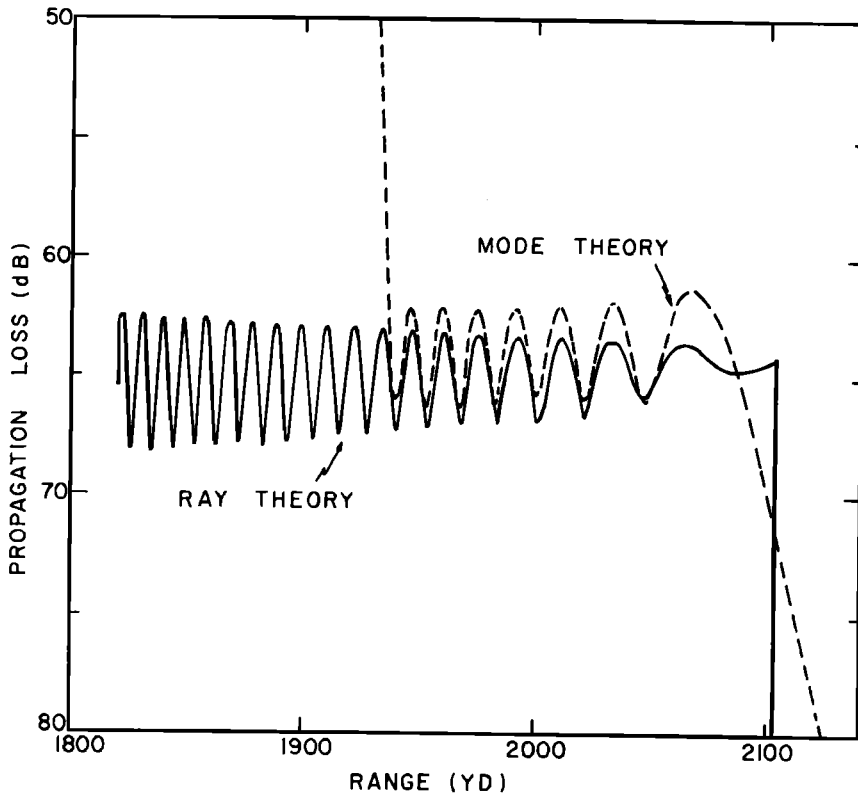


FIG. 20. Comparison of ray and mode theory for a 682.6-yd source and a 200-yd receiver. Mode theory has not been corrected for the index of refraction at the receiver.

a range of 2315 yd, not shown in Fig. 21. Beyond this range mode 1 represents the mode solution.

At this point it is convenient to present a number of receiver depths as a group. Figures 22-25 compare

ray and mode theory for the same source depth as that of Fig. 21, but for four other receiver depths. Salient features of the acoustic field for the receiver depths of Figs. 21-25 are presented in Table I. Column 1 is the

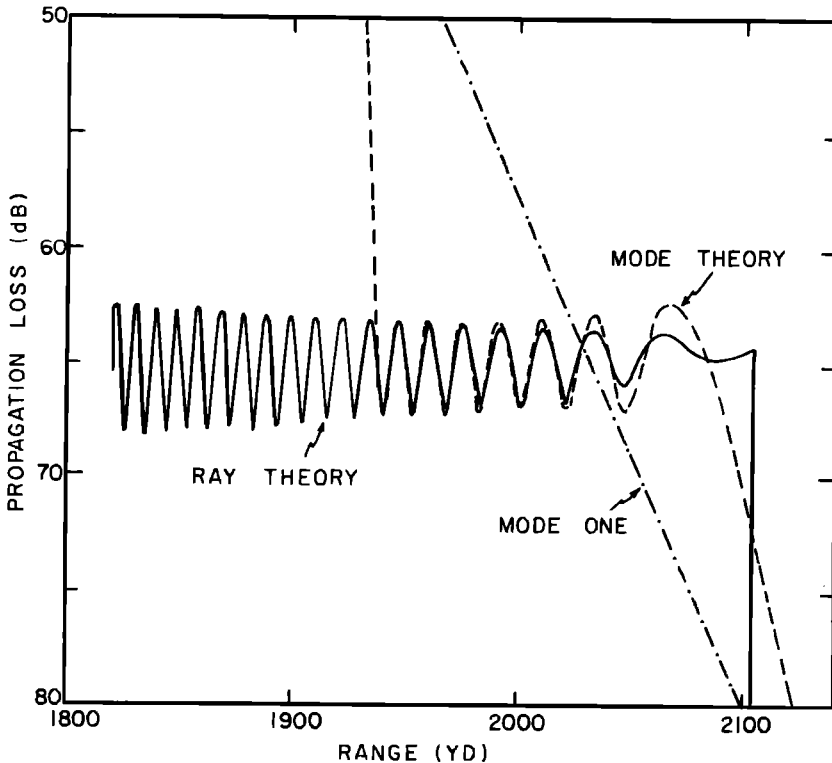


FIG. 21. Comparison similar to that of Fig. 20. The mode theory losses have been increased by 0.95 dB to correct for the index of refraction at the receiver.

FIG. 22. Comparison of ray and mode theory for a 682.6-yd source and a 400-yd receiver.

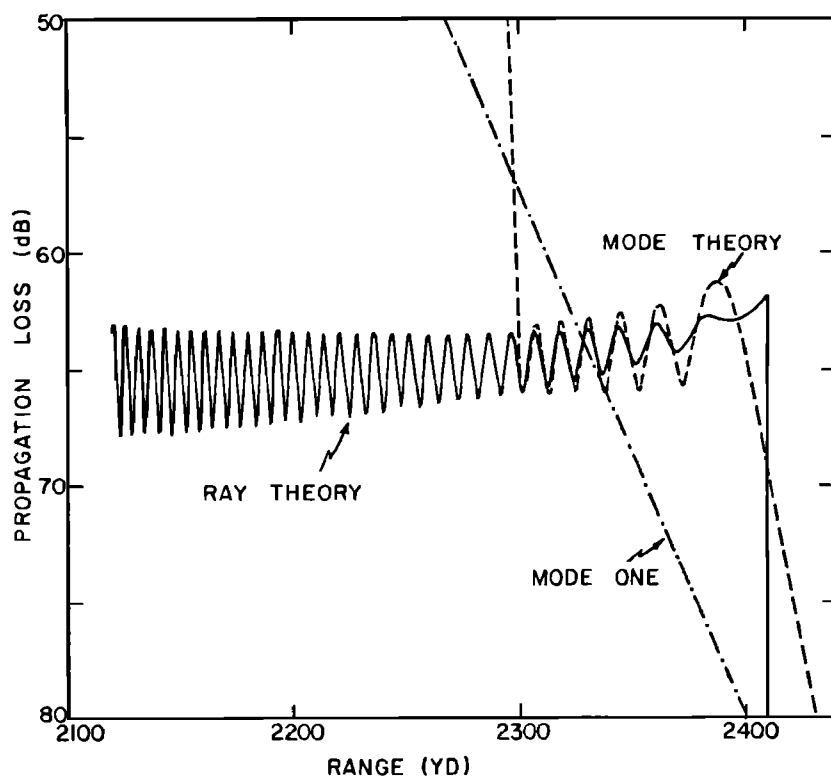
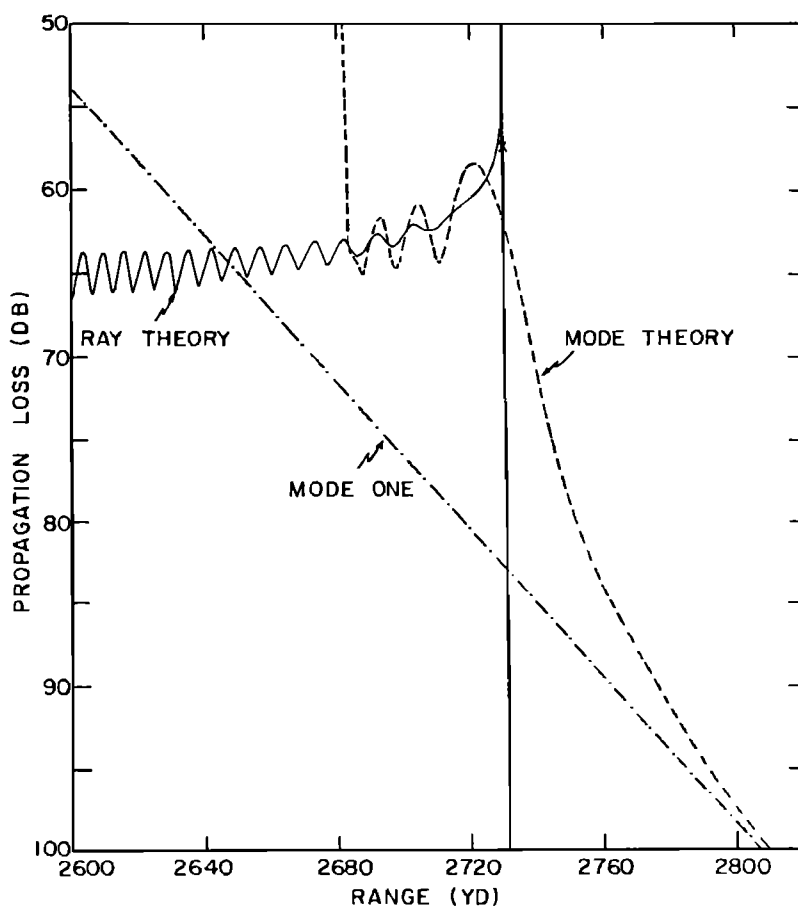


FIG. 23. Comparison of ray and mode theory for a 682.6-yd receiver. The X indicates the caustic value for extended ray theory.



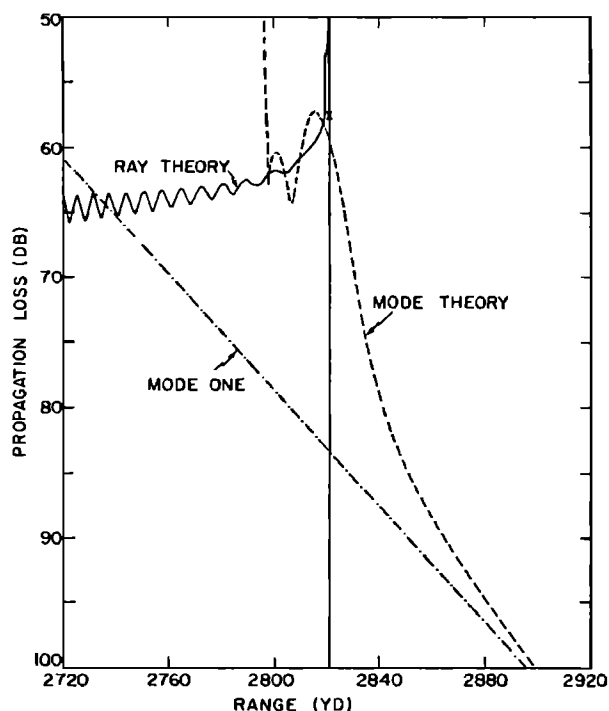


FIG. 24. Comparison of ray and mode theory for a 682.6-yd source and a 775-yd receiver. The X indicates the caustic value for extended ray theory.

receiver depth. Column 2 presents the range of the surface-grazing ray. Column 3 presents the caustic range. No caustic is present for the two shallowest receiver depths. For these receivers, the shadow-zone boundary is the range of column 2. The receiver depth of 682.6 yd (equal to the source depth) is the shallowest receiver for which there is a caustic. This caustic is formed by the surface-grazing ray. Thus the entries of columns 2 and 3 of Table I are identical in this case. For the two deepest receivers the shadow-zone boundary is the caustic range of column 3. Column 4 presents the range at which the propagation loss of mode 1 merges with the mode theory result. In all cases the range is off the scale of Figs. 21–25. Column 5 presents the index of refraction correction to the propagation losses of mode theory for proper comparison with ray theory. (We note in passing that the index of refraction correction of 0.3 dB was not applied to the mode theory result of Fig. 17. This was an additional complication which we did not wish to introduce into the discussion of Fig. 17. Moreover, since the ray and mode solutions did not overlap in Fig. 17, the correction appeared an unnecessary complication.)

Column 6 of Table I presents the maximum mode number used to make the calculations of Figs. 21–25. In prior investigations^{1,10} the computer was programmed to make calculations for some fixed number of modes. However, for the computations of Figs. 21–25 and Fig. 17 the computer was programmed to calculate a variable number of modes, depending on range.

A threshold was established such that modes with losses greater than this threshold could not possibly contribute to the result. The computer was programmed to treat only modes with losses smaller than this threshold. When all such modes had been summed, the propagation loss, range, and indicators giving the numbers of the modes summed were printed out. The computer would then repeat the process at the next smaller range. The initial range was chosen as the maximum range of interest and the computation progressed to smaller ranges in 2-yd range increments. The computation for a particular receiver was stopped when the propagation loss was less than 50 dB, which, for Figs. 21–25, represents a situation where the mode solution was diverging. The numbers given in column 6 of Table I represent the maximum mode number used which occurred at the smallest (last) range treated. This procedure, using a variable number of modes, saved considerable computer time because at the longest ranges of interest only a few modes were necessary as compared to hundreds of modes at short range.

Column 7 of Table I presents the shortest range point that was considered to be correct. For Figs. 23–25 this is only an estimate since the ray theory in the critical region differs from the correct mode theory and hence, cannot be used as a criterion for measuring the correctness of the mode theory. The mode theory diverges rapidly at ranges less than those of column 7. This divergence is not due to an inadequate number of modes as is the case for Refs. 1 and 10 or for Fig. 6. It

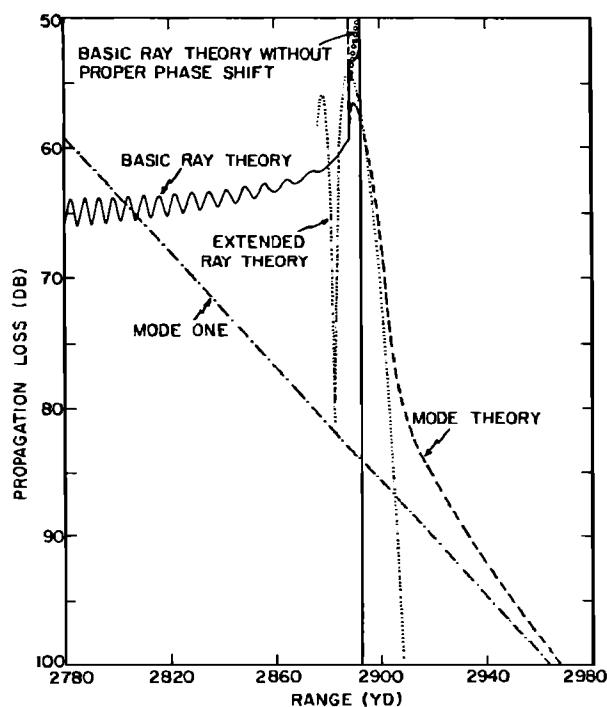


FIG. 25. Comparison of various ray theories and mode theory for a 682.6-yd source and an 850-yd receiver.

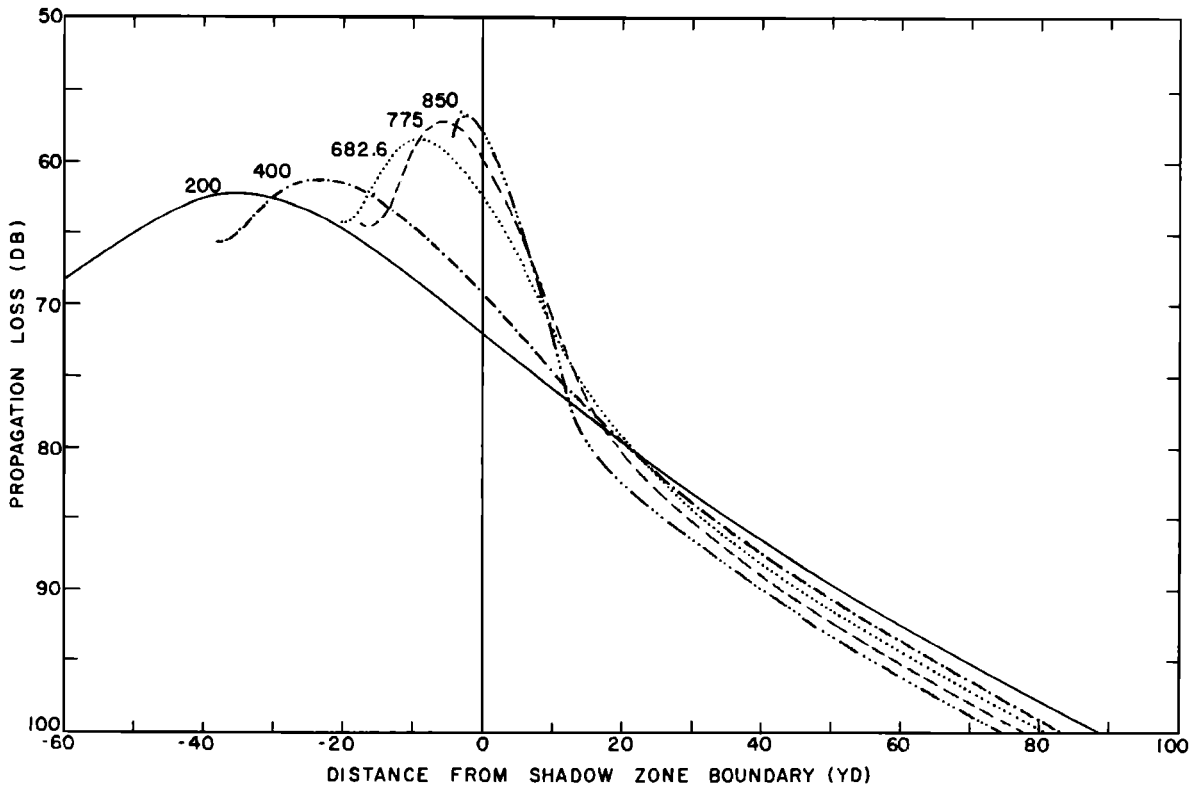


FIG. 26. Mode theory propagation loss near the shadow-zone boundary for a 682.6-yd source and for various receiver depths.

is due to roundoff error by the computer and will be discussed at the end of this section.

Two general trends are significant in Table I. First, the number of modes necessary in a computation increases with increasing receiver depth. Second, the difference between the range of the ray theory shadow zone (column 3 or 2) and the minimum range of accuracy (column 7) decreases with increasing receiver depth. This reflects the fact that greater computer accuracy is necessary for deeper receivers. Unfortunately, for a given computer accuracy the range interval over which ray and mode theory can be compared shrinks with increasing receiver depth. This is apparent in Figs. 22–25. In Fig. 22 there is a small interval at about 2300-yd range where the ray and mode theory solutions agree. In Figs. 23–25 there is no interval where ray and mode theory agree. However, we believe the mode theory to be accurate beyond the ranges of column 7 of Table I. Thus the differences between ray and mode theory in Figs. 23–25 result from an inadequacy of the ray theory. This disagreement between theories is to be expected since we observe in Figs. 6, 21, and 22 (where there are intervals of agreement) that the ray theory solution begins to depart further from mode theory as the shadow-zone boundary is approached.

In Figs. 23 and 24 only the caustic value for the extended ray theory is given (by the \times). In Fig. 25 a portion of the extended ray theory is given by the dotted

line. The extended ray theory should differ from mode theory since this ray theory does not take into account the ocean surface. For example, in Fig. 23, only one branch which forms the caustic is present, the other branch having been excluded by the surface. However, we note in Figs. 23–25, as the caustic develops more completely with increasing receiver depth, that agreement between the extended ray theory and mode theory improves at the caustic range. In Fig. 25 this agreement is within 0.9 dB. Note also in Fig. 25 that, as we proceed into the shadow zone from the caustic point, there is a similarity in the slopes of the propagation loss of the extended ray theory and mode theory. We had hoped to establish a more definitive comparison between these theories by extending the computations to still deeper receivers where the caustic would be more fully developed. It is apparent, however, that our present limitation of computer accuracy prohibits this extension.

The open-circle curve of Fig. 25 presents the ray theory without the $-\pi/2$ phase shift at the caustic. There is no obvious choice between this curve and the solid curve (ray theory with $-\pi/2$ phase shift) as far as comparison with the mode theory is concerned. We will presently introduce a more sensitive method for examining phase.

Figure 26 is a composite of the mode theory propagation losses of Figs. 21–25. The vertical scale of Fig. 26 is the same as that of Figs. 21–25. However, the horizontal scale has been normalized as the distance

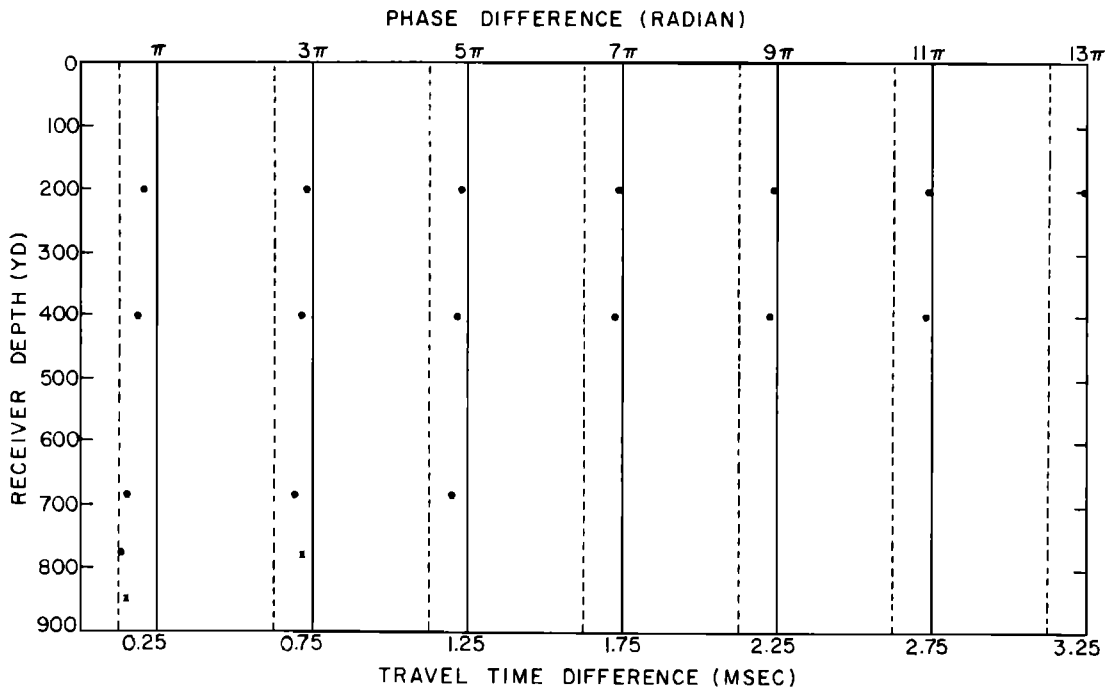


FIG. 27. Travel time differences between the ray paths at the ranges where minimum propagation losses occur in the mode theory results of Figs. 20-25.

from the shadow-zone boundary rather than the range. This presentation points up some interesting features. The mode theory losses appear to be smooth, continuous functions of receiver depth. Thus it appears that the last peak of the image interference pattern for a shallow receiver becomes the peak at $t \sim -1$ in Fig. 4 for a deep receiver with a well-developed caustic. This suggests that the entire image interference pattern for a shallow receiver transforms continuously into the interference pattern of Fig. 4 for a deep receiver when a caustic is formed.

In Fig. 26 the propagation loss at the shadow-zone boundary decreases with increasing receiver depth. This result agrees with the analysis of Eq. 44, which states that the propagation loss should decrease with increasing receiver depth as long as $C_A < 2^{\frac{1}{2}} C_s$.

We note in Fig. 26 that the peak of minimum loss approaches the shadow-zone boundary with increasing receiver depth. Also the propagation loss slope, as we proceed into the shadow zone from the boundary, steepens with increasing receiver depth. Both of these effects correspond to smaller $|L|$ in Eq. 30. This result does not agree with the analysis of Eq. 46 which states that with increasing receiver depth $|L|$ should decrease or increase, respectively, for receiver depths less than or greater than 682.6 yd. This disagreement is no doubt due to the presence of the ocean surface, which is ignored in the extended ray theory. It would be of interest to investigate deeper source and receiver depths to determine if mode theory supports the results of Eqs. 43-46 under conditions of well-developed caustics, removed from the influence of the ocean sur-

face. Unfortunately, such an investigation is impossible at present.

In Fig. 26 note the distinct change in slope for the 850-yd receiver at a distance of about 13 yd. A similar, but not so pronounced, change occurs for the 775- and 682.6-yd receivers. This can be explained if we consider the acoustic field in the shadow zone to be the superposition of two effects. At ranges close to the caustic (steep slope region) the field is primarily due to diffraction from the caustic. At ranges far from the caustic (small slope region) the field is primarily due to diffraction from the ocean surface.

Note that at ranges far from the shadow-zone boundary, the loss curves all have the same slope but the loss increases with increasing receiver depth. This is somewhat surprising since, at the shadow-zone boundary the loss decreases with increasing receiver depth. The loss curves then do not maintain their relative order but cross each other. When the field is dominated by refraction from the surface, one might expect the propagation loss to increase as the receiver is removed from the surface to greater depth.

Returning now to Figs. 21-24 we note that the interference pattern of ray theory always appears to be shifted slightly to the left of that of mode theory with the shift increasing as the shadow-zone boundary is approached. This observation suggests consistent phase errors in the ray theory. An approach, independent of the amplitudes of ray theory, was developed to investigate the phase of ray theory. This approach is based on the following assumptions: (1) The mode theory is correct and may be used as a control. (2) The minima

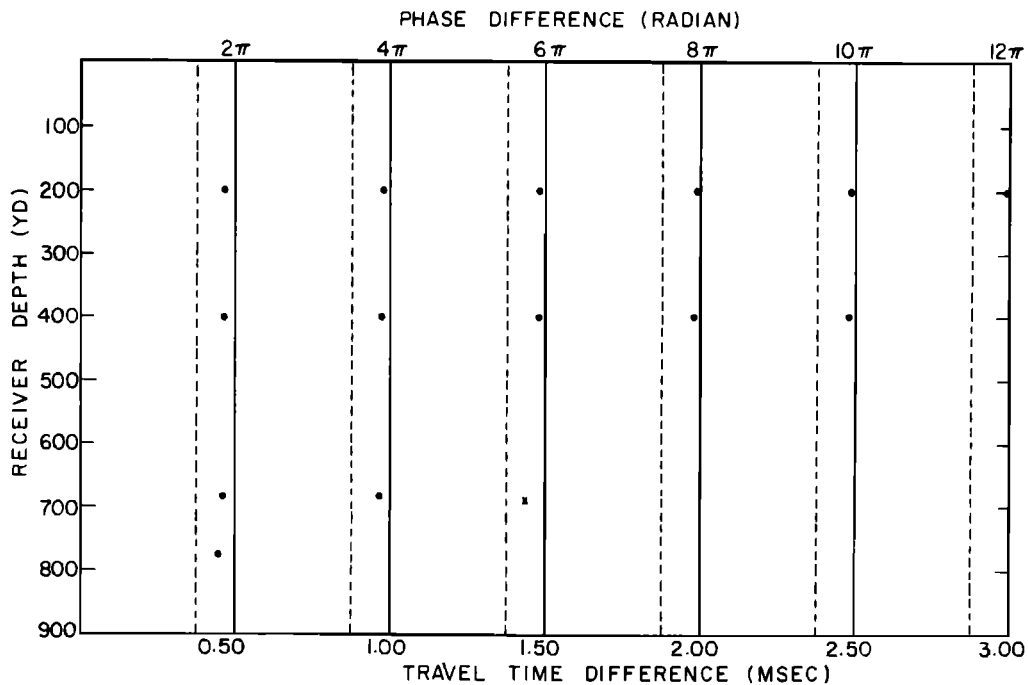


FIG. 28. Travel time differences between the ray paths at the ranges where maximum propagation losses occur in the mode theory results of Figs. 20-25.

and maxima in propagation loss image interference patterns occur at ranges where the two ray arrivals are exactly in phase or π radians out of phase. (This is an approximation which is valid provided the amplitudes of ray theory are slowly varying with range.) (3) Ray theory travel times are correct. (Ray theory amplitudes and phase shifts may be in error.)

The first step of the approach was the determination of the ranges in Figs. 20-25 where relative minima occurred in the propagation losses of mode theory. Ray theory computations of travel time were examined and the travel time differences between the two ray paths at each of the ranges from the first step were determined. These travel time differences are plotted in Fig. 27. A phase difference scale is also given at the top of Fig. 27. It was obtained from $\Delta\psi = 2\pi/\Delta T$, where $\Delta\psi$ is the phase difference and ΔT is the travel time difference. The set of points to the left of 0.25 msec corresponds to the relative minima at longest range while the sets at progressively greater travel time differences correspond to relative minima at progressively shorter ranges. The two \times 's indicate points which are of questionable accuracy since they correspond to ranges that are close to the divergence of the mode theory calculations due to roundoff errors.

Examination of Figs. 20-25 indicates that only one point in Fig. 27 corresponds to a case where one of the ray paths has touched a caustic rather than being reflected from the ocean surface. This point is the \times in the lower left extreme of Fig. 27. Thus, if the ray theory of Sec. I-C were correct this single point should lie on the dashed line at $\pi/2$ rad while all other points

should lie on the solid lines which are at odd multiples of π rad. These positions would correspond to exact in-phase relationships between rays assuming a phase shift of $-\pi/2$ on touching a caustic and a phase shift of $-\pi$ on reflection from the surface.

It is evident that there is not a discontinuous jump in phase from $-\pi$ to $-\pi/2$ as we go from the surface-reflected to caustic-touching condition. Figure 27 indicates that there is a smooth transition in phase shift from $-\pi$ for receivers near the surface to $-\pi/2$ for receivers at depths where the caustics are formed.

Figure 28 is the counterpart of Fig. 27 but for relative maxima in propagation loss rather than relative minima. In this case the solid lines are at even multiples of π rad corresponding to exact out-of-phase relationships. None of the points in Fig. 28 correspond to a case where a ray has touched a caustic. The results of Fig. 28 are similar to those of Fig. 27, showing a smooth transition in phase shift tending from $-\pi$ for shallow receivers to $-\pi/2$ for deep receivers.

Although we have indicated that one should introduce a $-\pi/2$ phase jump when the ray touches the caustic, it is evident from Figs. 27 and 28 that this is only a first order approximation. The results of mode theory indicate a continuous transition in phase rather than a discontinuous phase jump. Thus an improved ray theory should provide for a continuous transition in phase by sensing the presence of the caustic before actual contact.

A complication in the interpretation of Figs. 27 and 28 is the presence of the ocean surface. In an unpublished

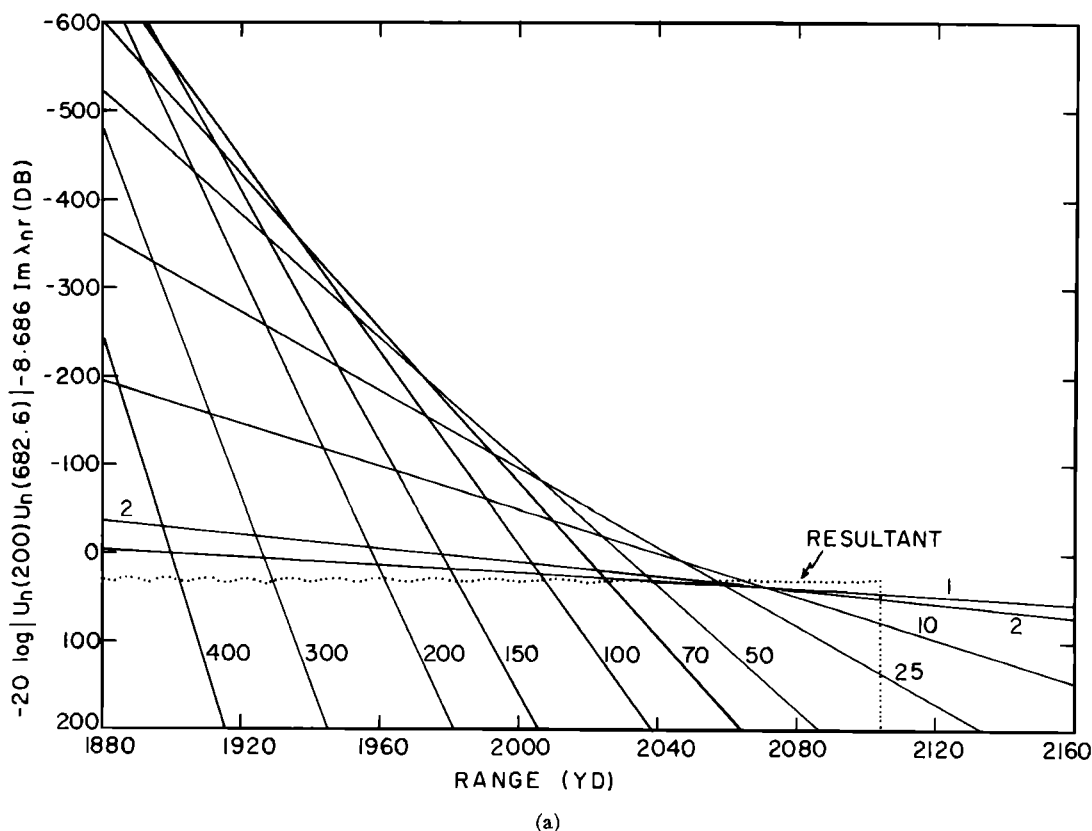


FIG. 29. Relative contribution of individual modes as a function of range for a 682.6-yd source and various receiver depths: (a) 200-yd receiver.

investigation we have examined the phase shift associated with the ocean surface. We examined the phase velocity of a particular mode as a function of frequency in a situation where the higher frequencies corresponded to rays which did not reflect from the ocean surface while lower frequencies corresponded to rays which reflected from the surface. These phase velocities were compared with those obtained from ray theory and the phase integral method.¹⁸ There was good agreement between the phase velocities obtained by the two methods with the use of a $-\pi$ shift in the ray theory at phase velocities well above the surface velocity and a $-\pi/2$ shift in the ray theory at phase velocities well below the surface velocity. There was a discontinuity in the result of the phase integral method at a phase velocity equal to the surface velocity corresponding to a jump in phase at the onset of reflection from the surface. In contrast the phase velocity as determined by mode theory went through a smooth, continuous transition in the region. It was evident that in an improved ray theory, a ray vertexing just below the surface should sense the proximity of the surface such that the phase does not jump but changes in a continuous fashion.

Because of the complication of both surface and caustic effects, we cannot give an interpretation of how ray theory might achieve the smooth transition from

$-\pi$ to $-\pi/2$ in Figs. 27 and 28. We shall have to assess these two effects separately. This will require an investigation of caustics where no surface is involved and a further investigation of surface effects such as described in the preceding paragraph. Once we have established interpretations for the separate effects of surface and caustic on ray theory phase, we may be able to apply them to the composite case illustrated by Figs. 27 and 28.

Consider now the relative contribution of individual modes for the source depth of 682.6 yd. These are presented in Figs. 29(a)–(e) and correspond to the propagation loss plots of Figs. 21 to 26. Before discussing the structure of the patterns consider the round-off problem discussed earlier. At the minimum ranges of accuracy (column 7 of Table I) the maximum mode contributions were determined to lie in the interval 352–378 dB above the resultant for the five receiver depths of Figs. 29(a)–(e). The average value was about 364 dB. This average corresponds to an accuracy of about 20 decimal digits in the contribution of the mode of maximum contribution. This corresponds favorably with a minimum of 19 decimal digits of accuracy cited earlier for the eigenvalues. This analysis of roundoff cannot be too precise because the roundoff depends somewhat on the maximum size of the partial sums in the mode summing process. Nonetheless the analysis is

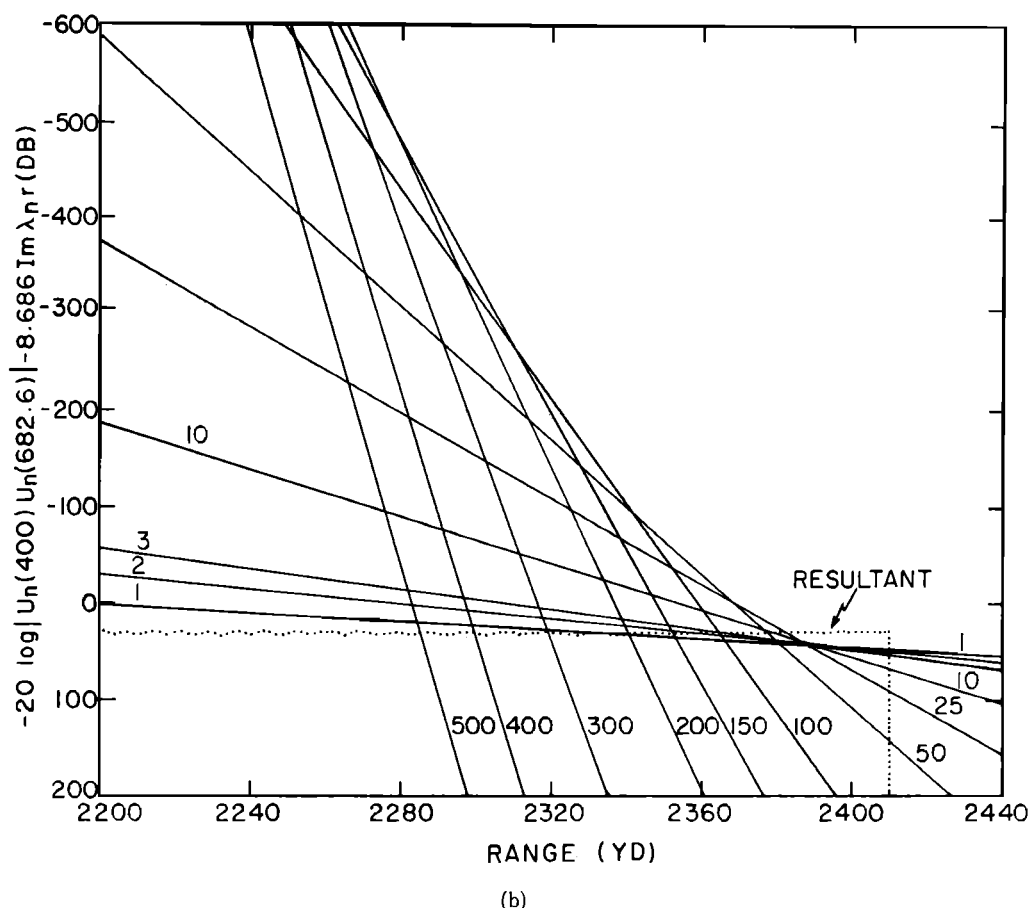


FIG. 29 (Continued). (b) 400-yd receiver.

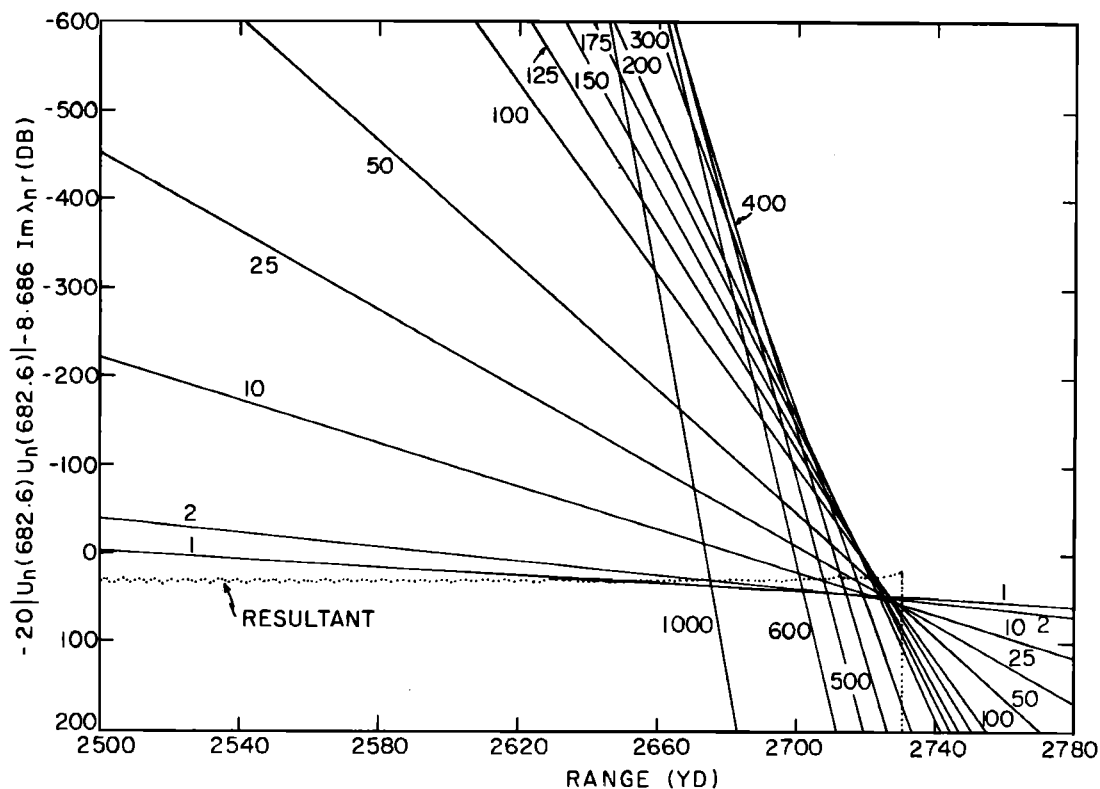
adequate to establish that the divergence of the mode theory computations at minimum range in Figs. 21 to 26 is due to computer roundoff error.

Consider now the general pattern of Figs. 29(a)–(e). The behavior in Fig. 29(a) is similar to that of Fig. 12. In Fig. 12, which presents sufficient detail, we see that the intersections of the lines representing adjacent modes moves inward with increasing mode number. Although the eigenvalues represent a discrete set of numbers we may, in effect regard, $|Mx_n|$ as a continuous variable. We consider the mode curves, such as those of Fig. 12, to be a one-parameter family of curves, where the parameter is $|Mx_n|$. The significant feature of Figs. 12 and 29(a) is the formation of a simple envelope. This envelope starts at the intersection of modes 1 and 2 and curves upward to smaller range as the mode number ($|Mx_n|$) is increased. In this case the envelope is a relative maximum in the mode contribution. This mode contribution pattern for near-surface transducers is the same as that described by Pekeris² on p. 301. For the case of a medium of constant velocity gradient Pekeris states, “As for the convergence of the terms for a point inside the normal zone, one can show that the absolute value of the terms first increases with the order of the mode, reaching a maximum, and then decreasing again. The number of

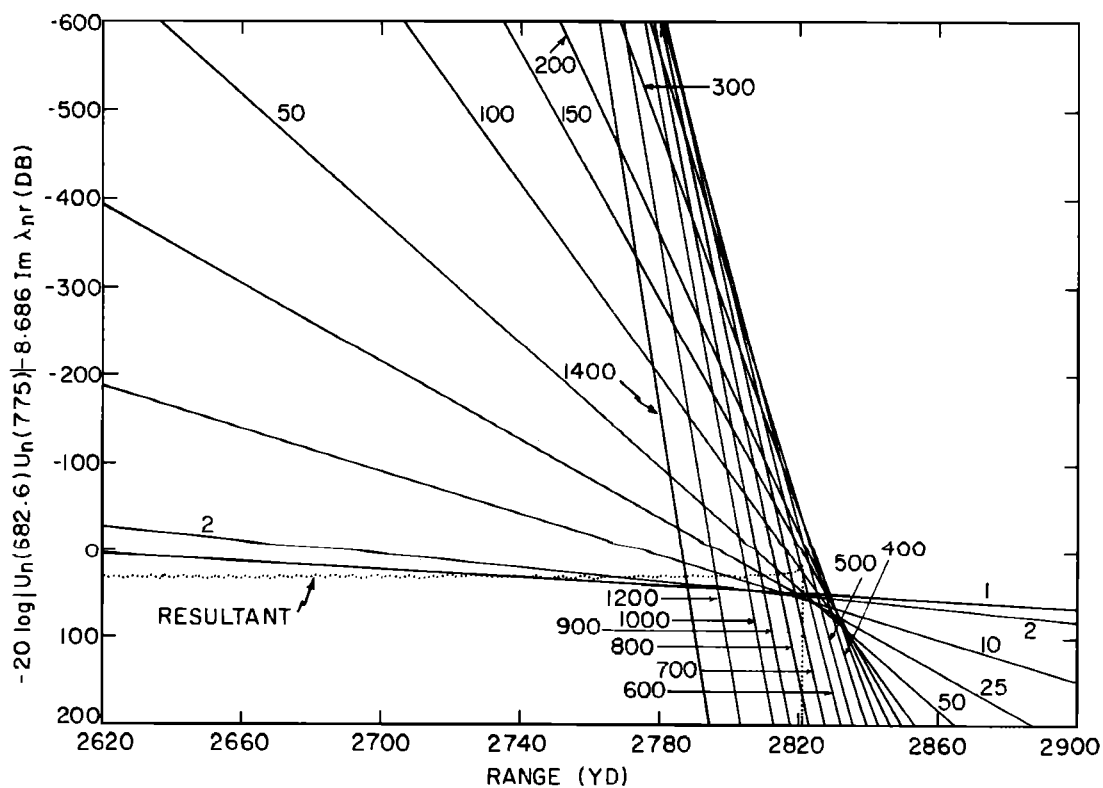
required terms increases as one recedes into the normal zone.”

In contrast to a simple envelope, the envelope of Figs. 15, 29(d), and 29(e) consists of two sections. The first section, starting with the intersection of modes 1 and 2, curves downward to larger range as the mode number is increased. For this section the envelope is a relative minimum in the mode contribution. The second section of the envelope starts at some maximum range and curves upward to smaller range as the mode number is increased. For this section the envelope is a relative maximum in the mode contribution. The two sections of the envelope form a cusp at some maximum range, which may be regarded as the end of the first section and the beginning of the second section. There is no envelope beyond this maximum range.

The cusp in the envelope is well developed in Figs. 15, 29(d), and 29(e). The cusp is evident but not prominent in Fig. 29(c). Though not evident in Fig. 29(b), there is the vestige of a cusp. This cusp has disappeared completely in Fig. 29(a). (These features are discussed in more detail in Sec. III.) There is no ray theory caustic for receiver depths shallower than that of Fig. 29(c). Thus the appearance of a well-developed cusp in the envelope of the family of mode contribution curves is correlated with the appearance of the caustic of



(c)



(d)

FIG. 29 (Continued). (c) 682.6-yd receiver; (d) 775-yd receiver.

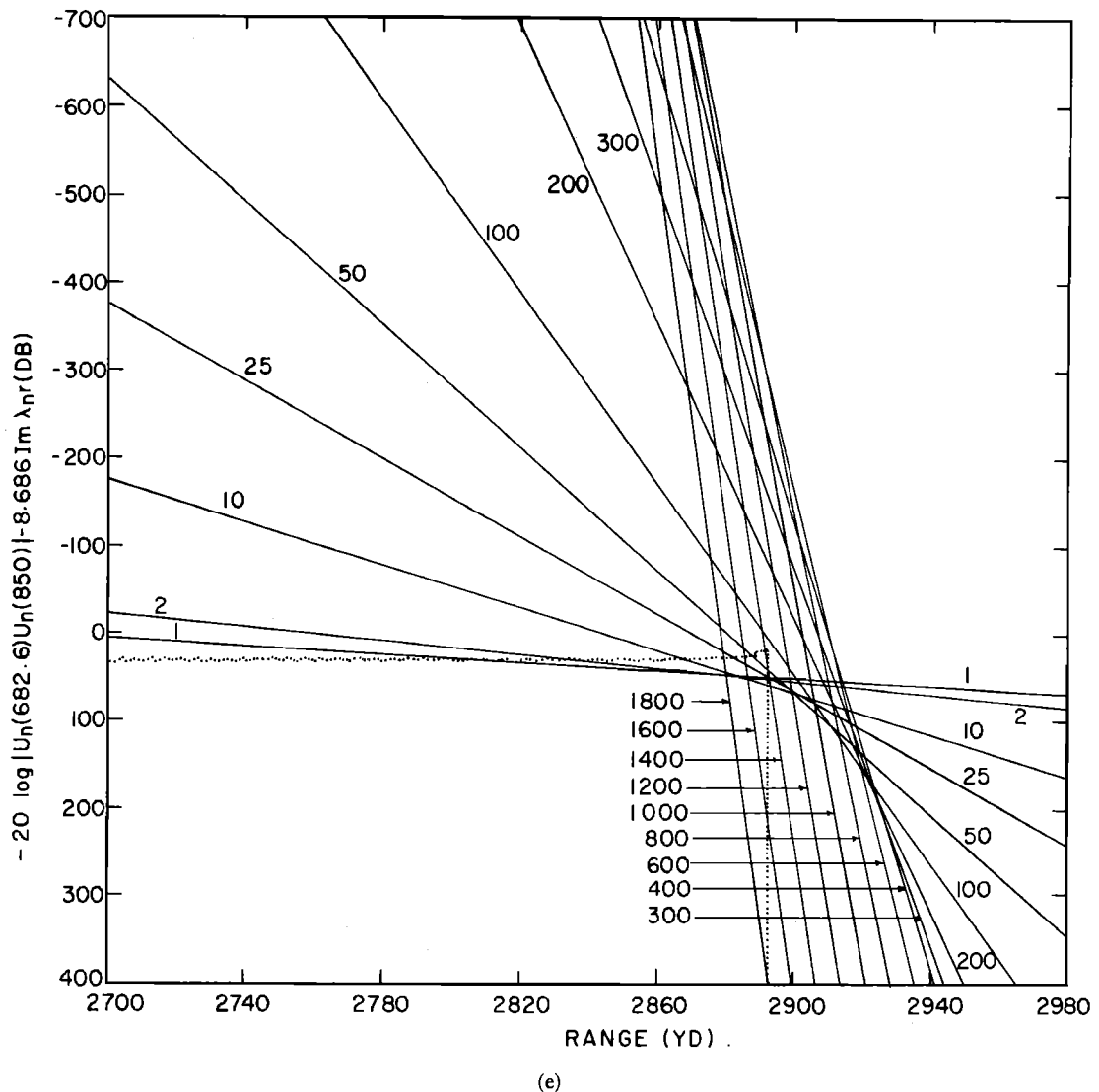


FIG. 29 (Continued). (e) 850-yd receiver.

ray theory. This will be established analytically in Sec. III.

We can now provide a possible explanation for the function of this cusp as related to the ray theory caustic. In the discussion of the 775- and 850-yd receivers of Fig. 26 we noted a distinct change in slope of the mode theory propagation loss about 13 yd beyond the ray theory caustic. We observe in Figs. 29(d) and 29(e) the presence of the cusp about 20 yd beyond the ray theory caustic. We believe that the change in slope of the mode theory propagation loss results from the rapid onset of those modes associated with the second section of the envelope in Figs. 24(d) and 24(e). The contribution of these modes increases very rapidly with decreasing range. They begin to make a significant contribution at a range between that of the cusp, and the ray theory caustic.

In Fig. 15 the cusp appears far beyond the caustic at a range of about 3300 yd. From Fig. 17 we see that

this is far beyond the region where the propagation loss is associated with diffraction from the caustic. For some inexplicable reason the cusp appears at too long a range for rapid buildup of mode amplitudes to be associated with the caustic. This apparent discrepancy is taken care of by the mode annihilation illustrated in Figs. 19(a)-(c). By this mechanism a rapid buildup of mode amplitudes need not necessarily be associated with a rapid decrease in propagation loss.

III. ANALYSIS OF THE CONTRIBUTION OF INDIVIDUAL MODES

This section is an analysis of the contribution of individual modes, $|A_n|$, given by

$$|A_n| = |H_0^2(\lambda_n r) U_n(Z) U_n(Z_0)|. \quad (52)$$

The purpose of this section is to examine the convergence properties of the normal mode series. This

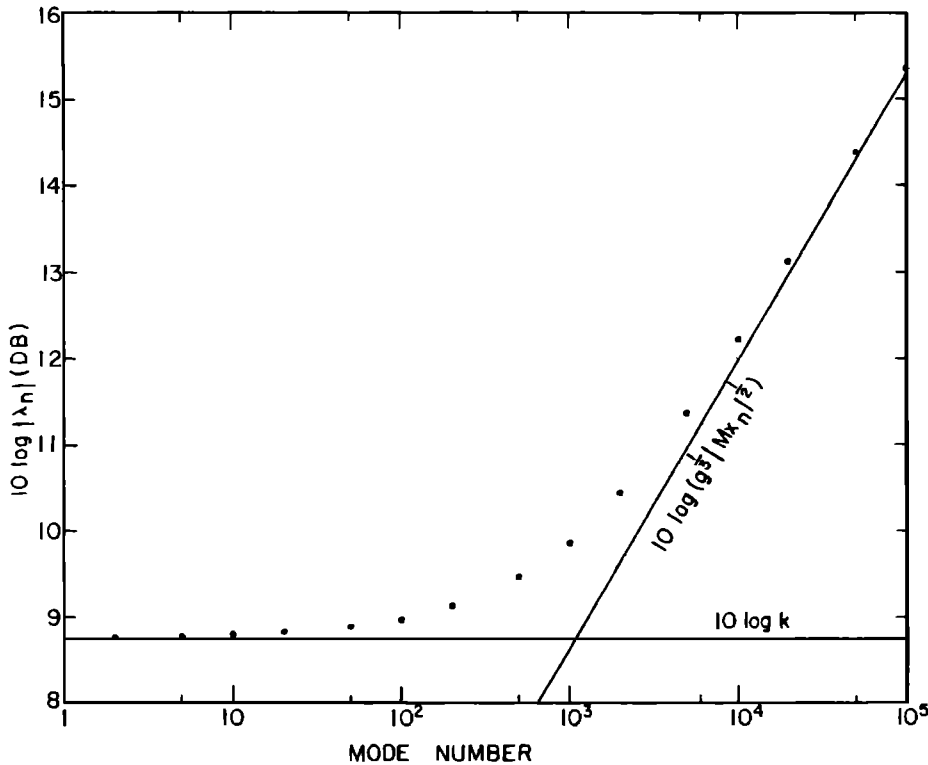


FIG. 30. $10 \log$ of the absolute value of the wave-number versus mode number. The two lines represent approximation valid for small and large mode numbers.

includes not only an analysis of the conditions for which the series converges but also of the rapidity of convergence.

For the model of this article (or closely related models), Pekeris,² Marsh,¹¹ and Morse³ discuss the convergence properties in terms of r_0 , the range of the surface-grazing ray. For $r < r_0$, Morse³ states that the series is not convergent while Pekeris² states that the series converges slowly. All three investigators^{2,3,11} agree that for $r > r_0$ the series is rapidly convergent. Our numerical examples do not agree with these conclusions. Figure 6 demonstrates that the mode series converges for at least some ranges which are less than r_0 . Moreover, Fig. 12 indicates that the convergence may even be rapid for r smaller but close to r_0 . Figure 18 demonstrates that the mode series is not always rapidly convergent for $r > r_0$. It is evident that the problem of convergence must be carefully examined.

We shall demonstrate that the conditions for which the mode series converges is completely independent of r_0 . Although the rapidity with which the series converges does indeed depend upon r_0 , we shall demonstrate that it also depends on the absence or presence of the ray theory caustic.

The analysis of Eq. 52 will be in terms of a series expansion, which takes different form for modes of large and small order. The detailed development of these expansions is contained in Appendix D.

A. Analysis of Large-Order Modes

In the analysis of large-order modes we first note that Eq. 39 of Ref. 1 was developed for low-order modes. This equation was based on the approximation

$$10 \log |\lambda_n| \sim 10 \log k, \quad (53)$$

which does not apply to large-order modes. This is illustrated in Fig. 30 which presents $10 \log |\lambda_n|$ as a function of mode number. The horizontal line represents the approximation of Eq. 53. The slant line represents an approximation for large-order modes. It may be obtained from Eq. D16.

A representation of the relative contribution of individual modes, which applies to large- as well as small-order modes is

$$H_n - 10 \log r = -20 \log |U_n(Z) U_n(Z_0)| + 10 \log |\lambda_n| - 8.686 \operatorname{Im} \lambda_n r - 7.98. \quad (54)$$

The constant in Eq. 54 is $-10 \log(2\pi)$. In future work we recommend that Eq. 54 be used rather than Eq. 39 of Ref. 1 for two reasons: (1) Equation 54 is more accurate, and (2) Eq. 54 represents the anomaly from cylindrical spreading, much as $H - 20 \log r$ represents the anomaly from spherical spreading.

In order to compare Eq. 54 with Eq. 39 of Ref. 1 we present Figs. 31 and 32. Figures 31 and 32 are the Eq. 54 counterparts of Figs. 12 and 15, which are based on

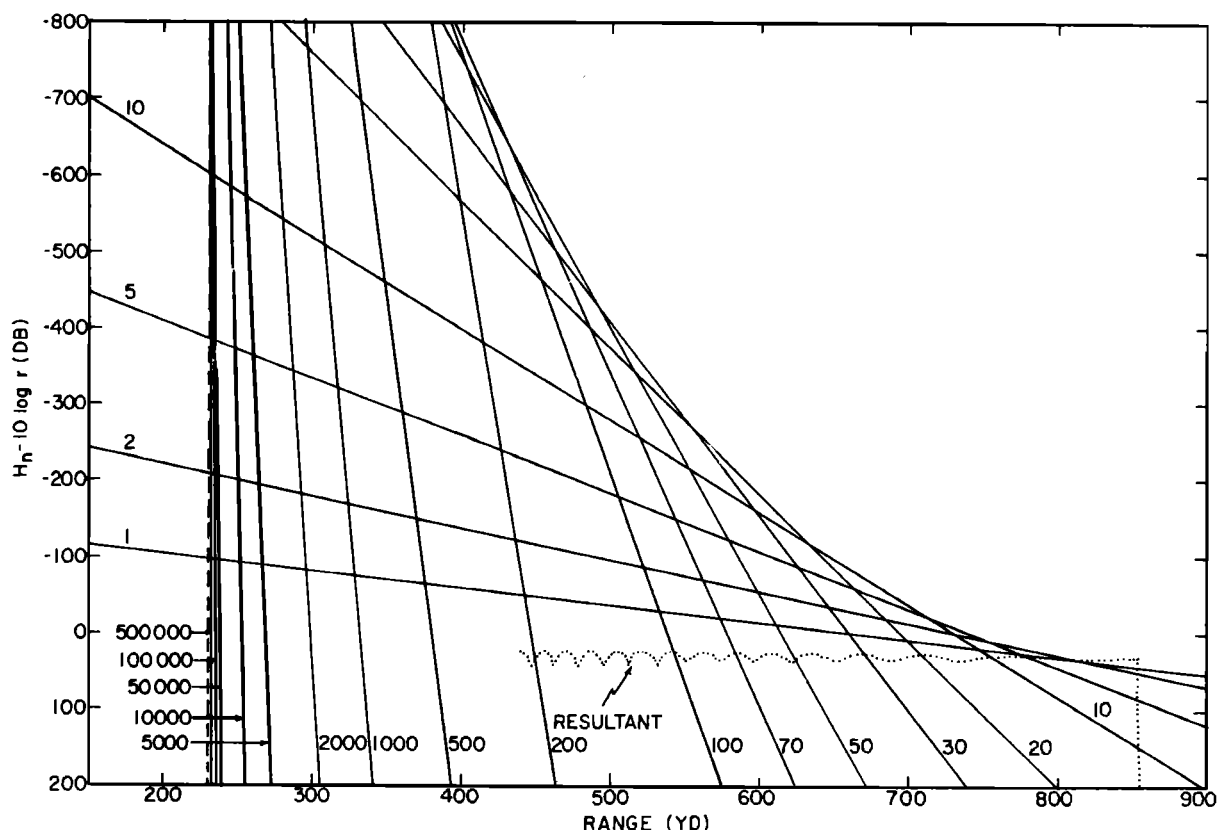


FIG. 31. Relative contribution of individual modes as a function of range for a 66.7-yd source and a 66.7-yd receiver. Mode values are determined from Eq. 54. The mode series diverges at ranges to the left of the dashed vertical line.

Eq. 39 of Ref. 1. In the case of the parameters of this study there is little difference between Eq. 39 of Ref. 1 and Eq. 54 for small-order modes. The term $10 \log(C_0/f)$ represents a shift of only -0.76 dB, while from Fig. 30 we see that the error resulting from the use of Eq. 53 is less than 1 dB for mode numbers less than 800. In the case of large-order modes, the error resulting from Eq. 53 is as much as 6.6 dB for mode 100 000, but even this value is small considering the vertical scale of Fig. 15 and similar figures. Thus Figs. 12, 15, and 29(a)-(e) are adequate presentations for small-order modes. Figures 31 and 32 are included here primarily for the investigation of large-order modes.

We now proceed with the analysis of $|A_n|$ of Eq. 52, which is related to H_n of Eq. 54 or of Eq. 39 of Ref. 1 by

$$H_n = -20 \log |A_n| - 20 \log \pi. \quad (55)$$

This conversion of $|A_n|$ to levels in decibels in the various illustrations representing the contribution of individual modes is a pictorial convenience. These illustrations can readily be related to our analysis of $|A_n|$.

In the case of large-order modes Sec. VIII of Appendix D develops the expression,

$$|A_n| = 4^{-1} (2/\pi r)^{1/6} |M x_n|^{-5/4} E_n, \quad (56)$$

where

$$E_n = \exp(2^{-1} g^1 \sum_m \alpha_m |M x_n|^{1-m}). \quad (57)$$

The first two coefficients in Eq. 57 are

$$\alpha_1 = 3^{1/2} (Z + Z_0) - r \quad (58)$$

and

$$\alpha_2 = 2^{-1} [(k/g^1)^2 r - 3^{1/2} 2^{-1} g^1 (Z^2 + Z_0^2)]. \quad (59)$$

Consider now the convergence of the normal-mode series. One can readily demonstrate from Eq. 56 that $\lim_{|M x_n| \rightarrow \infty} |A_n|$ is zero for $\alpha_1 < 0$ and is infinite for $\alpha_1 > 0$. It follows immediately that the normal-mode series diverges when $\alpha_1 > 0$ or when

$$r < 3^{1/2} (Z + Z_0). \quad (60)$$

The convergence tests when $\alpha_1 \leq 0$ are complicated and are discussed in Sec. IX of Appendix D, which demonstrates that the mode series is absolutely convergent when

$$r > 3^{1/2} (Z + Z_0). \quad (61)$$

The dashed vertical lines in Figs. 31 and 32 are

$$r = 3^{1/2} (Z + Z_0). \quad (62)$$

It is clear that the lines representing the mode contri-

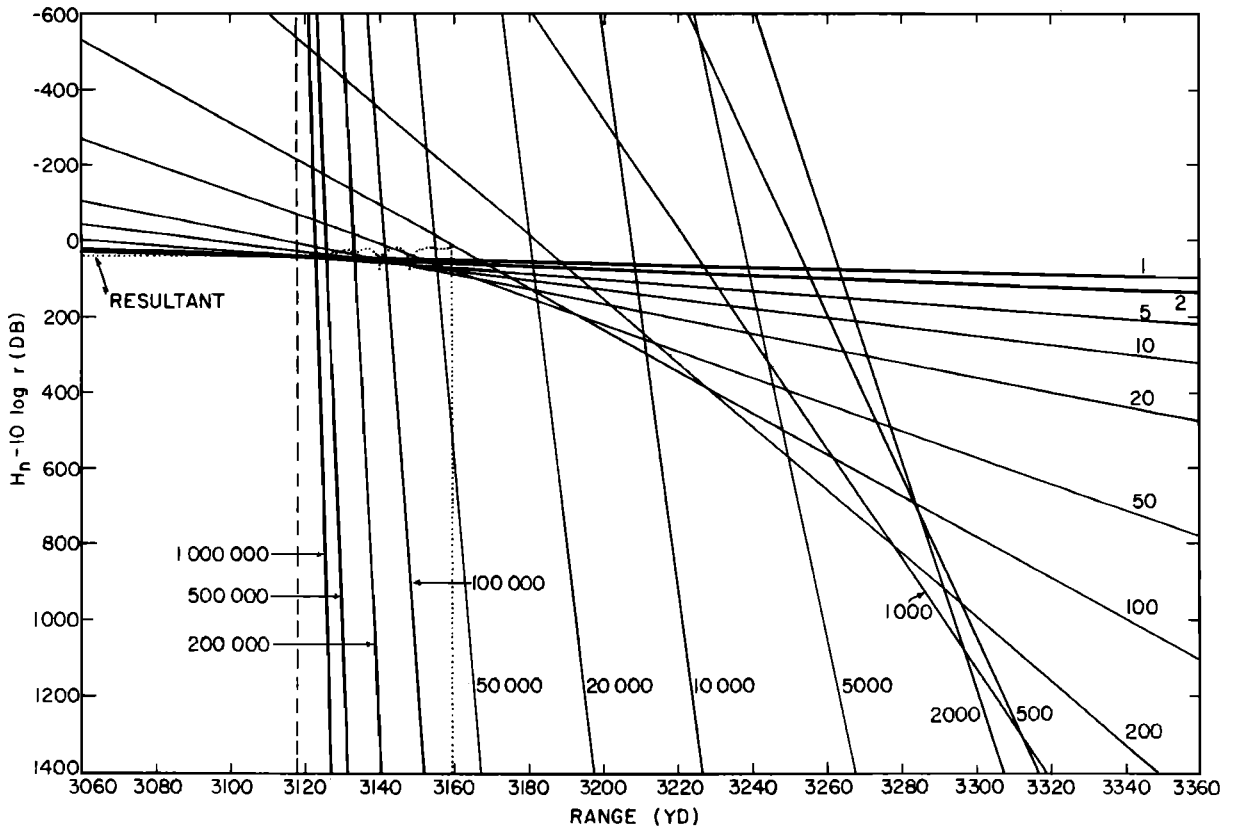


FIG. 32. Counterpart of Fig. 31 but for a 1000-yd source and an 800-yd receiver.

butions approach this dashed line as a limit as the mode number is increased. These numerical results agree with the theoretical results of Eqs. 60 and 61.

Figure 15 of Ref. 1 indicates that there may be a minimum range of convergence for each of the two families of modes in a surface duct. We plan to investigate this more complicated situation and determine the convergence conditions using the approaches of Appendix D.

We note that the convergence of the mode series is independent of the shadow-zone boundary. Indeed under conditions of very deep sources or receivers the mode series may even diverge in the shadow zone. We shall now investigate these conditions for some simple source and receiver depth configurations.

From Sec. VII of Appendix D we may express the range of the surface-grazing ray as

$$r_0 = 2S^{\frac{1}{2}}(Z^{\frac{1}{2}} + Z_0^{\frac{1}{2}}), \quad (63)$$

where

$$S = b^{-1}C_0^{-2} = -C_0/2\gamma = k^2g^{-1}. \quad (64)$$

The quantity S represents a fundamental depth which appears in several important contexts in both the ray and mode analysis. For the profile parameters of this study $S = 682.5768$ yd. If we set $Z = Z_0$, equate Eq. 63 to Eq. 62 and solve for Z_0 , we obtain

$$Z_0 = 4S/3. \quad (65)$$

This depth represents the coincidence of the minimum range of convergence and r_0 , when the source and receiver depth are equal. We may conclude that when Z_0 and Z are both $< 4S/3$ the series converges at r_0 . When Z_0 and Z are both $> 4S/3$ the series diverges at r_0 .

A similar analysis can be applied to R_c , the range of the caustic. When it exists, R_c is the shadow-zone boundary rather than r_0 . The existence of the caustic can be related to S by expressing Eq. 49 in terms of depth. At the onset of the ray theory caustic

$$ZZ_0 = S^2. \quad (66)$$

Thus, if

$$ZZ_0 < S^2, \quad (67)$$

no caustic is formed. While if

$$ZZ_0 > S^2, \quad (68)$$

a caustic is formed.

Equation 21 may be expressed as

$$R_c = 2[(S+Z)(S+Z_0)]^{\frac{1}{2}}. \quad (69)$$

If we set $Z = Z_0$, equate Eq. 69 to Eq. 62, and solve for Z_0 , we obtain

$$Z_0 = S/(3^{\frac{1}{2}} - 1) \approx 1.366S. \quad (70)$$

This depth represents the coincidence of the minimum range of convergence and the caustic, when the source and receiver depth are equal. We may conclude that

when Z_0 and Z are both $< 1.366S$ then the series converges at the caustic range. When Z_0 and Z are both $> 1.366S$ then the series diverges at the caustic range.

Another case of interest is the onset of the caustic, where Eq. 66 holds. Here Eq. 63 and 69 both reduce to

$$r_0 = R_c = 2S^{1/2}(S + Z_0)Z_0^{-1/2}. \quad (71)$$

If we set $Z = S^2/Z_0$, equate Eq. 71 to Eq. 62, and let $Z_0 = y^2S$, we obtain the equation

$$3^{1/2}y^4 - 2y^3 - 2y + 3^{1/2} = 0. \quad (72)$$

Two of the roots of Eq. 72 are complex and are of no further interest. The smaller real root is

$$y_1 = [1 + 7^{1/2} - (2 \cdot 7^{1/2} - 4)^{1/2}] / 2 \cdot 3^{1/2} \approx 0.72437. \quad (73)$$

The larger real root is the reciprocal of y_1 . The solutions in terms of Z_0 are then

$$Z_0 \approx 0.5247S \quad \text{and} \quad Z_0 \approx 1.9058S. \quad (74)$$

These two roots represent the two source depths for which the minimum range of convergence coincides with the onset of the caustic. We note that if one root in Eq. 74 is the source depth, the other root represents the receiver depth since the product of the two roots is S^2 . This result is to be expected since the source and receiver depths are in a reciprocity relationship. We may conclude that when the source (receiver) depth lies between $0.5247S$ and $1.9059S$, the series converges at the onset of the caustic. If the source (receiver) depth lies outside these limits the series diverges at the onset of the caustic and hence at the caustic for all greater receiver (source) depths.

Let us now consider the results of these simple cases from the standpoint of the numerical examples of this study. In all these examples the series converges at r_0 and R_c . In the case of Fig. 31, $Z = Z_0 = 0.098S$, which is much less than Eqs. 65 and 70 implying convergence. In the case of Figs. 29(a)-(e), $Z_0 = S$ while $Z \leq 1.245S$, which are less than Eqs. 65 and 70 implying convergence. In the case of Fig. 32, the deeper element is $Z_0 = 1.465S$. This does not fall under the simple cases analyzed here.

Figure 29(c) represents the very special case of $Z = Z_0 = S$, which is the onset of the caustic with source and receiver at the same depth. The series always converges at the onset of the caustic for this special case as can be seen from Eq. 74. Here $0.5247S < S < 1.9059S$ implying convergence. Indeed if we maximize $R_c - 3^{1/2}(Z + Z_0)$ with respect to Z_0 for the case of $Z = S^2/Z_0$, we obtain a maximum at $Z_0 = S$. In this case

$$R_c = 4S = 4Z_0 = 4Z, \quad (75)$$

$$3^{1/2}(Z + Z_0) = 3^{1/2}2S, \quad (76)$$

and the maximum difference is $0.536S$. This is the reason why we chose $Z_0 = S$ in Sec. II-C. We hoped that by maximizing the difference between the onset of the caustic and the range of minimum convergence we

could avoid the problems encountered in Fig. 17. Unfortunately we had not reckoned with the computer roundoff problem in a region of slow convergence for low-order modes which is the topic of the next section.

B. Analysis of Small-Order Modes

In the case of small-order modes Sec. VII of Appendix D develops the expression

$$|A_n| = 2^{7/6} 3^{1/2} \pi^{-1/2} g^{1/6} k^{-1/2} (ZZ_0)^{-1/2} |h'_2(Mx_n)|^{-2} E_n, \quad (77)$$

where

$$E_n = \exp(\beta_1 \sum_m \alpha_m |Mx_n|^m). \quad (78)$$

Here

$$\beta_1 = -3^{1/2} 4^{-1} g^{1/6} k^{-1/2}, \quad (79)$$

while the first three coefficients in the series are

$$\alpha_1 = r - r_0, \quad (80)$$

$$\alpha_2 = \beta_2(r - \beta_3 r_0), \quad (81)$$

and

$$\alpha_3 = 0, \quad (82)$$

where

$$\beta_2 = -4^{-1} g^{1/6} k^{-2} \quad (83)$$

and

$$\beta_3 = S(ZZ_0)^{-1/2}. \quad (84)$$

We note that the leading term of the argument of the exponential function in Eq. 78 is $\alpha_1 \beta_1 |Mx_n|$. As the mode number ($|Mx_n|$) gets larger, this leading term gets larger negative or positive depending, respectively, whether $r > r_0$ or $r < r_0$. If we ignored all other terms in Eqs. 77 and 78, one then might conclude rapid convergence for $r > r_0$ and divergence for $r < r_0$. This is the basis for some of the convergence conclusions by early investigators discussed at the beginning of Sec. III. Morse³ is in error in stating that the series is not convergent for $r < r_0$. His analysis is based on an expression valid for small-order modes similar to Eq. 77. However, as discussed in Sec. III-A, the convergence of the mode series depends on large-order modes for which Eq. 77 is no longer valid. Equation 77 is concerned with the rapidity with which small-order modes converge. We will demonstrate that for our case the second term in the argument of the exponential function of Eq. 78 cannot be ignored but plays a significant role in whether or not the series converges rapidly for $r > r_0$.

The first procedure in our analysis is the determination of the range where $|A_p| = |A_q|$, i.e., where the amplitude of mode p equals the amplitude of mode q . In representations such as Figs. 31 and 32 this is the range where the straight lines representing modes p and q intersect. Using Eq. 77, we may express the solution as

$$r_{pq} = \beta_4(1 + \beta_5)^{-1} + r_0(1 + \beta_3\beta_5)(1 + \beta_5)^{-1}, \quad (85)$$

where

$$\beta_4 = 2\beta_1^{-1}(|Mx_q| - |Mx_p|)^{-1} \times \ln[|h'_2(Mx_q)| |h'_2(Mx_p)|^{-1}] \quad (86)$$

and

$$\beta_5 = (|Mx_q| + |Mx_p|)\beta_2. \quad (87)$$

The most important case is $q=2$ and $p=1$, corresponding to the intersection of mode 2 and mode 1. As discussed at the end of Sec. II, this intersection can be regarded as the beginning of the envelope of the family of curves in representations such as Fig. 32. From Table IV of Ref. 13 the numerical evaluation of Eqs. 86 and 87 yields, for modes 1 and 2,

$$\beta_4 = 0.15508\beta_1^{-1} \quad \text{and} \quad \beta_5 = 6.4261\beta_2. \quad (88)$$

Equation 85 is an excellent approximation. A comparison was made with exact calculations for the intersection of modes 1 and 2. In the case of Figs. 29(b)-(e) and Fig. 32, Eq. 85 gave ranges which were within 0.1 yd of the exact calculations. The maximum difference of 0.77 yd occurred for the case of Fig. 31.

For small-order modes, the first term of Eq. 85 is negative. It is -14.267 yd for the profile parameters of this study. From Eqs. 66 to 68 and Eq. 84 we note that:

$$\beta_3 = 1 \text{ at caustic onset}, \quad (89)$$

$$\beta_3 > 1 \text{ for no caustic}, \quad (90)$$

$$\beta_3 < 1 \text{ for caustic}. \quad (91)$$

Thus the second term of Eq. 85 is equal to r_0 at the caustic onset, is smaller than r_0 for no caustic, and is larger than r_0 when a caustic is formed. Thus the intersection of modes 1 and 2 must occur at a range smaller than r_0 when no caustic is formed. If a caustic is well developed, it is possible for this intersection to occur beyond r_0 but this does not even occur for Fig. 32.

As p and q are increased, the first term of Eq. 85 tends to a smaller negative number while the second term gets smaller for $\beta_3 < 1$ and larger for $\beta_3 > 1$. This interplay between the first and second terms in Eq. 85 determines the basic pattern of Figs. 29, 31, and 32. Although it is possible to analyze these patterns in terms of Eq. 85, the approach is cumbersome. A superior approach is to treat $|Mx_n|$ as a continuous rather than discrete variable and to apply analytical methods of the calculus.

The first step in this approach is to express $|h'_2(Mx_n)|^{-2}$ in terms of $|Mx_n|$. Section VII of Appendix D develops an alternate form to Eq. 77 which is

$$|A_n| = 4^{-1}(2/\pi r)^{1/2} g^{1/2} k^{-1/2} (ZZ_0)^{-1/2} |Mx_n|^{-1/2} E_n. \quad (92)$$

The differentiation of Eq. 92 with respect to $|Mx_n|$ yields

$$d|A_n|/d|Mx_n| = |A_n|X_n, \quad (93)$$

where

$$X_n = -(2|Mx_n|)^{-1} + \beta_1(r-r_0) + 2\beta_1\beta_2(r-\beta_3r_0)|Mx_n|. \quad (94)$$

The expression

$$X_n = 0 \quad (95)$$

yields the extrema of $|A_n|$.

Our first application of Eq. 95 is to determine the mode of maximum or minimum contribution for a given value of r , Z , and Z_0 . Consider the case of Fig. 31 at a range of 700 yd. Equation 95 yields $|Mx_n| = 11.6153$ as the largest positive root. From Eq. 11 of Ref. 1 this corresponds to mode 8.01. The right side of Eq. 54 as evaluated by the computer has a maximum for mode 8 for this situation. Thus agreement is good. As a second example consider the case of Fig. 32 at a range of 3180 yd. Equation 95 yields $|Mx_n| = 38.19$ as the largest positive root. This corresponds to mode 50.33. The right side of Eq. 54 as determined by the computer has a minimum for mode 53 for this situation. Agreement is not so good here because for this large a mode number higher-order terms in Eq. 78, which have been neglected, have an effect.

Let us now solve Eq. 95 for r . The result is

$$r = (2|Mx_n|\beta_1)^{-1}Y_n + r_0(1 + 2\beta_2\beta_3|Mx_n|)Y_n, \quad (96)$$

where

$$Y_n = (1 + 2\beta_2|Mx_n|)^{-1}. \quad (97)$$

Equation 96 is the continuous eigenvalue counterpart of Eq. 85 which applies to the discrete eigenvalues. Equation 85 gives the intersection of two modes, while Eq. 97 gives the envelope which is the intersection between the curves for two parameters as the two parameters approach each other.

The intersection of modes 1 and 2 in Eq. 85 should correspond to the evaluation of Eq. 96 for mode 1.5 or an $|Mx_n|$ of 3.2616. A comparison of Eq. 96 with Eq. 85 for the cases of Figs. 29, 31, and 32 indicates agreement within 0.5 yd.

If we now differentiate Eq. 96 with respect to $|Mx_n|$, we obtain

$$dr/d|Mx_n| = Y_n^2|Mx_n|^{-2}W_n, \quad (98)$$

where

$$W_n = 2\beta_2(\beta_3 - 1)r_0|Mx_n|^2 + (-2\beta_1)^{-1}(4\beta_2|Mx_n| + 1). \quad (99)$$

The sign of Eq. 98 determines the direction in which the envelope moves as the mode number is increased. This equation then explains the basic pattern for low-order modes in Figs. 29, 31, and 32.

In the analysis of the sign of Eq. 98, we first note that Y_n is positive for low-order modes and $Y_n = \infty$ occurs at $|Mx_n| = (-2\beta_2)^{-1}$. For the parameters of this study this $|Mx_n| = 593.64$, corresponding to mode 3069.58. This occurs far beyond the region where Eq. 77 applies. Thus $dr/d|Mx_n|$ has the same sign as W_n in the region

of interest. We further note that the second factor of the second term in Eq. 99 is positive for small-order modes and is zero at $|Mx_n| = (-4\beta_2)^{-1}$. For the parameters of this study this $|Mx_n| = 296.81$, corresponding to mode 1085.37. This again occurs beyond the low-order modes of interest. Thus in the region of interest the second term of Eq. 99 is positive since β_1 is negative. This result corresponds to our statement that the first term of Eq. 85 tends to a smaller negative number as p and q are increased.

The equation,

$$W_n = 0, \quad (100)$$

corresponds to the cusp in the envelope. The analysis of Eqs. 98 and 100 depends primarily on the sign of β_3 in Eq. 99. Consider first the case of $\beta_3 > 1$, which occurs when there is no ray theory caustic. Here the first term in Eq. 99 is positive and Eq. 100 can have a positive real $|Mx_n|$ for a root. For example, the solution of Eq. 100 for the case of Fig. 29b is $|Mx_n| = 6.0035$, which corresponds to mode 3.37. Exact computations on the computer indicate that in this case modes 2 and 3, 3 and 4, and 4 and 5 intersect, respectively, at ranges of 2394.66, 2395.01, and 2394.72 yd. In this case the reversal for the discrete case agrees well with the result of Eq. 100.

The case of no reversal in the range of the intersection of adjacent modes corresponds to the situation where the root of Eq. 100 is too small to correspond to discrete modes. For example, in the case of Fig. 31 the root of Eq. 100 is $|Mx_n| = 1.8503$, corresponding to mode 0.78. There is obviously no discrete counterpart here and there is no range reversal. In the case of Fig. 29(a), the root of Eq. 100 is $|Mx_n| = 3.8772$, corresponding to mode 1.87. At first sight this result would appear to contradict the fact that no range reversal occurs in Fig. 29(a). We will now demonstrate that there is no contradiction. We first note that in the discrete case the transition from no range reversal to a range reversal occurs when

$$\tau_{12} = \tau_{23}, \quad (101)$$

i.e., when the intersection of modes 1 and 2 coincides with that of modes 2 and 3. This would correspond in the continuous case to the cusp occurring at mode 2. Hence if the root of Eq. 100 is less than $|Mx_n| = 4.08795$ there is no range reversal. This is the case in Fig. 29(a).

We may further substantiate this analysis by determining the onset of range reversal for the 682.6-yd source by both the discrete and continuous methods. With the use of Eq. 85, we solve Eq. 101 for receiver depth. The range reversal for the discrete case occurs at a receiver depth of 208 yd. If we set $|Mx_n| = 4.08795$ in Eq. 100 and solve for receiver depth, we obtain the onset of the cusp at 224-yd depth. Thus the results of the two methods agree reasonably well considering the approximations employed. Either method agrees with the result of Figs. 29(a) and 29(b) that the onset of the

range reversal must take place between a receiver depth of 200 and 400 yd. This completes the analysis of $\beta_3 > 1$.

Consider now the case of $\beta_3 \leq 1$, which occurs when there is a ray theory caustic. In this case the first term in Eq. 99 is positive or zero and since the second term in Eq. 99 is positive there can be no solution to Eq. 100. In order to obtain the cusp in this case we would have to include higher-order terms in Eq. 78 and the subsequent development. This has not been done because the next extension of Eq. 99 is a fourth-degree polynomial in $|Mx_n|$ and the analysis becomes too complicated to be very useful. The important aspect of the problem is that the more well developed the ray theory caustic, the larger the first term of Eq. 99 will be. The cusp then can be formed only when higher-order terms cancel this term. This cusp must then correspond to larger $|Mx_n|$ since Eq. 99, which is obviously inadequate under these conditions, is valid for small $|Mx_n|$.

We will now demonstrate that a relative minimum in the contribution of individual modes corresponds to an increase in range of the envelope with increasing mode number. Moreover, a relative maximum corresponds to a decrease in range of the envelope.

From Eq. 93 it follows that

$$d^2|A_n|/d|Mx_n|^2 = |A_n|X_n^2 + |A_n|(dX_n/d|Mx_n|). \quad (102)$$

Upon the evaluation of Eq. 102 at $X_n = 0$, we note that

$$dX_n/d|Mx_n| > 0 \quad (103)$$

corresponds to a relative minimum in the contribution of individual modes, while

$$dX_n/d|Mx_n| < 0 \quad (104)$$

corresponds to a relative maximum.

We consider Eq. 95 to be an implicit relationship between τ and $|Mx_n|$. From fundamental mathematics we may write,

$$d\tau/d|Mx_n| = -(\partial X_n/\partial|Mx_n|)/(\partial X_n/\partial\tau). \quad (105)$$

We now assert that

$$\partial X_n/\partial\tau < 0. \quad (106)$$

Equation 106 follows from the fact that the mode amplitude must attenuate with increasing range. From Eqs. 105 and 106 it follows then that $d\tau/d|Mx_n|$ has the same sign as $\partial X_n/\partial|Mx_n|$. We note also that in Eq. 102 we treated τ as a parameter rather than a variable. Thus in this context the total derivative in Eq. 103 is the same as the partial derivative in the numerator of Eq. 105. It follows that when $dX_n/d|Mx_n|$ is positive (corresponding to a relative minimum), $d\tau/d|Mx_n|$ is positive, corresponding to an increase in range of the envelope with increasing mode number. Similarly a relative maximum corresponds to a decrease

in range of the envelope and our demonstration is complete.

We note from Figs. 29, 31, and 32 that this property applies in all cases and not just to the small-order modes. We will now demonstrate this property for the general case. Consider the expression

$$|A_n| = f \exp g, \quad (107)$$

where f and g are functions of $|Mx_n|$. Equation 107 is the general form that applies for any $|Mx_n|$ but takes different specific forms depending on the size of $|Mx_n|$; for example, Eq. 56 in the case of very large $|Mx_n|$ and Eq. 92 in the case of very small $|Mx_n|$. From Eq. 107 we determine that Eq. 93 holds where X_n is expressed in general terms by

$$X_n = (df/d|Mx_n|)/f + dg/d|Mx_n|. \quad (108)$$

It should be noted that Eqs. 102–106 do not depend upon the particular form in Eq. 94 but apply as well to the general case of Eq. 108. Thus the correspondence between a relative minimum in the contribution of individual modes and an increase in range of the envelope with increasing mode number (also the counterpart for relative maximum and decrease in range) is demonstrated for the general case. Indeed we believe that this property is even more general since Eq. 107 no doubt applies to many other models of the velocity profile.

IV. AREAS FOR FURTHER INVESTIGATION

This study suggests several areas for further investigation. The most obvious is an examination of the convergence properties of both families of modes for the two-layer surface channel of Ref. 1.

References 1 and 10 established good agreement between normal-mode and simple ray theory in the image interference region. The goal of the present article was to compare mode and ray theory for a model in which extensions to simple ray theory must be considered. Because of convergence problems in the mode theory and other complications this goal was only partially achieved. Nonetheless the comparisons, which were possible, are encouraging and indicate that further comparison should be made for other models and configurations.

Other negative-gradient models, which produce a caustic at short range, should be investigated. The model of this article is unrealistic except close to the ocean surface. The onset of the caustic will occur closer to the surface for more realistic models, which have a greater curvature. These models should be examined to establish if the presence of a ray theory caustic at short range is always characterized by a very slow convergence of the normal-mode series.

The convergence zone region for other models should be investigated by normal-mode and extended ray theory. There should be no problem here with conver-

gence of the mode series. However, there will be the problem of the superposition of several caustics which contribute in the convergence zone.

The phase jumps of ray theory are not compatible with the smooth and continuous results of mode theory. Special configurations should be examined in order to determine, at least qualitatively, smooth phase transitions of ray theory which are compatible with the mode result.

V. CONCLUSIONS

A comparison between ray and mode theory was made in the image interference region for a near-surface source and receiver. This comparison verified that there is no $-\pi/2$ jump in the ray phase at a ray vertex.

Analysis, based on the ranges of the minima and maxima in the interference pattern of mode theory, indicates a $-\pi/2$ phase shift in the ray which touches the caustic. However, this analysis suggests that this phase shift is a smooth transition and not an abrupt jump.

Excellent agreement was obtained between ray theory, with a $-\pi/2$ jump in the ray phase at a caustic, and modified ray theory based on Airy functions. The region of agreement coincided, as theoretically predicted, with the region where the asymptotic approximation to the Airy function applies.

The fact that the maximum intensity, associated with a ray theory caustic, does not occur at the caustic range can be explained by two features of ray theory: (1) a $-\pi/2$ jump in the ray phase at a caustic, and (2) the component ray which has touched the caustic always has a greater travel time than the component ray which has not.

The mode theory series for the single-layer model converges in the mathematical sense for ranges which are greater than 1.732 times the sum of the source and receiver depths. The solution diverges for smaller ranges.

When the shadow-zone boundary is the ray which grazes the ocean surface, the mode theory series converges rapidly in the shadow zone and somewhat more slowly in the region ensonified by rays. When the shadow-zone boundary is a caustic the mode theory series converges very slowly even in the shadow zone. This convergence is so slow that in many cases the normal-mode method is impractical because of computer roundoff problems and the large number of modes which must be included. In one example a group of 2600 modes, with individual contributions as much as 280 dB above the resultant, almost completely annihilated itself by phase interference and produced a difference of only 0.02 dB in the resultant.

Plots, which indicate the relative values of the contribution of individual modes as a function of range, were developed previously as aids in determining numbers of modes to be summed and computer roundoff problems. These plots have now proved to be a valuable

tool from the theoretical standpoint, particularly when the eigenvalue parameter is regarded as a continuous rather than discrete variable. A well-developed cusp in the envelope of these plots has been shown to be associated with the presence of a caustic in the ray theory. When there is a relative minimum in the contribution of individual modes, the range at the envelope of the plots is increasing with increasing mode number. Conversely, when there is a relative maximum in the contribution of individual modes the range at the envelope is decreasing with increasing mode number.

A shift in the propagation losses of mode theory as compared to those of ray theory was found to result from a difference in the manner of relating the acoustic pressure to the intensity. This shift can be corrected by multiplying the intensities of mode theory by the ratio of the sound velocity at the source depth to that at the receiver depth.

The normal mode results indicate that the acoustic field in the ray theory shadow zone is the superposition of two diffraction fields. At ranges close to the ray theory caustic, the diffraction field associated with the caustic dominates. At ranges far from the caustic, the diffraction field associated with the ocean surface dominates.

For the model of this study, the phase velocities of all the normal modes are less than the surface velocity. Thus the correspondence between rays and modes through their phase velocity (often useful in other cases) breaks down because there are no modes to correspond to rays reflecting from the surface.

ACKNOWLEDGMENTS

Gary Keck programmed the double-precision calculation of the Hankel and modified Hankel functions. Grace Wofford prepared and drafted the illustrations. She volunteered work after retirement in order to complete this article. We greatly appreciate our 18-year association with Mrs. Wofford, who has made an invaluable contribution to our publications.

APPENDIX A: NOTES ON DERIVATION OF MODE SOLUTION

This derivation follows Marsh¹¹ but with some changes in notation. For the model of Fig. 1(a) the depth functions satisfy Stoke's equation,

$$d^2 U_n / d\zeta^2 + \zeta U_n = 0, \quad (\text{A1})$$

where ζ is given by Eq. 4. A general solution to Eq. A1 in terms of modified Hankel functions is

$$U_n = A_n h_1(\zeta) + B_n h_2(\zeta). \quad (\text{A2})$$

For this model the function $h_2(\zeta)$ represents a downgoing wave. Since U_n must represent a downgoing wave, $A_n = 0$. The surface condition, $U_n = 0$ at $Z = 0$, leads to Eq. 5. Freehafer¹¹ refers to $h_2(\zeta)$ and U_n in

Eq. A2 as the unnormalized and normalized height-gain functions, respectively. With the use of Eq. 246 of Freehafer¹¹ we obtain

$$B_n^2 = 2\lambda_n \left[\frac{\partial h_2(\zeta)}{\partial Z} \frac{\partial h_2(\zeta)}{\partial \lambda} \right]_{Z=0, \lambda=\lambda_n}^{-1}. \quad (\text{A3})$$

From Eq. 4

$$\partial h_2(\zeta) / \partial Z = h'_2(\zeta) g^{\frac{1}{2}}. \quad (\text{A4})$$

From Eqs. 4 and 7

$$\partial h_2(\zeta) / \partial \lambda = h'_2(\zeta) (-2\lambda_n) g^{-\frac{1}{2}}. \quad (\text{A5})$$

Evaluation of Eq. A3 then leads to

$$B_n^2 = -g^{\frac{1}{2}} [h'_2(Mx_n)]^{-2}. \quad (\text{A6})$$

This is the coefficient in Eq. 3.

The solution may also be obtained as a degenerate case of the expressions in Ref. 10. One chooses $\gamma_0 = \gamma_1 = \gamma$, so that the two layers become one layer. Under these conditions basic expressions of Ref. 10 become $\rho = 1$, $M/Z_a = -g^{\frac{1}{2}}$, $Ml = -g^{\frac{1}{2}}Z$, and $Ml_0 = -g^{\frac{1}{2}}Z_0$. Equation 6 of Ref. 10 reduces to

$$G = h_2(Mx_n)W = 0, \quad (\text{A7})$$

where W is the Wronskian. Since $W \neq 0$, Eq. 5 is equivalent to Eq. A7. For both case I and case II of Ref. 10, F_n becomes

$$F_n = h_1(Mx_n)h_2(\zeta). \quad (\text{A8})$$

Equation 8 of Ref. 10 reduces to

$$D_n = W^2. \quad (\text{A9})$$

With the use of $W = h_1(Mx_n)h'_2(Mx_n)$ and other given relationships, Eq. 2 of Ref. 10 reduces to Eq. 3. This approach points out an important feature of the solution. Note that the eigenvalues for the single layer are obtained by setting $\rho = 1$ in Eq. 17 of Ref. 1, which applies to the second family of modes for the two-layer case. There are no modes which correspond to the first family of modes.

APPENDIX B. FIELD NEAR A CAUSTIC

This appendix presents details on how Eqs. 27–30 were obtained from Brekhovskikh,⁴ whose derivation need not be repeated. However, there is such a change in notation that some explanation appears desirable. The following equations relate the necessary notation of Ref. 4, given on the left, to that of the present article, given on the right:

$$x_0 = \theta_s, \quad (\text{B1})$$

$$x_p = \theta_h, \quad (\text{B2})$$

$$k_0 = 2\pi f / C_s, \quad (\text{B3})$$

$$r = R, \quad (\text{B4})$$

$$R = \text{slant range}, \quad (\text{B5})$$

$$\xi = 2\pi f / C_m, \quad (\text{B6})$$

$$\eta(Z) = C_s / C_h, \quad (\text{B7})$$

$$\cos \chi = C / C_m, \quad (\text{B8})$$

$$|\dot{\zeta}|^2 / R^2 = (I/F)_c, \quad (\text{B9})$$

and

$$\nu(t) = \pi^{1/2} \text{Ai}(t). \quad (\text{B10})$$

Equations B1–B7 represent definitions. Equation B8 is Snell's law. Equation B9 relates the ζ of Eq. 38.50 of Ref. 4 to the corrected intensity at a caustic as expressed in Eq. 27. Equation B10 stems from a minor difference in defining the Airy integral.

With use of Eq. B6 and the chain rule for differentiation, we find that

$$\partial^2 \tau / \partial \xi^2 = C_m^3 (C_m d^2 R / dC_m^2 + 2dR / dC_m) / (2\pi f)^2. \quad (\text{B11})$$

At the caustic $dR / dC_m = 0$. Hence

$$(\partial^2 \tau / \partial \xi^2)_{\xi_0} = C_m^4 (d^2 R / dC_m^2) / (2\pi f)^2. \quad (\text{B12})$$

With appropriate substitution in Eq. 38.50 of Ref. 4, we obtain Eq. 27 with

$$K = 4\pi^{1/2} \nu^2(0) = 4\pi^{1/2} \text{Ai}^2(0) = 4(\pi/3)^{1/2} [\Gamma(2/3)]^2. \quad (\text{B13})$$

Equations 28–30 follow from Eqs. 38.51 and 38.52 of Ref. 4 with appropriate substitutions. The constant in Eq. 30 is equal to $\pi^{-1/2}$. The rule for choice of signs in Eq. 38.52 of Ref. 4 is eliminated by the fact that L in Eq. 30 takes the sign of $d^2 R / dC_m^2$.

In obtaining Eq. 27, we suppressed the term $[\eta(Z)]^{-1}$ appearing in Eq. 38.50 of Ref. 4 for reasons now discussed. We must first examine f , the focusing factor of Ref. 4. This term is related to our relative intensity by

$$f / R^2 = I / F. \quad (\text{B14})$$

The focusing factor is closely related to transmission anomaly^{B1} defined by

$$A = -10 \log(I/F) - 20 \log(\text{slant range}). \quad (\text{B15})$$

Hence from Eqs. B14 and B5

$$-10 \log f = A. \quad (\text{B16})$$

One can readily demonstrate with appropriate substitutions that Eq. 38.35 of Ref. 4 is completely compatible with Eq. 23, the expression which applies outside of the caustic region. Now the ζ of Eq. 38.50 of Ref. 4 is related to f by

$$|\dot{\zeta}|^2 = f. \quad (\text{B17})$$

If one follows the development from Eqs. 38.33 to 38.35 of Ref. 4 one finds that

$$f = R^2 \eta(Z) |\Psi_N^+|^2 / 4 \quad (\text{B18})$$

or

$$|\dot{\zeta}| = R |\Psi_N^+| [\eta(Z)]^{1/2}. \quad (\text{B19})$$

Substitution of Eq. 38.49 of Ref. 4 into Eq. B19 yields the modulus of Eq. 38.50 of Ref. 4 with the term $[\eta(Z)]^{-1}$ suppressed.

Our discovery of this inconsistency stemmed from two observations. We first noticed that Eq. 38.50 of Ref. 4 was inconsistent with the results of Marsh,¹⁵ i.e., Eq. 33, which we have used since 1956. We next noticed that the use of Eq. 38.50 of Ref. 4 lead to a displacement of 0.3 dB between the results of Fig. 13. This was contrary to the result of Silbiger¹⁷ that the curves in Fig. 13 should agree at the range given by Eq. 36. Adjustment of the result, based on Eq. 38.50 of Ref. 4, by $10 \log[\eta(Z)]$ gave the proper agreement shown in Fig. 13.

Equation 38.50 of Ref. 4 can be obtained by suppressing $\eta(Z)$ in the equation immediately preceding Eq. 38.34 of Ref. 4. A possible reason for this suppression is discussed in Appendix C.

APPENDIX C. MODE THEORY ADJUSTMENT FOR INDEX OF REFRACTION

The primary purpose of this appendix is a derivation and discussion of Eq. 51, which adjusts the mode theory result for proper comparison with ray theory. This adjustment is closely related to the reciprocity relation, a well-known result of ray theory.^{C1} This is expressed as

$$H_{h,s} = H_{s,h} + 20 \log(C_s / C_h). \quad (\text{C1})$$

Here $H_{s,h}$ represents the propagation loss from a source at a first point to a receiver at a second point and $H_{h,s}$ represents the reciprocal situation, i.e., the source at the second point and the receiver at the first. Equation C1 follows from Eq. 23. It also is valid when Eq. 27 applies as can readily be verified.

However, from Eq. 6, we see that the propagation loss of mode theory is unchanged when source and receiver are interchanged. This result in turn stems from a result, generally applicable to mode theory, that the velocity potential is unchanged when source and receiver are interchanged.

There then appears to be a fundamental difference between ray and mode theory results depending on the size of the second term on the right side of Eq. C1. Although we have been aware of this difference for a long time, we have not considered it important in a practical sense because the variation of velocity in the ocean is such that the second term of Eq. C1 only amounts to tenths of a decibel.

On the other hand the source–receiver configuration of Fig. 20 has not been constrained by the realities of the ocean. Here the source and receiver velocities were about 1186 and 1475 yd/sec, respectively. In this case the second term of Eq. C1 is -1.9 dB. We were not at all surprised then when a displacement appeared between ray and mode theory in Fig. 20. We immediately recognized that this displacement was related to

the difference between ray and mode theory in the case of interchanging source and receiver.

We then decided to examine the fundamentals of both theories and determine why there is a discrepancy and which result is correct. This is the topic of the remainder of this appendix.

Equation 23, the relative intensity of ray theory, is based on elementary geometrical concepts.^{B1} This geometrical concept is difficult to compare with mode theory which is based on physical concepts. Fortunately Eq. 23 can also be obtained from the fundamental relationship between intensity, pressure, and particle velocity given by

$$g = pv = p \nabla \phi, \quad (C2)$$

where ϕ is the velocity potential. On p. 482, Brekhovskikh⁴ demonstrates that with certain approximations Eq. C2 leads to

$$|g| \approx I = \rho \omega k_0 \eta(Z) |\phi|^2. \quad (C3)$$

We next demonstrate that I is the absolute value of the intensity for a plane wave. For a harmonic source,

$$|p| = |\rho \omega \phi|. \quad (C4)$$

With the use of Eq. C4, Eq. C3 may be shown to be equivalent to

$$I = |p|^2 / \rho C. \quad (C4a)$$

Equation C4a is an exact expression for the absolute value of the intensity for a plane wave.

Appendix B demonstrates that Eq. 23 can be obtained from Eq. C3 which is in turn equivalent to Eq. C4a. Thus the relative intensity of ray theory is based on Eq. C4a under the condition that the density is a constant. An alternate presentation by Officer,^{C2} but based on simpler considerations, leads to the same conclusion.

The quantity F in I/F is a measure of source strength and is defined as the average time rate of energy flow per unit solid angle. It may be expressed as

$$F = R^2 |I| = R_0^2 |p_0|^2 / \rho C_s. \quad (C4b)$$

The latter expression is obtained by evaluation at unit distance, using Eq. C4a. If we evaluate Eq. C4a at the receiver and divide by Eq. C4b we obtain Eq. 23a.

Consider now the normal-mode approach. Equations 6a and C4 lead to

$$H_e = -10 \log(|\phi|^2 / |\phi_0|^2), \quad (C5)$$

where ϕ_0 is the velocity potential at unit distance from the source. Equation 6 is based on

$$H_e = -10 \log |\phi|^2 \quad (C6)$$

and is numerically equivalent to Eq. C5 or Eq. 6a since one of the conditions imposed on the normal-mode solution is that the velocity potential at unit distance be unity. From a dimensional standpoint Eq. C5 is the

correct expression. However, $|\phi_0|^2$ is usually suppressed as was done in Eq. 6.

In order to compare the ray theory result with the mode result, we determine the propagation loss using Eqs. 23a and 23b or

$$H_r = -10 \log |p^2 / p_0^2| + 10 \log (C_h / C_s). \quad (C7)$$

Equation 51 follows directly from Eq. C7. This also explains the reciprocity relation of Eq. C1. The mode theory result "splits the difference" between the reciprocal ray theory results. The loss for one ray theory configuration is $10 \log C_s / C_n$ different from the mode theory while the other is $-10 \log C_s / C_h$. The difference in loss between the two ray theory configurations then is $20 \log C_s / C_h$ in agreement with Eq. C1.

The use of Eq. C7 rather than Eq. 6a is equivalent to the suppression of $\eta(Z)$ in Eq. C3. This procedure is quite common. This is apparently what Brekhovskikh used to obtain his Eq. 38.50 in Ref. 4 as discussed in Appendix B. As a more recent example Uginčius^{C3} in reconciling results for two ray theory approaches found that the discrepancy arose from the suppression of $\eta(Z)$ in one of the approaches.

Propagation loss as given by Eq. C7 is the propagation loss which is shown in most of the figures of this article. However, Eq. 6a is commonly used, because in experiments, the hydrophone measures pressure. One determines experimental propagation loss by subtracting $20 \log p / p_{ref}$ from the source level at one yard. Thus a theory based on Eq. 6a would be appropriate for comparison with such experimental results.

Before closing we should note that, in going from Eq. C2 to Eq. C3, we are employing an approximation. This approximation is exact for plane waves. For a true comparison between mode theory and ray theory, one should use Eq. C2 to obtain the intensity of mode theory. However, the evaluation of $\nabla \phi$ poses additional complications to an approach which is already difficult from a computational standpoint. Indeed, a preliminary examination of $\nabla \phi$ for the specific forms of Sec. I-B indicates a formidable task just to demonstrate that $\eta(Z)\phi$ is a first approximation to $\nabla \phi$. At present the detailed evaluation of $\nabla \phi$ does not appear justified, particularly when experimental results are based on the even grosser approximation of Eq. 6a.

APPENDIX D. SERIES EXPANSIONS FOR THE CONTRIBUTION OF INDIVIDUAL MODES

This appendix develops the series expansions which are necessary in the analysis of the contribution of individual modes. It is divided into a number of subsections.

I. SERIES EXPANSIONS FOR λ_n

Consider the binomial series expansion of λ_n of Eq. 7. When

$$|Mx_n| < k^2 g^{-1}, \quad (D1)$$

this series leads to

$$\operatorname{Re} \lambda_n \approx k(1 + g^{\frac{1}{2}} k^{-2} |Mx_n|/4) \quad (\text{D2})$$

and

$$\operatorname{Im} \lambda_n \approx -3^{\frac{1}{2}} 2^{-1} g^{\frac{1}{2}} k^{-1} |Mx_n| (1 - g^{\frac{1}{2}} k^{-2} |Mx_n|/4). \quad (\text{D3})$$

Equations D2 and D3 were obtained with the use of Eq. 8 and the fact that λ_n must lie in the fourth quadrant of the complex plane.

Similarly when

$$|Mx_n| > k^2 g^{-\frac{1}{2}}, \quad (\text{D4})$$

the binomial series leads to

$$\operatorname{Re} \lambda_n \approx 3^{\frac{1}{2}} 2^{-1} g^{\frac{1}{2}} |Mx_n|^{\frac{1}{2}} [1 + (k/g^{\frac{1}{2}})^2/2 |Mx_n|] \quad (\text{D5})$$

and

$$\operatorname{Im} \lambda_n \approx -2^{-1} g^{\frac{1}{2}} |Mx_n|^{\frac{1}{2}} [1 - (k/g^{\frac{1}{2}})^2/2 |Mx_n|]. \quad (\text{D6})$$

II. SERIES EXPANSIONS FOR $\zeta^{\frac{1}{2}}$

Consider the binomial series of $\zeta^{\frac{1}{2}}$, where ζ is given by Eq. 4. When

$$|Mx_n| < g^{\frac{1}{2}} Z, \quad (\text{D7})$$

this series leads to

$$\operatorname{Re} \zeta^{\frac{1}{2}} \approx g^{\frac{1}{2}} Z^{\frac{1}{2}} (1 - 3 |Mx_n|/4 g^{\frac{1}{2}} Z) \quad (\text{D8})$$

and

$$\operatorname{Im} \zeta^{\frac{1}{2}} \approx (\frac{3}{2}) 3^{\frac{1}{2}} 2^{-1} g^{\frac{1}{6}} Z^{\frac{1}{2}} |Mx_n| (1 - |Mx_n|/4 g^{\frac{1}{2}} Z). \quad (\text{D9})$$

Similarly when

$$|Mx_n| > g^{\frac{1}{2}} Z, \quad (\text{D10})$$

the binomial series leads to

$$\operatorname{Re} \zeta^{\frac{1}{2}} \approx -|Mx_n|^{\frac{1}{2}} (1 - 3 |Mx_n|^{-1} g^{\frac{1}{2}} Z/4) \quad (\text{D11})$$

and

$$\operatorname{Im} \zeta^{\frac{1}{2}} \approx (\frac{3}{2}) 3^{\frac{1}{2}} 2^{-1} g^{\frac{1}{2}} Z |Mx_n|^{\frac{1}{2}} (1 - g^{\frac{1}{2}} Z |Mx_n|^{-1}/4). \quad (\text{D12})$$

In order to obtain Eqs. D11 and D12 one must use the fact that $(Mx_n)^{\frac{1}{2}}$ lies in the first quadrant of the complex plane. The steps leading to this choice of square root are somewhat complicated. We first note that for large mode numbers $\zeta \rightarrow Mx_n$. Here we need an expansion of $h_2(\zeta)$, where ζ approaches arbitrarily close to the roots of h_2 . This means that we cannot use Eq. 31 of Ref. 13 since the ray of slope angle $2\pi/3$ is specifically excluded. Equation 32 of Ref. 13 must be used to treat the case of large mode numbers. We note also that ζ always lies in the first or second quadrant. In these quadrants (aside from the positive real axis) Eq. 32 of Ref. 13 is always valid. The proper choice for $\zeta^{\frac{1}{2}}$ in Eq. 32 of Ref. 13 lies in the first quadrant. This choice must hold for all $\zeta^{\frac{1}{2}}$. In particular, it must hold for $\zeta = Mx_n$. Thus $(Mx_n)^{\frac{1}{2}}$ must lie in the first quadrant.

III. ASYMPTOTIC EXPANSION OF $H_0^2(\lambda_n r)$

The first term of the asymptotic expansion of $H_0^2(\lambda_n r)$ may be written as^{D1}

$$H_0^2(\lambda_n r) \sim (2/\pi \lambda_n r)^{\frac{1}{2}} \exp(-i \lambda_n r + \pi i/4). \quad (\text{D13})$$

From Eq. D13 it follows that

$$|H_0^2(\lambda_n r)| \sim (2/\pi r)^{\frac{1}{2}} |\lambda_n|^{-\frac{1}{2}} \exp(r \operatorname{Im} \lambda_n). \quad (\text{D14})$$

We note from Eq. 7 that when Eq. D1 applies,

$$|\lambda_n|^{-\frac{1}{2}} \approx k^{-\frac{1}{2}}. \quad (\text{D15})$$

Similarly when Eq. D4 applies,

$$|\lambda_n|^{-\frac{1}{2}} \approx |Mx_n|^{-\frac{1}{2}} g^{-1/6}. \quad (\text{D16})$$

Figure 30 illustrates the accuracy of Eqs. D15 and D16 for the parameters of this article.

IV. ASYMPTOTIC EXPANSION OF $h_2(\zeta)$

For our application, Eq. 32 of Ref. 13 gives the asymptotic expansions of $h_2(\zeta)$. Since the dominant term of both Eq. D9 and D12 is positive, the contribution of the second series of Eq. 32 of Ref. 13 is small compared to the first series and may be ignored. We obtain

$$h_2(\zeta) \sim \alpha(\zeta)^{-\frac{1}{2}} \exp(-2i\zeta^{\frac{1}{2}}/3 + 5\pi i/12), \quad (\text{D17})$$

where α is $2^{\frac{1}{2}} 3^{1/6} \pi^{-\frac{1}{2}}$. It follows that

$$|h_2(\zeta)| \sim \alpha |\zeta|^{-\frac{1}{2}} \exp(2 \operatorname{Im} \zeta^{\frac{1}{2}}/3). \quad (\text{D18})$$

We note from Eq. 4 that when Eq. D7 applies,

$$|\zeta|^{-\frac{1}{2}} \approx g^{-1/12} Z^{-\frac{1}{2}}. \quad (\text{D19})$$

Similarly when Eq. D10 applies

$$|\zeta|^{-\frac{1}{2}} \approx |Mx_n|^{-\frac{1}{2}}. \quad (\text{D20})$$

V. ASYMPTOTIC EXPANSION OF $h'_2(Mx_n)$

In this case we need an asymptotic expansion for h'_2 evaluated at the roots of h_2 . The appropriate expression is

$$h'_2(Mx_n) \sim 2\alpha(Mx_n)^{\frac{1}{2}} \exp[i\pi(n - \frac{1}{3})]. \quad (\text{D21})$$

Although Eq. D21 is relatively simple, we have not found it cited in the literature. We obtained it by simplification of Eq. 101 of Furry.^{D2} Equation D21 is a very good approximation. For the first root Mx_1 , Eq. D21 gives the real and imaginary parts with error of less than 0.51%. This is the worst case, since the accuracy of Eq. D21 improves with increasing n . From Eq. D21 it follows that

$$|h'_2(Mx_n)| = 2\alpha |Mx_n|^{\frac{1}{2}}. \quad (\text{D22})$$

VI. ASYMPTOTIC EXPRESSIONS FOR $|A_n|$

We now combine results to obtain asymptotic expressions for the contributions of various modes. From Eqs. 52, D14, 3, and D18 we obtain

$$|A_n| = (2/\pi r)^{\frac{1}{2}} g^{\frac{1}{2}} [h'_2(Mx_n)]^{-2\alpha^2} |\zeta \zeta_0|^{-\frac{1}{2}} |\lambda_n|^{-\frac{1}{2}} E_n, \quad (\text{D23})$$

where

$$E_n = \exp[2(\operatorname{Im} \zeta^{\frac{1}{2}} + \operatorname{Im} \zeta_0^{\frac{1}{2}})/3 + r \operatorname{Im} \lambda_n]. \quad (\text{D24})$$

A more useful form is obtained by the substitution of Eq. D22 into Eq. D23 to yield

$$|A_n| = 4^{-1}(2/\pi r)^{1/2} |Mx_n|^{-1/2} |\zeta \zeta_0|^{-1/2} |\lambda_n|^{-1/2} E_n. \quad (D25)$$

We are now ready to apply the expansions of Secs. A and B of this appendix. We note that Eqs. D1 and D4 determine two regions as far as λ_n is concerned. Equations D7 and D10 determine two regions for ζ and two more for ζ_0 . Since in the general case all of these regions are independent, this leads to eight expressions for Eq. D24, applying in eight different regions of $|Mx_n|$. Here we shall consider only two regions—the region for very small mode numbers and the region for very large mode numbers.

VII. $|A_n|$ FOR SMALL-ORDER MODES

Consider the region where $|Mx_n| < k^2 g^{-1}$ and $g^{\dagger} Z$ and $g^{\dagger} Z_0$. This region applies to the small-order modes. Equation 77 is obtained from Eqs. D23, D19, and D15 and the value of α (in text after Eq. D17). Equation 92 is obtained in similar fashion starting with Eq. D25 rather than Eq. D23.

From Eqs. D24, D9, and D3 we obtain

$$E_n = \exp(-|Mx_n| 3^{1/2} 4^{-1} g^{\dagger} k^{-1} F_n), \quad (D26)$$

where

$$E_n = r - 2kg^{-1}(Z^{\dagger} + Z_0^{\dagger}) - |Mx_n| 4^{-1} g^{\dagger} k^{-2} [r - 2g^{-1} k^3 (Z^{-1} + Z_0^{-1})]. \quad (D27)$$

Some of the mode theory expressions in Eq. D27 may be related to ray theory. From Eq. 11 we may write the range of the shadow zone, r_0 , when it is determined by the ray which grazes the surface rather than a caustic as

$$r_0 = 2b^{-1} C_0^{-2} [(C_0^2 - C_h^2)^{1/2} / C_h + (C_0^2 - C_s^2)^{1/2} / C_s]. \quad (D28)$$

If we express C_h and C_s in terms of depths and profile parameters we find that Eq. D28 becomes

$$r_0 = (-2C_0/\gamma)^{1/2} (Z_h^{\dagger} + Z_s^{\dagger}). \quad (D29)$$

In our mode theory notation, $Z_h = Z$ and $Z_s = Z_0$ and with the use of Eq. 2, D29 becomes

$$r_0 = 2kg^{-1}(Z^{\dagger} + Z_0^{\dagger}). \quad (D30)$$

Equation D30 may be expressed in terms of a fundamental depths S as

$$r_0 = 2S^{\dagger}(Z^{\dagger} + Z_0^{\dagger}), \quad (D31)$$

where

$$S = k^2 g^{-1}. \quad (D32)$$

With the use of Eqs. D30–D32, Eq. D27 may be written as

$$F_n = r - r_0 - |Mx_n| 4^{-1} g^{\dagger} k^{-2} [r - S(ZZ_0)^{-1/2} r_0]. \quad (D33)$$

Equations 78 and 78 follow from Eq. D26. Equations 80, 81, 83, and 84 follow from Eq. D33. Equation 82 results

from the fact that $\text{Im}(Mx_n)^2 = 0$ and drops out of the expansion of λ_n and ζ^{\dagger} .

VIII. $|A_n|$ FOR LARGE-ORDER MODES

Consider the region where $|Mx_n| > k^2 g^{-1}$ and $g^{\dagger} Z$ and $g^{\dagger} Z_0$. This region applies to the large-order modes. Equations 56–59 are obtained from Eqs. D25, D20, D16, D24, D12, and D6.

IX. TEST FOR CONVERGENCE OF MODE SERIES

This section examines the convergence of the normal-mode series when $\alpha_1 < 0$ where α_1 is given by Eq. 58. We first note from Eq. 56 that for sufficiently large n , i.e., $|Mx_n|$, $|A_n| < E_n$. Thus if we demonstrate the convergence of $\sum E_n$ it follows that the mode series is absolutely convergent and hence is conditionally convergent.

Now for sufficiently large n , $|Mx_n|$ may be approximated¹ by

$$|Mx_n| \sim [(3\pi/2)(n - \frac{1}{4})]^{\dagger}. \quad (D34)$$

Thus from Eqs. 57 and 58 for large n and $\alpha_1 < 0$

$$E_n \approx \exp[K(n - \frac{1}{4})^{\dagger}], \quad (D35)$$

where

$$K = (3\pi/2)^{\dagger} 2^{-1} g^{\dagger} \alpha_1. \quad (D36)$$

Unfortunately the standard tests for convergence such as D'Alembert's ratio test and Cauchy's n th root test fail when applied to a series of terms of the form of Eq. D35. However, since K is negative,

$$f(x) = \exp[K(x - \frac{1}{4})^{\dagger}] \quad (D37)$$

is a positive, continuous, decreasing monotonic function for $1 \leq x < \infty$. Hence we may apply Maclaurin's integral test. Under the transformation $\mu^3 = x - \frac{1}{4}$ this integral becomes

$$\lim_{b \rightarrow \infty} \int_a^b 3\mu^2 \exp(K\mu) d\mu, \quad (D38)$$

where $a = (\frac{3}{4})^{\dagger}$. Integral D38 is a type form which may be evaluated for $K < 0$ as equal to

$$-3(a^2 K^{-1} - 2a K^{-2} + 2K^{-3}) \exp(Ka). \quad (D39)$$

Since this expression is finite, Maclaurin's integral test proves that $\sum E_n$ converges for $\alpha_1 < 0$. Hence the series is absolutely convergent for $\alpha_1 < 0$. (Note that Eq. D35 does not apply for mode 1 corresponding to the lower limit of the integral test. This does not affect the proof since Eq. D39 is finite for some finite a that corresponds to the lowest-order mode for which Eq. D35 represents the dominant behavior.)

In the case of $\alpha_1 = 0$ Eq. 56 may be approximated for large n by

$$|A_n| \approx L n^{-\frac{3}{2}}, \quad (D40)$$

where L is a nonzero bounded constant. Now the

harmonic series, Σn^{-1} , diverges. Since $n^{-\frac{2}{3}} > n^{-1}$ for large n , it follows that the normal-mode series does not converge absolutely for $\alpha_1=0$. It is possible that the normal-mode series converges conditionally. However, we will not continue the complicated analysis of this case since it is not important.

¹ M. A. Pedersen and D. F. Gordon, J. Acoust. Soc. Amer. 47, 304-326 (1970).

² C. L. Pekeris, J. Acoust. Soc. Amer. 18, 295-315 (1946).

³ S. Flügge, *Encyclopedia of Physics* (Springer, Berlin, 1961), Vol. X1/1, pp. 81-85.

⁴ L. M. Brekhovskikh, *Waves in Layered Media* (Academic, New York, 1960), pp. 474-492.

⁵ I. Tolstoy, J. Acoust. Soc. Amer. 44, 675-683 (1968).

⁶ A. Silbiger, J. Acoust. Soc. Amer. 44, 653-654 (1968).

⁷ W. D. Hayes, J. Acoust. Soc. Amer. 44, 828 (1968).

⁸ D. H. Wood, J. Acoust. Soc. Amer. 44, 1154-1155 (1968).

⁹ J. E. Freehafer, "The Effect of Atmospheric Refraction on Short Radio Waves," Mass. Inst. Technol. Lab. Rep. 447 (1943).

¹⁰ M. A. Pedersen and D. F. Gordon, J. Acoust. Soc. Amer. 37, 105-118 (1965).

¹¹ H. W. Marsh, "Theory of the Anomalous Propagation of Acoustic Waves in the Ocean," U. S. N. Underwater Sound Lab. Rep. 111 (1950), pp. 34-36.

¹² W. H. Furry, "Methods of Calculating Characteristic Values for Bilinear M Curves," Mass. Inst. of Technol. Lab. Rep. 795 (1946).

¹³ *Tables of the Modified Hankel Functions of Order One-Third and of Their Derivatives* (Harvard U. P., Cambridge, Mass., 1945).

¹⁴ J. C. P. Miller, *The Airy Integral* (Cambridge U. P., Cambridge, England, 1946). British Assoc. for the Advancement of Science, Math. Tables Pt., Vol. B.

¹⁵ H. W. Marsh and M. Schulkin, "Underwater Sound Transmission," Avco Marine Electron. Rep. (1962), p. 46.

¹⁶ W. S. Kimball, *Calculus of Variations* (Butterworths, London, 1952), pp. 291-324.

¹⁷ A. Silbiger, "Focusing of Sound and Explosive Pulses in the Ocean," Cambridge Acoustical Assoc. Tech. Rep. U-286-188 (1968).

¹⁸ H. P. Bucker, J. Acoust. Soc. Amer. 36, 251-258 (1964).

¹⁹ D. E. Kerr, *Propagation of Short Radio Waves* (McGraw-Hill, New York, 1951), pp. 78-79.

²⁰ Summary Tech. Rep. of DIV 6, NRDC, Vol. 8, pp. 51-53 (1946).

²¹ J. W. Horton, *Fundamentals of SONAR* (US Naval Institute, Annapolis, Maryland 1957), p. 120.

²² C. B. Officer, *Introduction to the Theory of Sound Transmission* (McGraw-Hill, New York, 1958), pp. 43-44.

²³ P. Uginčius, J. Acoust. Soc. Amer. 47, 339-341 (1970).

²⁴ G. N. Watson, *A Treatise on the Theory of Bessel Functions* (Cambridge U. P., Cambridge, England, 1944), p. 198.

²⁵ W. H. Furry, "Methods of Calculating Characteristic Values for Bilinear M Curves," Mass. Inst. Technol. Lab. Rep. 795 (1946).